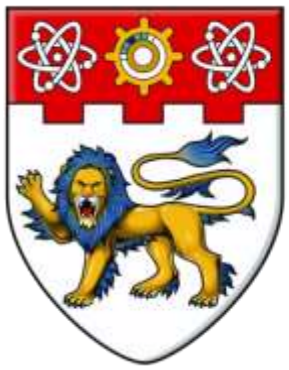

NANYANG TECHNOLOGICAL UNIVERSITY

Synthesis, Properties and Applications of 2D Materials

ZHOU JIADONG

SCHOOL OF MATERIALS SCIENCE AND ENGINEERING

[12/06/2017]

Synthesis, Properties and Applications of 2D Materials

ZHOU JIADONG

SCHOOL OF MATERIALS SCIENCE AND ENGINEERING

A thesis submitted to the Nanyang Technological University
in partial fulfilment of the requirement for the degree of
Doctor of Philosophy

2017

Statement of Originality

I hereby certify that the work embodied in this thesis is the result of original research and has not been submitted for a higher degree to any other University or Institution.

. . 12/06/2017. . . . .

ZHOU JIADONG

Abstract

Two dimensional materials (TMDs) have drawn more attention due to their excellent physical properties such as high mobility, valley spintronic and high on/off ratio. The band gap changing from indirect in bulk to direct in monolayer makes them as potential candidates for the next generation applications for field effect transistor (FET), flexible transparent electrodes, photonics sensors, conductive composites, gas separation membranes and nonlinear optics.

So far, following the reported monolayer graphene, more than 40 different TMDs have been reported. However, many work only focus on synthesis and properties of TMDs in Mo-/W-based (MX_2, M: Mo, W; X: S, Se) and MX_2 based heterostructures. Other 2D TMDs are rare to be studied due to their difficulties synthesizing by chemical vapor method (CVD), such as $MoTe_2$, WTe_2, IV-, V-, Re-, and VIII-based TMDs, impeding researchers to study their properties such as superconductivity, spintronic, magnetism and applications.

Furthermore, the heterojunctions based on the different structure of monolayer TMDs offer the possibility to fabricate the p-n junction, high-speed electronics, optoelectronic, LEDs and spin valleytronic devices. The most of studies focus on the heterojunctions with combination of WX_2 and MoX_2. The heterojunctions with different crystal structures are difficult to be realized, such as the heterostructures between MX_2 and PtX_2 (X: S, Se). In addition, compared with the TMDs, the IIIA-VIA layered materials such as GaS, GaSe, In_2Se_3 and InSe also show potential applications for next generation electronics and optoelectronics due to their suitable bandgaps. The properties such as the optical and optoelectronic have not been studied. Based on the above analysis of problems, in this thesis:

First, the monolayer $MoTe_2$ and WTe_2 were synthesized by CVD method. The size of monolayer $MoTe_2$ and WTe_2 is up to 300 μm and 100 μm, respectively. Scanning transimission electron microscopy (STEM) was used to confirm their atomic structures. Devices fabricated using monolayer $MoTe_2$ and few layer WTe_2 show enhanced

superconductivity in few layer $MoTe_2$ and semimetal-insulator transfer between few layer in WTe_2.

Second, using the molten salt-assisted CVD method, varied types of TMDs were synthesized, including Ti (TiS_2, $TiSe_2$, and $TiTe_2$), V (VS_2, VSe_2, and VTe_2), Nb (NbS_2, $NbSe_2$, and $NbTe_2$). Raman and photoluminescence (PL) spectroscopy were used to confirm as-synthesized TMDs. Atomic force microscopy (AFM) was used to check the thickness of as-synthesized crystals. STEM was used to confirm their atomic structure.

Third, the heterojunction with different crystal structure and lattice constant between $PtSe_2$ and $MoSe_2$ was synthesized via one-step CVD method. The Raman and PL mapping reveal the vertically stacking between $PtSe_2$ and $MoSe_2$. X-ray photoelectron spectroscopy (XPS) and annular dark-field scanning transition electron microscopy (ADF-STEM) demonstrate the strong coupling epitaxial growth behavior of $PtSe_2$ on the $MoSe_2$. The device using $PtSe_2$/$MoSe_2$ heterostructure shows a typical p-n junction property.

Forth, the monolayer In_2Se_3 for the first time was prepared by physical vapor deposition (PVD) method. Raman and PL spectra were identified in the monolayer In_2Se_3. STEM confirmed the hexagonal structure of In_2Se_3. The FETs fabricated using few layer In_2Se_3 perform excellent optoelectronic properties, indicating In_2Se_3 atomic layers as a promising candidate for the optoelectronic and photosensitive device applications.

Acknowledgements

I would like to take this opportunity to sincerely appreciate the professional instruction, selfless guidance and invaluable enlightenment of Prof. Liu Zheng on the research project. His insightful advice and discussions are an invaluable treasure for me. Especially, his guidance on how to write a good paper and draw a beautiful figure. His enthusiasm towards scientific research and life will undoubtedly benefit me.

Herein, I express my gratitude to Prof. Jin Chuanhong and Mr. Lv Danhui from Zhejiang University, Prof. Zhou Wu from University of Chinese Academy of Sciences, Dr. Lin Junhao and Prof. Kazu Suenaga from National Institute of Advanced Industrial Science and Technology, Mr Zhang Bowei and Prof. Huang Yizhong from NTU to help me testing the TEM. In addition, I express my gratitude to Prof. Li shuzhou for his advice on my project.

I express my gratitude to Xia Juan, Sun Linfeng, Chen Yu, Dr. Jiang chongyun, Dr. Cong chunxiao, Dr Wang hailong, Prof Yu ting, Prof. Gao weibo and Prof Shen zexiang from SPMS in the support of test Raman test. In addition, I would extend my gratitude to technical staff, especially those in FACTS, for their patient training and cooperation all the way.

Many thanks and appreciations go to Mr Huang Xiangwei and Prof. Liu guangtong from Beijing National Laboratory for Condensed Matter Physics, Institute of Physics, Chinese Academy of Sciences for their support in devices fabrication and measurements.

Many thanks and appreciations go to Prof. Hsin Lin from National University of Singapore, Dr. Xie Yu, Prof. Boris I. Yakobson from Rice University, Prof. Ji Wei from Renmin University of China for their support in theoretical calculations.

Also, I want to express my gratefulness to all group members: Dr. Liu Fucai, Dr. Zeng Qingsheng, Dr. Niu Lin, Dr. Yu Peng, Dr. Wang Xiaowei, Dr. Zheng Lu, Dr. He Yongmin, Dr. Zhu Chao, Dr. Wang Hong, Mr Fu Qundong, Mr Wang Xuewen, Mr Zhu Chao, Mr Yan Cheng for their enthusiastic sharing of their experience and skills. I also want to say many thanks to my friends.

I am very grateful to my father Mr Zhou Guolun, mother-in-law Mrs Li Qingfang, father-in-law Mr Li Zhenying and especially my wife Dr. Zhou Yao from Shanghai Institute of Ceramics, Chinese Academy of Sciences in China. Because of her unconditional support and encouragement, I can finish my thesis.

Finally, I dedicate this thesis to my mother.

This thesis is supported by the Singapore National Research Foundation under NRF RF Award No. NRF-RF2013-08, the start-up funding from Nanyang Technological University (M4081137.070).

Table of Contents

Table Captions

Figure Captions

Figure 2.10 A topological phase transition in 2D TMDs.

Figure 2.11 STM images (*Z*-channel) showing the formation of TiS_2 nanocrystals after deposition of Ti on AuS/Au (111). (a) As-prepared AuS film on Au (111) with a characteristic vacancy island pattern. (b) After deposition of 0.25 ML Ti at room temperature; consecutive heating to (c) 450 K, (d) 550 K, (e) 670 K, and (f), 800 K for 10 minutes leads to the formation of TiS_2 nanocrystals.

Figure 2.12 TEM and HRTEM images of the as-synthesized TiS_2 nanotubes: (a and b) Low-magnification TEM images and (c, d, e) HRTEM images.

Figure 2.13 The pressure–temperature phase diagram of $TiSe_2$. (a) Charge density wave (CDW) ordered and the phase boundaries between normal state and superconducting. (b) Zoom-in on the region where exhibits the transition between commensurate and incommensurate order.

Figure 2.14 (a) Schematic for 2D $TiSe_2$ growth using CVT method. (b) and (c) Optical and AFM images of the as-obtained $TiSe_2$ flakes.

Figure 2.15 (a) The magnetic moment per X atom in MX. (b) The energy difference between FM and AFM order (c) of VX_2 monolayers.

Figure 2.16 (a) Temperature dependence of resistance in the temperature range 80–200 K. (b) ZFC magnetization of the obtained ultrathin VSe_2 nanosheets. (c) M–H curves of VSe_2 nanosheets at 300 K. (d) TDOS and PDOS of VSe_2 monolayer.

Figure 2.17 (a) Scanning electron microscope (SEM) images of VS_2 nanosheets. (b) SEM image of VS_2 with aligned parallel to the substrate. (c) Dominant hexagon. (d) Nearly "half-hexagon" shape of VS_2. (e–h) Optical images of VS_2 crystals.

Figure 4.3 (a) AFM image of $MoTe_2$ monolayer. Inset showing a thickness of 0.9 nm for $MoTe_2$, demonstrating that the as-grown $MoTe_2$ is monolayer. (b and c) The corresponding amplitude and phase image, respectively..

Figure 4.4 (a–f) WTe_2 single crystal triangles with thicknesses from 25 nm to monolayer layer. 10 nm and thicker WTe_2 flakes can be obtained when the reaction time is more than 10 min. Scale bar: 10 μm. (g) A large-size WTe_2 monolayer with size up to 120 μm. Scale bar: 20 μm. A few regions are bi-layer and tri-layer WTe_2 (dark purple) as labeled. Such few-layer regions also facilitate forming a ribbon-like structure, complying with the 1T′ structure of WTe_2. (h) The thickness of the WTe_2 flake as a function of the growth time.

Figure 4.5 (a, d, g, j) Optical images of WTe_2 flakes captured by AFM measurement. Scale bar: 10 μm. The corresponding AFM images are shown in b, e, h and k, respectively. Scale bar: 2 μm. The corresponding thickness that are shown in c, f, i, and l is about 17 nm, 14 nm, 2 nm and 1 nm, respectively. Because the thickness of monolayer WTe_2 is about 0.8 nm. The WTe_2 flakes in g and j correspond to bilayer and monolayer ones, respectively.

Figure 4.6 Raman spectra and mapping of WTe_2 and $MoTe_2$ monolayers. (a) Raman spectra of WTe_2 with different thickness. (b) Optical image of a monolayer WTe_2. (c) Raman intensity mapping using A_1^9 from the region in b. (d) Raman spectra of $MoTe_2$ with different thickness. (e) Optical image of monolayer and bilayer $MoTe_2$. (f) Raman intensity mapping of A_g at 161 cm^{-1}.

Figure 4.7 Raman mapping of monolayer and bilayer WTe_2. (a) Optical image of large monolayer WTe_2. The corresponding Raman intensity and Raman center mapping is shown in c and e, respectively. (b) Optical image of bilayer WTe_2. (d and f) Shows the corresponding Raman intensity and center mapping of bilayer WTe_2 with grain boundary, respectively.

Figure 4.8 STEM characterization of WTe_2 atomic layer. (a) STEM Z-contrast image of a monolayer WTe_2. The coordinate and structural model are overlaid on the image. Insets:

FFT pattern and simulated STEM image of the monolayer WTe_2. (b) Line intensity profile file of the region highlighted by red rectangle in a. (c, d) STEM Z-contrast image of a bilayer WTe_2 with 2H stacking c and 2H' stacking (d). The green and red dash diamonds indicate the orientation of the zigzag W-Te chains in the first and second layer, respectively. 2H and 2H′ stacking is differed by half of a unit cell shifting along the *b* aixs in the second layer. Images in green are simulated images. (e) STEM Z-contrast image of an atomically sharp stacking boundary between the 2H (left) and 2H′ (right) stacking. The structural model is optimized by DFT calculations. (f) Projected DOS of the W atoms in the mirror twin boundary and in the bulk, showing more states near the Fermi level for W atoms in the boundary region. Inset: the structural model of the mirror twin boundary.

Figure 4.9 TEM characterize of WTe_2 flakes. (a) Low magnification TEM imaging of WTe_2 thick flake. The triangle WTe_2 flake can be seen in Figure 4.9a and b, the selected area electron diffraction (SAED) in a, which shows reciprocal lattice of the WTe_2 single crystal. (c) High resolution image of WTe_2 in a, b, and c show the high quality of the thick WTe_2 flakes.

Figure 4.10 Atomic structure of $MoTe_2$ and WTe_2 few layers. (a, b) Experimental STEM image, FFT pattern, simulated STEM images with corresponding atomic model and EELS spectra of $MoTe_2$ (a) and WTe_2 (b) few layer. $MoTe_2$ and WTe_2 are very similar in structures. The simulations were done on a 6-layer model with a small tilting away from the [001] direction.

Figure 4.11 Transport in different thicknesses of WTe_2 flakes and superconductivity in few layered $MoTe_2$. (a) The resistance of 4 nm and 2 nm WTe_2 flakes at different temperature under zero magnetic field, respectively. (b) Field-dependent magnetoresistance of 2 nm WTe_2 flake under different temperatures. (c) Superconducting transition behavior of a few layered $MoTe_2$ under zero magnetic field. (Inset: Superconductivity at different perpendicular magnetic fields). (d) The upper critical field H_{c2} under dependence temperature. The solid red line is the linear fit to H_{c2}.

.

Abbreviations

TMD	Transition Metal Dichalcogenide
MX_2	M: M, W; X: S, Se
CVD	Chemical Vapor Deposition
PVD	Physical Vapor Deposition
FET	Field-effect Transistor
BN	Boron Nitride
BP	Black Phosphorous
MoX_2	X: S, Se
WX_2	X: S, Se
AFM	Atomic Force Microscopy
TEM	Transmission Electron Microscopy
STEM	Scanning Transmission Electron Microscopy
XPS	X-ray Photoelectron Spectroscopy
PL	Photoluminescence
1T	One Layer per Repeat, Tetragonal Symmetry
2H	Two Layers per Repeat, Hexagonal Symmetry
3R	Three Layers per Repeat, Rhombohedral Symmetry
CVT	Chemical Vapor Transfer
CDW	Charge Density Wave
LPCVD	Low Pressure Chemical Vapor Deposition
TiX_2	X: S, Se, Te
VX_2	X: S, Se, Te
NbX_2	X: S, Se, Te
DFT	Density Functional Theory
SEM	Scanning Electron Microscope
PMMA	Poly (methyl methacrylate)
PC	Poly (bisphenol A carbonate)
PDMS	Polydimethylsiloxane
EELS	Electron Energy Loss Spectroscopy

IPA	Iso-Propyl alcohol
ADF	Annular dark-field
PPMS	Physical Property Measurement System

Chapter 1

Introduction

In this chapter, a brief introduction on this thesis will be elaborated. First, the hypotheses about synthesis, properties and applications of the large-size tellurides including $MoTe_2$ and WTe_2, new two-dimensional transition metal dichalcogenides in group IV and group V, new vertically stacked heterostructure and In_2Se_3 monolayer will be introduced. Second, based on the hypotheses, the objectives and scopes including synthesis, properties and applications of large monolayer $MoTe_2$, WTe_2, TiX_2, VX_2, NbX_2, $PtSe_2$/$MoSe_2$ and monolayer In_2Se_3 are then described. Third, the dissertation overview for each chapter in the whole thesis is also presented. Finally, the findings and outcomes of this thesis are summarized based on the whole content.

1.1 Hypothesis/Problem Statement

The discovery of monolayer graphene has opened up the field of two-dimensional materials.[1] The monolayer graphene has lots of excellent properties, such as high thermal conductivity,[2] high electron mobility,[3] large specific surface area[4] and high strength. [5] These unique properties have inspired a great amount of research on its applications, including ultrafast photoresponse, photodetectors,[6] broadband light emitters, flexible electronic devices,[7] super capacitors and lithium ion batteries.[8,9] However, the zero bandgap in the intrinsic monolayer graphene limits its applications in the semiconducting devices such as field-effect transistor (FET) and logic circuits.[10] Hence people move their focus on the graphene-like two dimensional materials, such as transition metal dichalcogenides (TMDs), boron nitride (BN), black phosphorus (BP) and IV-VI layered materials(for example InSe and In_2Se_3), among which the TMDs are the hottest.[11-19]

Similar to the graphite, adjacent layers are coupled by the van der Waals interaction in bulk TMDs, which make them easy to get monolayer and few-layer TMD crystals by different methods including mechanical exfoliation using the Scotch tape, PVD and CVD method. Synthesis of large scale atom-thin TMDs is the key for their further applications and exploiting their novel properties. So far, more than 40 different TMDs have been reported. However, most of the efforts focus on the MX_2 (M: M, W; X: S, Se). Lacking of a suitable method to preparing the remaining 2D TMDs impedes researchers to study the novel properties such as the high mobility in group IV-based TMDs, charge density wave state, superconductivity in group V-based TMDs, superconducting transfer behavior in $MoTe_2$ and topological insulate state in WTe_2.[20-25] Therefore, it is very urgent to make large-size single-crystal TMDs.

Owning to the development of TMDs, the heterostructures based on different TMDs show excellent properties and great potential applications in speed electronics, optoelectronic devices, transistors, sensors, photodetectors, LEDs and spin valleytronic devices. Traditional 2D TMDs heterostructures are often obtained via combining the TMDs with different chemical composition and properties by sequential mechanical method. However, a small overlap sample size and the interface contamination is difficult to avoid. If the

TMDs heterostructure can be synthesized via one-step method, the interface contamination can be avoided. So far, only the MoX_2/MX_2 heterostructures (MX_2, where M are the transition metals such as Mo or W, and X is S, or Se) via one-step or two steps by van der waals epitaxial method have been reported.[26-34] Synthesis of the heterostrurcture, such as between MX_2 and group-10 TMDs (for example PtS_2 and $PtSe_2$), cannot be realized due to the two reasons: 1) the low chemical reactivity of Pt and Pd; 2) The crystal structures of PtS_2 and $PtSe_2$ are different from the MX_2.

Compared with the TMDs, the layered materials combined by group IIIA and group VIA (such as In_2Se_3) have also the similar structure to 2D TMDs and have been considered as the potential candidates for the next generation of optoelectronic devices. However, synthesis of the In_2Se_3 monolayer is very difficult due to many phases existence, which prohibits researchers to study their optoelectronic properties. If the large monolayer In_2Se_3 can be synthesized, their properties and applications in different fields can be studied.

1.2 Objectives and Scope

Based on the discussion in the hypothesis part, the objectives are shown as follows:

First, large $MoTe_2$ and WTe_2 monolayer will be synthesized by CVD method. The thickness of $MoTe_2$ and WTe_2 will be measured by atomic force microscopy (AFM). The quality of $MoTe_2$ and WTe_2 will be checked by Raman spectroscopy. The atomic structure of $MoTe_2$ and WTe_2 will be examined by transmission electron microscopy (TEM) and scanning transmission electron microscopy (STEM). Different layers of $MoTe_2$ and WTe_2 will be used to fabricate devices to exploit their properties.

Second, the growth mechanism of MoS_2 will be studied. Subsequently, a new method of molten salt-assisted CVD will be designed. Meanwhile, the growth mechanism of this method will be discussed. Monolayer and few layer 2D TMDs including TiS_2, $TiSe_2$, $TiTe_2$, VS_2, VSe_2, VTe_2, NbS_2, $NbSe_2$ and $NbTe_2$ will be prepared. The Raman, PL, AFM, TEM and STEM will be used to check their quality, thickness and atomic structure.

Third, a new heterostructure between monolayer $PtSe_2$ and monolayer $MoSe_2$ will be synthesized by CVD method via one-step process. Raman and PL spectroscopy will be used to confirm the vertically stacked structure. Moreover, X-ray photoelectron spectroscopy (XPS) will be used to check the distribution of elements and the charge transfer between $MoSe_2$ and $PtSe_2$. The STEM will be further used to study the atomic structure of the vertically stacked heterostructure. Devices using the $PtSe_2/MoSe_2$ will be fabricated and their p-n junction property will be studied.

Forth, monolayer In_2Se_3 will be synthesized by PVD method. Thickness of In_2Se_3 under different growing conditions will be studied. Spectroscopic method such as Raman and PL will be used to check its quality and its phase. STEM will be used to confirm its crystal structure. At last, the applications of In_2Se_3 devices for FET and photodetectors will be exploited.

1.3 Dissertation Overview

The thesis addresses the synthesis of large monolayer $MoTe_2$ and WTe_2, which offers the opportunities to fabricate the devices to study their superconducting transition behavior and semimetal-insulator transition. And this thesis addresses how to synthesize the new 2D TMDs such as IV-, V-based 2D TMDs, and shows how to characterize the as-synthesized 2D TMDs using different techniques. Meanwhile, this thesis addresses how to produce the new heterostructure between $MoSe_2$ and $PtSe_2$ and the monolayer In_2Se_3, and finally demonstrates their potential applications for FET and photodetectors.

Chapter 1 provides a rationale for the research and outlines the goals and scope.

Chapter 2 reviews the literature about the background of 2D materials and the current research progress of 2D TMDs, heterostructures and In_2Se_3. Especially, the structure, properties, potential applications and synthetic method of 2D materials will be introduced. The problems and possible methods will be shown in this chapter.

Chapter 3 discusses the principles of the methods that are used to synthesize $MoTe_2$, WTe_2, other 2D TMDs, heterostructure and In_2Se_3. The principles of the characterization methods such as Raman spectroscopy, AFM, TEM and STEM and applications of these 2D materials are discussed.

Chapter 4 elaborates the synthesis and characterizations of monolayer $MoTe_2$ and WTe_2. The superconducting transition behavior in few layer $MoTe_2$ and semimetal-insulator transition in few layer WTe_2 are elaborated.

Chapter 5 elaborates the preparation and characterizations of 2D TMDs, including monolayer TiS_2, few layer $TiSe_2$, few layer $TiTe_2$, monolayer VS_2, few layer VSe_2, few layer VTe_2, monolayer NbS_2, monolayer $NbSe_2$ and few layer $NbTe_2$. Raman spectroscopy and STEM are used to confirm the as-synthesized crystals.

Chapter 6 elaborates the preparation and characterizations of the heterostructure between monolayer $PtSe_2$ and monolayer $MoSe_2$. Demonstrating the epitaxial behavior is the key role for the growth of the heterostructure. The p-n junction property based on the heterojunction is discussed.

Chapter 7 elaborates the synthesis and characterizations of the monolayer In_2Se_3. Raman spectroscopy and STEM are performed to demonstrate the α phase of as-produced monolayer In_2Se_3. Potential applications such as FET and photodetector are studied.

Chapter 8 shows the conclusions and implications of this thesis. Elaborating the reconnaissance should be done in the future.

1.4 Findings and Outcomes/Originality

This research led to several novel outcomes as follows:

1. By using the CVD method, high-quality and atom-thin tellurides including monolayer $MoTe_2$ and WTe_2 with lateral size over 300 μm were synthesized.

Atomic structure of the $MoTe_2$ and WTe_2 were studied by scanning transmission electron microscope (STEM). The as-grown WTe_2 shows two different stacking sequences in the bilayer. A novel semimetal-to-insulator transition is observed in WTe_2 layers, while few-layer $MoTe_2$ shows superconductivity with a zero resistance below 0.5 K, a much higher transition temperature than the bulk $MoTe_2$ (0.1 K). This work paves the way to synthesize atom-thin tellurides and fabricate quantum spin Hall devices.

2. 2D TMDs, including monolayer TiS_2, few layer $TiSe_2$, few layer $TiTe_2$, monolayer VS_2, few layer VSe_2, few layer VTe_2, monolayer NbS_2, monolayer $NbSe_2$ and few layer $NbTe_2$ were synthesized by a designed molten salt-assisted CVD method. Their growth mechanism has been studied.
3. The vertically heterostructure between monolayer $PtSe_2$ and $MoSe_2$ was synthesized via one step by CVD method. The strong coupling epitaxial growth behavior was the key role for the second layer $PtSe_2$ growth, which is for the first time reported about the monolayer group-10 TMDs's single crystal. The monolayer $PtSe_2$ shows a typical p type property. The p-n junction formed between p type $PtSe_2$ and n type $MoSe_2$.
4. Monolayer In_2Se_3 was prepared by PVD method. Strong Raman and PL signal were observed from monolayer In_2Se_3, which have not been reported yet. In addition, back-gating filed-effect transistors (FETs) were fabricated using In_2Se_3 few layer, showing p-type behaviors and a mobility up to 2.5 cm^2/Vs. Such devices exhibit a high photoresponsivity up to 340A/W, plus fast response time 6 ms for the rise and 12 ms for the fall.

References

[1] K. S. Novoselov, A. K. Geim, S. V. Morozov, D. Jiang, Y. Zhang, S. V. Dubonos, I. V. Grigorieva, A. A. Firsov, Science 2004, 306, 666.

[2] A. A. Balandin, S. Ghosh, W. Z. Bao, I. Calizo, D. Teweldebrhan, F. Miao, C. N. Lau, Nano Lett 2008, 8, 902.

[3] A. K. Geim, K. S. Novoselov, Nat Mater 2007, 6, 183.

[4] F. Bonaccorso, L. Colombo, G. H. Yu, M. Stoller, V. Tozzini, A. C. Ferrari, R. S. Ruoff, V. Pellegrini, Science 2015, 347.

[5] C. Lee, X. D. Wei, J. W. Kysar, J. Hone, Science 2008, 321, 385.

[6] F. N. Xia, T. Mueller, Y. M. Lin, A. Valdes-Garcia, P. Avouris, Nat Nanotechnol 2009, 4, 839.

[7] M. F. El-Kady, V. Strong, S. Dubin, R. B. Kaner, Science 2012, 335, 1326.

[8] X. M. Li, T. S. Zhao, Q. Chen, P. X. Li, K. L. Wang, M. L. Zhong, J. Q. Wei, D. H. Wu, B. Q. Wei, H. W. Zhu, Phys Chem Chem Phys 2013, 15, 17752.

[9] M. Q. Zhao, Q. Zhang, J. Q. Huang, G. L. Tian, J. Q. Nie, H. J. Peng, F. Wei, Nat Commun 2014, 5.

[10] I. Meric, M. Y. Han, A. F. Young, B. Ozyilmaz, P. Kim, K. L. Shepard, Nat Nanotechnol 2008, 3, 654.

[11] K. F. Mak, C. Lee, J. Hone, J. Shan, T. F. Heinz, Phys Rev Lett 2010, 105.

[12] S. S. Pershoguba, V. M. Yakovenko, Phys Rev B 2012, 86.

[13] W. Z. Bao, X. H. Cai, D. Kim, K. Sridhara, M. S. Fuhrer, Appl Phys Lett 2013, 102.

[14] Q. H. Wang, K. Kalantar-Zadeh, A. Kis, J. N. Coleman, M. S. Strano, Nat Nanotechnol 2012, 7, 699.

[15] H. L. Zeng, J. F. Dai, W. Yao, D. Xiao, X. D. Cui, Nat Nanotechnol 2012, 7, 490.

[16] K. F. Mak, K. L. He, J. Shan, T. F. Heinz, Nat Nanotechnol 2012, 7, 494.

[17] T. Cao, G. Wang, W. P. Han, H. Q. Ye, C. R. Zhu, J. R. Shi, Q. Niu, P. H. Tan, E. Wang, B. L. Liu, J. Feng, Nat Commun 2012, 3.

[18] K. F. Mak, K. L. McGill, J. Park, P. L. McEuen, Science 2014, 344, 1489.

[19] M. Eginligil, B. C. Cao, Z. L. Wang, X. N. Shen, C. X. Cong, J. Z. Shang, C. Soci, T. Yu, Nat Commun 2015, 6.

[20] A. M. van der Zande, P. Y. Huang, D. A. Chenet, T. C. Berkelbach, Y. M. You, G. H. Lee, T. F. Heinz, D. R. Reichman, D. A. Muller, J. C. Hone, Nat. Mater. 2013, 12, 554.

[21] X. Wang, Y. Gong, G. Shi, W. L. Chow, K. Keyshar, G. Ye, R. Vajtai, J. Lou, Z. Liu, E. Ringe, B. K. Tay, P. M. Ajayan, Acs Nano 2014, 8, 5125.

[22] C. Cong, J. Shang, X. Wu, B. Cao, N. Peimyoo, C. Qiu, L. Sun, T. Yu, Advanced Optical Materials 2014, 2, 131.

[23] Y. P. Qi, P. G. Naumov, M. N. Ali, C. R. Rajamathi, W. Schnelle, O. Barkalov, M. Hanfland, S. C. Wu, C. Shekhar, Y. Sun, V. Suss, M. Schmidt, U. Schwarz, E. Pippel, P. Werner, R. Hillebrand, T. Forster, E. Kampert, S. Parkin, R. J. Cava, C. Felser, B. H. Yan, S. A. Medvedev, Nat Commun 2016, 7.

[24] A. A. Soluyanov, D. Gresch, Z. J. Wang, Q. S. Wu, M. Troyer, X. Dai, B. A. Bernevig, Nature 2015, 527, 495.

[25] X. F. Qian, J. W. Liu, L. Fu, J. Li, Science 2014, 346, 1344.

[26] M. Y. Li, Y. M. Shi, C. C. Cheng, L. S. Lu, Y. C. Lin, H. L. Tang, M. L. Tsai, C. W. Chu, K. H. Wei, J. H. He, W. H. Chang, K. Suenaga, L. J. Li, Science 2015, 349, 524.

[27] K. Chen, X. Wan, J. X. Wen, W. G. Xie, Z. W. Kang, X. L. Zeng, H. J. Chen, J. B. Xu, Acs Nano 2015, 9, 9868.

[28] K. Chen, X. Wan, W. G. Xie, J. X. Wen, Z. W. Kang, X. L. Zeng, H. J. Chen, J. B. Xu, Adv Mater 2015, 27, 6431.

[29] X. F. Li, M. W. Lin, J. H. Lin, B. Huang, A. A. Puretzky, C. Ma, K. Wang, W. Zhou, S. T. Pantelides, M. F. Chi, I. Kravchenko, J. Fowlkes, C. M. Rouleau, D. B. Geohegan, K. Xiao, Sci Adv 2016, 2.

[30] Y. D. Yoo, Z. P. Degregorio, J. E. Johns, J Am Chem Soc 2015, 137, 14281.

[31] T. Zhang, B. Jiang, Z. Xu, R. G. Mendes, Y. Xiao, L. F. Chen, L. W. Fang, T. Gemming, S. L. Chen, M. H. Rummeli, L. Fu, Nat Commun 2016, 7.

[32] Y. J. Gong, J. H. Lin, X. L. Wang, G. Shi, S. D. Lei, Z. Lin, X. L. Zou, G. L. Ye, R. Vajtai, B. I. Yakobson, H. Terrones, M. Terrones, B. K. Tay, J. Lou, S. T. Pantelides, Z. Liu, W. Zhou, P. M. Ajayan, Nat Mater 2014, 13, 1135.

[33] X. D. Duan, C. Wang, J. C. Shaw, R. Cheng, Y. Chen, H. L. Li, X. P. Wu, Y. Tang, Q. L. Zhang, A. L. Pan, J. H. Jiang, R. Q. Yu, Y. Huang, X. F. Duan, Nat Nanotechnol 2014, 9, 1024.

[34] C. M. Huang, S. F. Wu, A. M. Sanchez, J. J. P. Peters, R. Beanland, J. S. Ross, P. Rivera, W. Yao, D. H. Cobden, X. D. Xu, Nat Mater 2014, 13, 1096.

Chapter 2

Literature Review

This chapter reviews the progress on synthesizing 2D materials. The problems of normal chemical vapor deposition not being able to synthesize the remaining 40 types of 2H/1T/1T′ 2D materials which shows unique properties (semiconducting, superconducting, ferromagnetic) are illustrated. Based on these critical problems, the improved methods for synthesis of 2D materials and heterostructure are presented as follows: 1) using mixed compound of $MoCl_5$, MoO_3 and Te (or WCl_6, WO_3 and Te) for preparation of $MoTe_2$ (WTe_2); 2) using molten salt-assisted chemical vapor deposition method for synthesis of TiX_2, VX_2 and NbX_2 (X: S, Se and Te); 3) using one-step chemical vapor deposition method for synthesis of $PtSe_2/MoSe_2$ heterostructure; 4) using physical vapor deposition method for synthesis of In_2Se_3 monolayer. Third, the contents in the thesis based on literature are discussed.

2.1 Overview

Layered materials have been studied for more than 150 years. Owning to the monolayer graphene obtained by Geim using mechanical exfoliation method,[1] 2D materials have drawn intensive attention due to their unique properties when thinned to their physical limits. Although many studies focusing on the graphene have been devoted due to its exceptional optoelectronic, electronic, electrochemical and others applications,[2] the gapless of the monolayer graphene with low on/off ratio limits its application in field effect transistor (FET).[1] While the 2D TMDs with tunable band gap which can offset the gapless of graphene have drawn more and more attention.

TMDs have a formula of MX_2, where M stands for transition metal element and X stands for S, Se or Te.[3] One plane of hexagonally arranged transition metal atoms is sandwiched by two planes of hexagonally arranged chalcogen atoms, forming an MX_2 monolayer (Figure 2.1a).

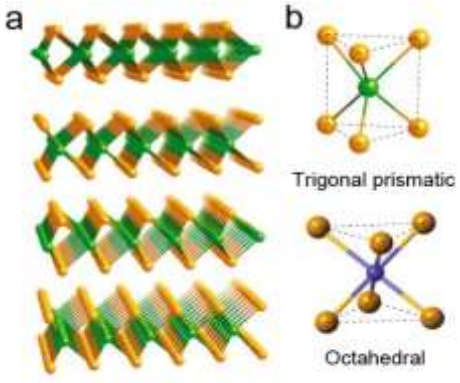

Figure 2.1 (a) A typical layered structure of MX_2, where metal atom is in green and chalcogen atom is in orange. (b) Two types of the local coordination of the metal atoms.[4]

In the TMD family, there are three typically crystal structures (2H, 1T and 3R), where the letter H, T and R stand for hexagonal, tetragonal and rhombohedral symmetry, respectively.[5] The numbers indicate the layer number in the unit cell. In addition, in the 2H and 3R polytypes, atoms in one layer are arranged in the trigonal prismatic geometry,

while in the 1T polytype, atoms are arranged in the octahedral geometry (Figure 2.2). Meanwhile, the two phases 1T′ and 1T″ are obtained distorted from 1T phase such as 1T′-WTe_2 and 1T″ $ReSe_2$, as shown in Figure 2.3. The electronic band structure of TMDs is mainly determined by the coordination geometry, whose stability is then influenced by the number of d-electrons.[3] For group 4, 7 and 10 TMDs, the D_{3d} symmetric octahedral geometry is preferable where two degenerate orbitals are formed ($d_{xy,yz,xz}$ and d_{z^2,x^2-y^2}). For group 5 and 6 TMDs, the D_{3h} symmetric trigonal prismatic geometry is preferable where three degenerate orbitals are formed ($d_{z^2}, d_{x^2-y^2,xy}$ and $d_{yz,xz}$). The electronic properties of TMDs are determined by how these bands are filled. For the TMDs, four electrons of metal atom are used to form bonds with chalcogens. Thus the number of nonbonding d-electrons is 0, 1, 2, 3 and 6 for group 4, 5, 6, 7 and 10 TMDs, respectively. As shown in Figure 2.4, for the group 6 TMDs with the D_{3h} symmetry, the d_{z^2} band is fully filled and as a result these materials are semiconducting, such as the 2H-MoS_2 and 2H-WS_2. On the other hand, for the group 5 TMDs with the D_{3h} symmetry, the d_{z^2} band is half filled and as a result these materials are metallic, such as the 2H-$NbSe_2$ and 2H-TaS_2.

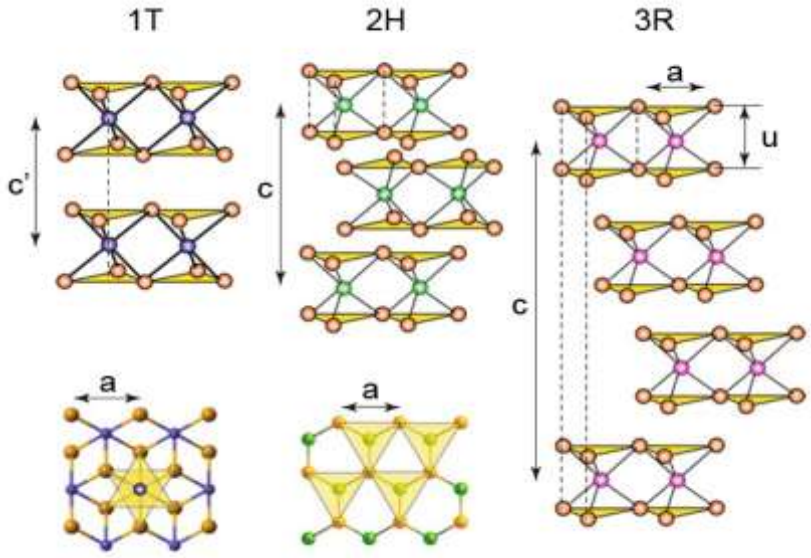

Figure 2.2 Structures of 1T (one layer per repeat, tetragonal symmetry), 2H (two layers per repeat, hexagonal symmetry) and 3R (three layers per repeat, rhombohedral symmetry) polytypes of TMD.[4]

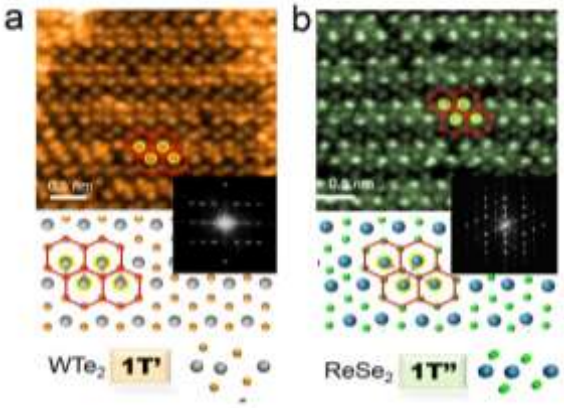

Figure 2.3 The atomic structure of WTe_2 and $ReSe_2$, indicating the 1T′ phase of WTe_2 and 1T″ phase of $ReSe_2$.

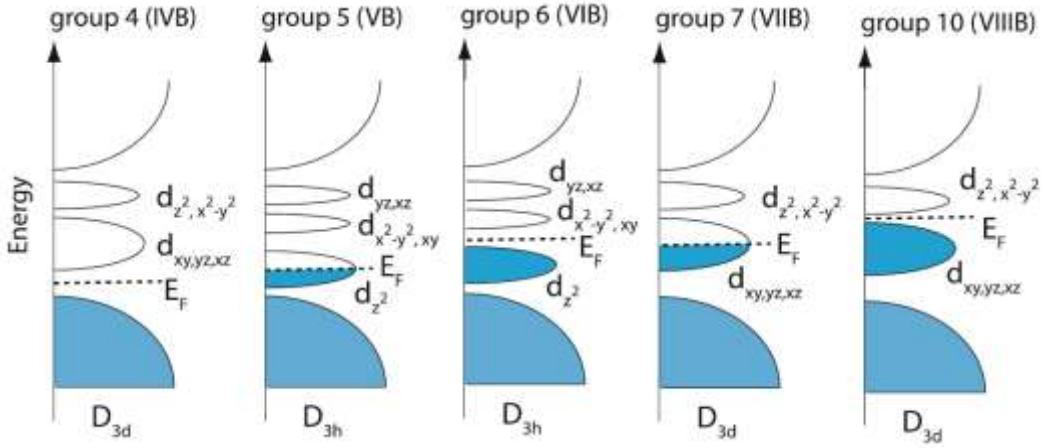

Figure 2.4 Schematic density of states of layered TMDs in group 4-7 and 10.[6]

So far, more than 40 different types of the 2D TMDs have been predicted or prepared by the traditional chemical vapor transfer (CVT) method.[7] Meanwhile, there are many layered materials that go beyond TMDs, including MXenes, monoelemental 2D semiconductors (silicene, phosphorene, germanene), monochalcogenides (InSe, GaSe, etc.), In_2Se_3, and heterostructures formed by stacking these 2D TMDs layer-by-layer in sequence or with in-plane junctions, as shown in Figure 2.5 and table 2.1

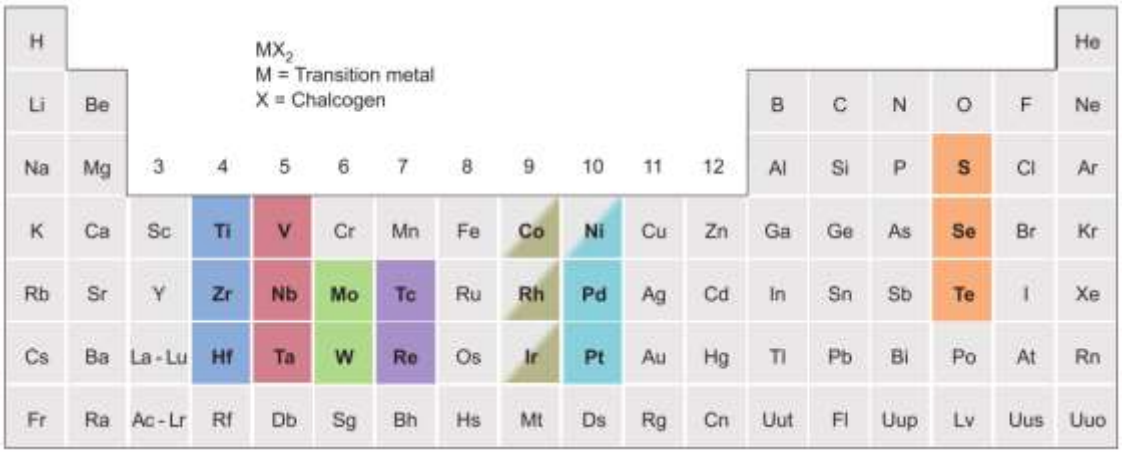

Figure 2.5 Summary of layered TMDs. The corresponding elements are highlighted in the period table. For Co, Rh, Ir and Ni, they can only form layered structures with some of the chalcogens.[3]

Table 2.1 Layered crystal structures that have been or can be mechanically exfoliated.[8]

Group IV	Dichalcogenides	Trichalcogenides	Oxides	Halides	Potential 2D
Graphene C	VSe_2, $NbSe_2$,	Bi_2Se_3, Bi_2Te_3,	MoO_3, V_2O_5,	$FeCl_3$,	**Zintl Hosts**
Graphane CH	TiS_2, ZrS_2, HfS_2,	Sb_2Te_3, Bi_2S_3,	WO_3, ...	$FeBr_3$,	$CaSi_2$, $CaGe_2$,
Fluorographene CF	ReS_2, PtS_2,	In_2Se_3, As_2S_3,		$CrCl_3$,	$Ca(Si_{1-x}Ge_x)_2$
Silicene Si	$TiSe_2$, $ZrSe_2$,	As_2Se_3, $NbSe_3$,	**Nitrides**	$CrBr_3$,	$Ba_3Sn_4As_6$
Germanane GeH	$HfSe_2$, $ReSe_2$,	TiS_3, ZrS_3, $ZrSe_3$,	BN	$MoCl_3$,	$CaMg_2N_2$
	$PtSe_2$, $SnSe_2$,	$ZrTe_3$, HfS_3,		$MoBr_3$,	$CaIn_2$
	$TiTe_2$, $ZrTe_2$,	$HfSe_3$, $HfTe_3$,	**Oxychlorides**	$TiCl_2$,	$CaNi_2P_2$
MXenes	VTe_2,$NbTe_2$,	NbS_3, TaS_3,	BiOCl, FeOCl,	$TiBr_3$,	$CaAuGa$, ...
Ti_3C2,Ti_2C, Ta_4C_3,	$TaTe_2$, $MoTe_2$,	$TaSe_3$, ...	HoOCl, ErOCl,	$InBr_3$,	
$Ti_3(Co_{.5}No.5)2$, ...	WTe_2, $CoTe_2$,		ErOCl, TmOCl,	PbI_2,	
	$RhTe_2$, $IrTe_2$,	**Mono-Chalcogenides**	YbOCl, LnOCl, ...	$A1Cl_3$3,	
	$NiTe_2$, $PdTe_2$,	GeSe, GeTe,	**Layered Silicate**	$InBr_3$3,	
	$PtTe_2$, $SiTe_2$,	GaSe, GaS	**Minerals**	$CrBr_3$3,	
	NbS_2, TaS_2,		Egyptian Blue, ...	$FeCl_2$,	
	MoS_2, WS_2,	**Thiophosphates**		$MgCl_2$,	
	$TaSe_2$, $MoSe_2$,	FePS3, MnPS3,		$CoCl_2$,	
	WSe_2, $MoTe_2$,	NiPS3, ...		$VC1_2$,	
	$SnSe_2$, SnS_2, ...			VBr_2, VI_2	
				$CdCl_2$,	
				CdI_2, ...	

Due to the polytype and the number of d-electrons of the transition metal element are different,[3] TMDs show rich physical and chemical properties including semiconducting,[9] semi-metallic,[10] metallic,[11] superconducting[12, 13] and charge density wave (CDW) behaviors (Table 2.2).[13] By now, TMDs have shown a great potential in many research areas,[10-23] such as electronics, optoelectronics, nonlinear optics, flexible devices, energy

storage and sensor applications. Synthesis of large monolayer of 2D TMDs is very important for exploiting their properties and applications.

Table 2.2 Electronic properties of different layered TMDs. The ρ stands for the in-plane electrical resistivity.[3]

Group	M	X	Properties
4	Ti, Hf, Zr	S, Se, Te	Semiconducting (E_g = 0.2–2 eV). Diamagnetic.
5	V, Nb, Ta	S, Se, Te	Narrow band metals (ρ ~ 10^{-4} Ω.cm) or semimetals. Superconducting. Charge density wave (CDW). Paramagnetic, antiferromagnetic, or diamagnetic.
6	Mo, W	S, Se, Te	Sulfides and selenides are semiconducting (E_g ~ 1 eV). Tellurides are semimetallic (ρ ~ 10^{-3} Ω cm). Diamagnetic.
7	Tc, Re	S, Se, Te	Small-gap semiconductors. Diamagnetic.
10	Pd, Pt	S, Se, Te	Sulfides and selenides are semiconducting (E_g = 0.4 eV) and diamagnetic. Tellurides are metallic and paramagnetic. $PdTe_2$ is superconducting.

2.1.1 Synthesis and properties of VI-based TMDs

The transition metal dichalcogenide (TMDC) monolayers (MX_2) have three atom layers with a transition metal atom such as Mo or W sandwiched by two layers of chalcogen atom layer (such as S, Se, or Te). In order to produce the monolayer of these TMDCs, the methods including the top-down and bottom-up have been used. The top-down methods such as the mechanical exfoliation,[24] electrochemical and chemical exfoliation or direct sonication in solvents, only can produce few-layer crystals with small size and low quality.[25, 26] The bottom-up methods including the CVD and PVD method have been used to synthesis of large-size 2D TMDs monolayer on SiO_2 substrate.[27] As for the CVD method, there are two routes that are used to synthesize large-size 2D TMDs.[28] The first is considered as two-step growth routes, in which the precursors of Mo or W are deposited on the substrate first, and then react with chalcogens such as S, Se or Te. The second route is that the metal oxides or metal chlorides react with the chalcogens directly, and then the products deposit on the substrate. The two routes used for synthesis of MoS_2 are summarized in Figure 2.6.[28]

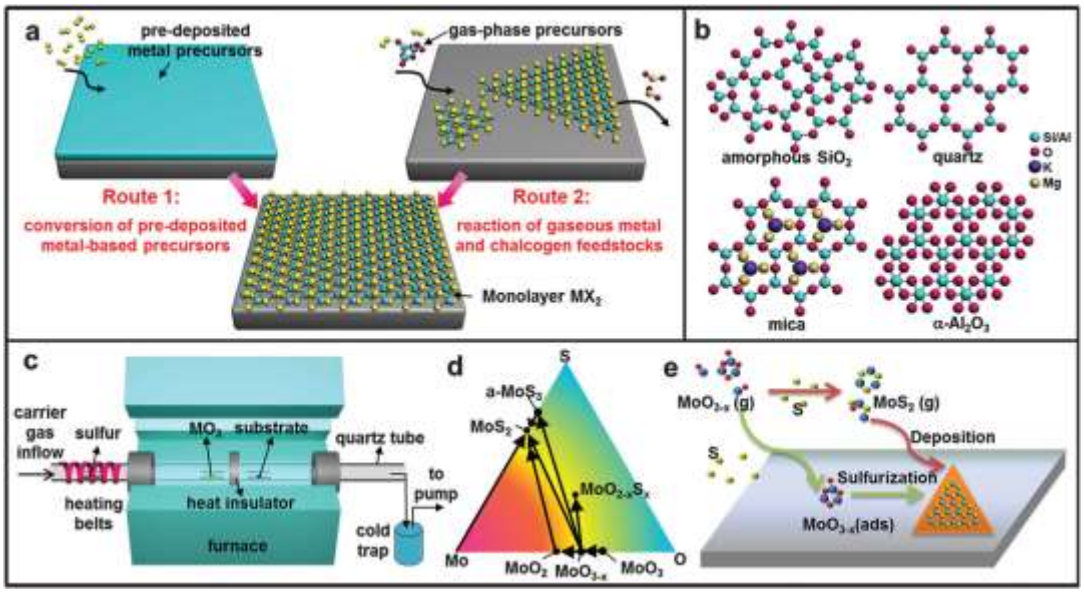

Figure 2.6 CVD system was used for synthesis of MX_2. (a) Two routes for MX_2 synthesis. (b) Commonly used insulating substrates for MX_2 growth (top view). (c) Typical setup of a LPCVD system. (d) Mo–O–S ternary phase diagram, in which the labelled arrows indicate reaction pathways for the CVD growth of MoS_2 from MoO_3 precursors. (e) Possible growth processes of MoS_2 by the reaction of MoO_{3-x} and S.

For the route one, which has been used to synthesize MoS_2, $MoTe_2$ and so on. For example, Lou's group has reported that the Mo layers deposited by e-beam evaporation on substrate first, and then sulfuration of the pre-deposited Mo layers, they obtained the few-layer MoS_2.[29] Similarly, MoO_2 and NH_4MoO_4 were used as the precursors and deposited on the substrate first, and then reacted with S. The MoS_2 flakes with different thickness were obtained.[30] $MoTe_2$ with different phases were reported by Lee's group via using the route one. They deposited the Mo film with different thickness, and then tellurization of the pre-deposited Mo film.[31] However, the route one cannot be used to prepare the single crystals. In contrast, people have used the route-two to prepare the monolayer MoS_2, $MoSe_2$, WS_2, WSe_2 single crystals successfully. In the route-two, the sulfur, selenium and the metal oxides such as MoO_3 and WO_3 are used as the precursors. The sources are put in the reaction chamber with different temperature. The Ar or Ar/H_2 is used as the carrier gas. For example, large monolayer MoS_2 was produced by Ajayan's group using the MoO_3 and

S as the sources. $MoSe_2$ was synthesized by using MoO_3 and Se as the reaction sources and the H_2/Ar as the carrier gas at the high temperature about 750 ºC. Yu's group reported that they could synthesize the monolayer WS_2 under temperature of 750 ºC using WO_3 and S as the sources.[32] The monolayer WSe_2 was reported by Luace Li' group under low pressure.[33]

Although these two routes have been used to prepare the MX_2 (M: Mo, W and X: S, Se, Te), however, which have common characteristics that metal sources deposit on the substrate and then reaction with the S/Se/Te or using the metal oxides evaporate at high temperature. The two routes cannot be used to prepare the $MoTe_2$ and WTe_2 single crystals due to the low chemical reactivity of Mo and W and their decomposition properties at high temperature(Such as WTe_2).

Transition metal ditellurides, such as tungsten ditelluride (WTe_2) and molybdenum ditelluride (1 T′-$MoTe_2$), are layered semimetals from transition metal dichalcogenides (TMD-Cs). In sharp contrast to the semiconducting sulfide and selenide compounds such as 2H MoS_2, $MoSe_2$, WS_2 and WSe_2, tellurides exhibit much richer structural variations and electronic properties from semiconducting 2H phase to semi-metallic 1T′ phase. Among all telluride compounds, WTe_2 and $MoTe_2$ crystal can maintain a stable layered 1T′ phase in nature. They have been considered as promising candidates of type-II Weyl materials (as shown in Figure 2.7).[34, 35] Meanwhile, large and non-saturating magnetoresistance has been reported in WTe_2 bulk, as shown in Figure 2.8.[36] An Ohmic homojunction between 2H and 1T′ $MoTe_2$ has been demonstrated, as shown in Figure 2.9.[37] The mobility of $MoTe_2$ and WTe_2 up to 4000 cm^2/Vs and 10000 cm^2/Vs has been reported. Moreover, monolayer WTe_2 and $MoTe_2$ have been predicted to be 2D topological insulators, as shown in Figure 2.10.[38] All these novel phenomena in $MoTe_2$ and WTe_2 have attracted tremendous interest.[34] Although telluride compounds such as $MoTe_2$ films were successfully synthesized by thermal flux and tellurization of molybdenum films,[31, 39, 40] controlling synthesis of high-quality telluride atomic layers, even down to monolayer, remains elusive under the existing CVD or PVD conditions, mainly due to the lower environmental stability and reaction activity of tellurium. For instance, the low chemical

reaction activity of W and Mo with Te limits tellurization of W and Mo precursors (powder and oxides), although this method has been widely adopted for the preparation of sulfide and selenide monolayers. More specifically, the electronegativity difference between transitional metal (W or Mo) and Te is very small (~ 0.4 eV or 0.3 eV), indicating a weak bonding between the metals and Te atoms, which makes the stoichiometry of ditellurides difficult to be obtained. Furthermore, even though the stoichiometry of WTe_2 and $MoTe_2$ is maintained, the as-synthesized product tends to decompose rapidly by emitting Te vapor at high reaction temperature (around 600 ºC),[41] instead of evaporating into gas-phase telluride. As a result, synthesizing monolayer $MoTe_2$ and WTe_2 is very difficult by the traditional CVD or PVD method.

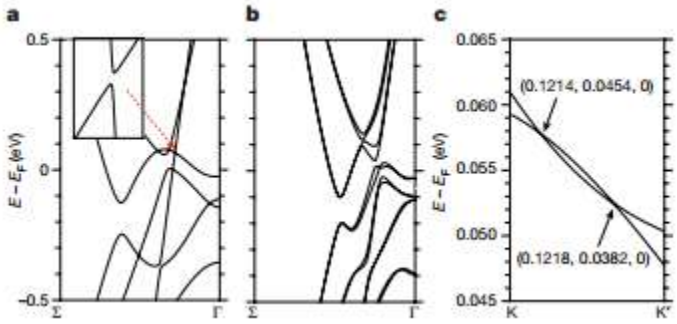

Figure 2.7 Band structure of WTe_2, indicating the WTe_2 is a type-II Weyl semimetal.

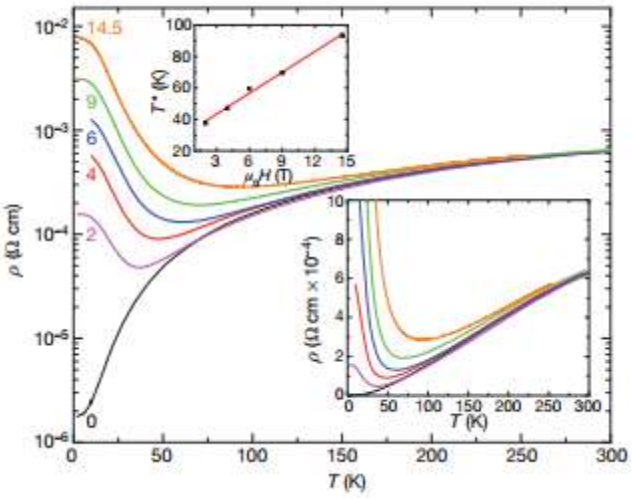

Figure 2.8 Large and non-saturating magnetoresistance in WTe_2.

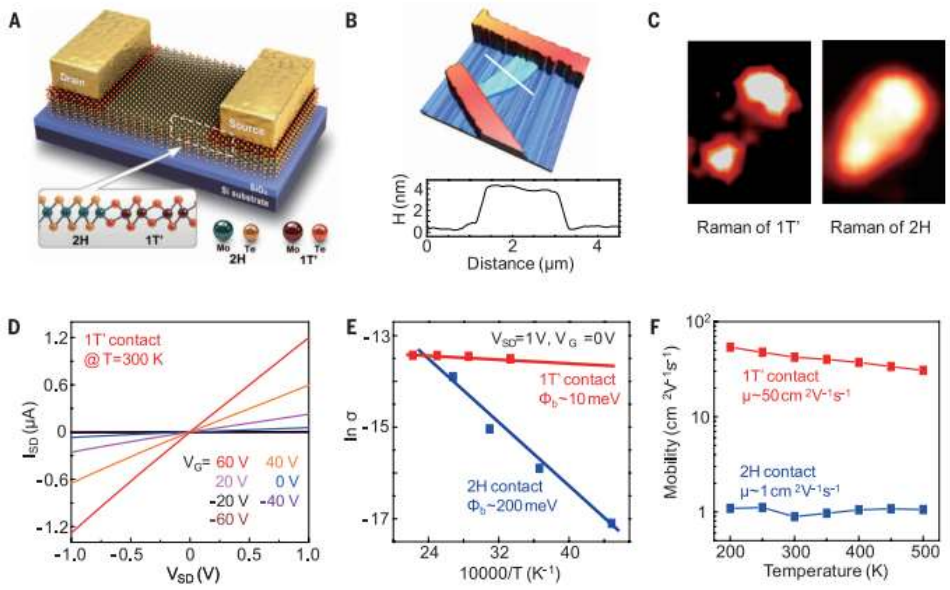

Figure 2.9 Ohmic homojunction between 2H and 1T′ $MoTe_2$

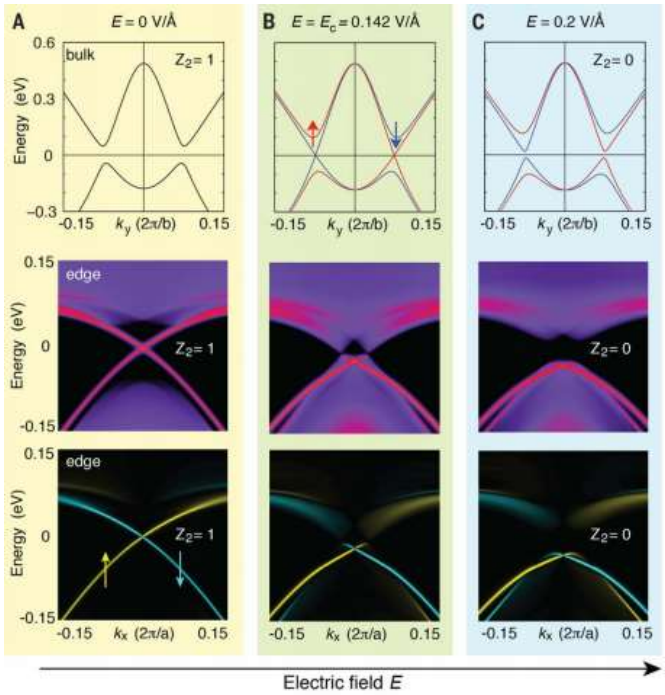

Figure 2.10 a topological phase transition in 2D TMDs.

2.1.2 Synthesis and properties of TiX_2, VX_2 and VX_2

TiX_2: Similar with the 2D TMDs in group VI. TiX_2, VX_2 and NbX_2 (X: S, Se, Te) are all layered materials. The TiX_2 includes TiS_2, $TiSe_2$ and $TiTe_2$. TiS_2 is a semiconductor with a small band gap.[42] Monolayer layer TiS_2 consists of S-Ti-S layers, which has been considered as a promising candidate for potential electronic applications because of its electronic structure. Theoretical work also showed that the high-conductive properties existing in TiS_2 crystal. Moreover, TiS_2 ultrathin nanosheets showed the ultrahigh conductivity in the field of electrodes[43] and potential application in the hydrogen evolution reaction.[44] The high electrical conductivity was also realized in the organic/TiS_2 composites.[45] In order to synthesis of TiS_2, researcher has reported an approach to synthesize the two-dimensional nanocrystalline TiS_2 on Au (111) substrate. They found that the only TiS_2 islands were obtained, as shown in Figure 2.11.[42] TiS_2 nanotubes have been obtained by CVD method using the $TiCl_4$, H_2S and H_2 as the sources under the growing temperature about 450 ºC, the TEM images of the TiS_2 nanotubes are shown in Figure 2.12.[46] TiS_2 whiskers have also been reported by a simple CVD method on a Ni-coated Si substrate.[47] However, to date, synthesizing large few layer or monolayer TiS_2 has not been reported.

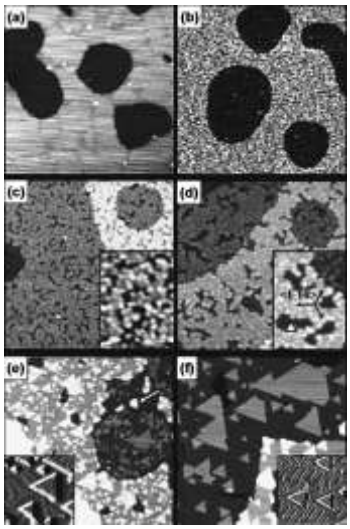

Figure 2.11 STM images (*Z*-channel) shows the formation of TiS_2 nanocrystals after deposition of Ti on AuS/Au(111). (a) as-prepared AuS film on Au(111) with a characteristic vacancy island pattern. (b) After deposition of 0.25 ML Ti at room temperature; consecutive heating to (c) 450 K, (d)550 K, (e) 670 K, and (f), 800 K for 10 minutes leads to the formation of TiS_2 nanocrystals.

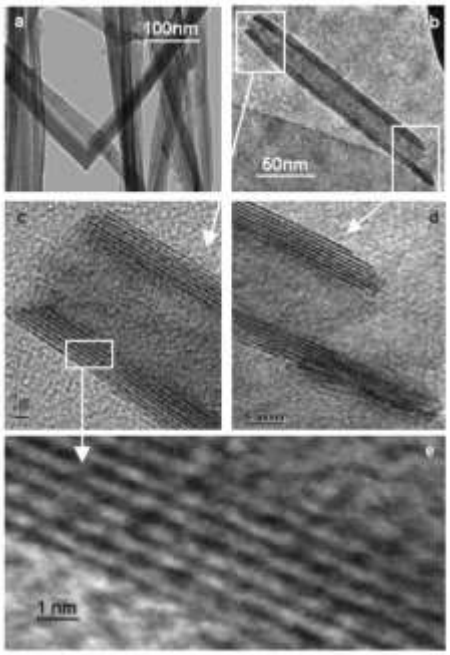

Figure 2.12 TEM and HRTEM images of the as-synthesized TiS_2 nanotubes. (a and b) low-magnification TEM images and (c, d, e) HRTEM images.

Compared with TiS_2, $TiSe_2$ has a CDW order when temperature was cooled below a transition temperature TCDW=202 K. The CDW phase could be suppressed by applying hydrostatic pressure or by intercalation of Cu atoms.[48] Researchers found that the CDW domain walls of $TiSe_2$ also appear above the superconducting temperature when add the press at P=3 GPa, as shown in Figure 2.13.[49] Especially, the CDW and superconducting phases of $TiSe_2$ can be tuned by the electric-field effect. The CDW order has been observed in exfoliated $TiSe_2$ monolayer characterized by Raman spectra.[50] However, all these studies focus on the $TiSe_2$ bulk crystals or $TiSe_2$ few layer obtained by mechanical exfoliation method. In order to study the properties in few layer or monolayer $TiSe_2$, Jiao's group has tried to synthesize the few layer $TiSe_2$ by CVT method, as shown in Figure 2.14.[51] Synthesis of large few layer or monolayer $TiSe_2$ is very important for study its novel properties. For the $TiTe_2$, the structure is similar to the TiS_2 and $TiSe_2$, however, only few studies about $TiTe_2$ were made. Synthesis of $TiTe_2$ is urgent to study its topological phase transition and negative magnetoresistance.[52]

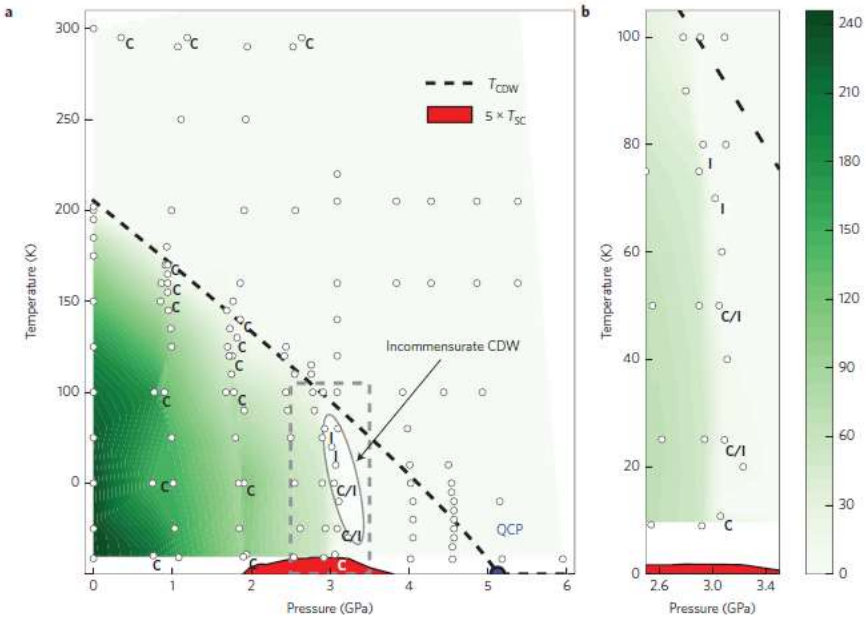

Figure 2.13 The pressure–temperature phase diagram of $TiSe_2$. (**a**) Charge density wave (CDW) ordered and the phase boundaries between normal state and superconducting. (**b**) Zoom-in on the region where exhibits the transition between commensurate and incommensurate order.

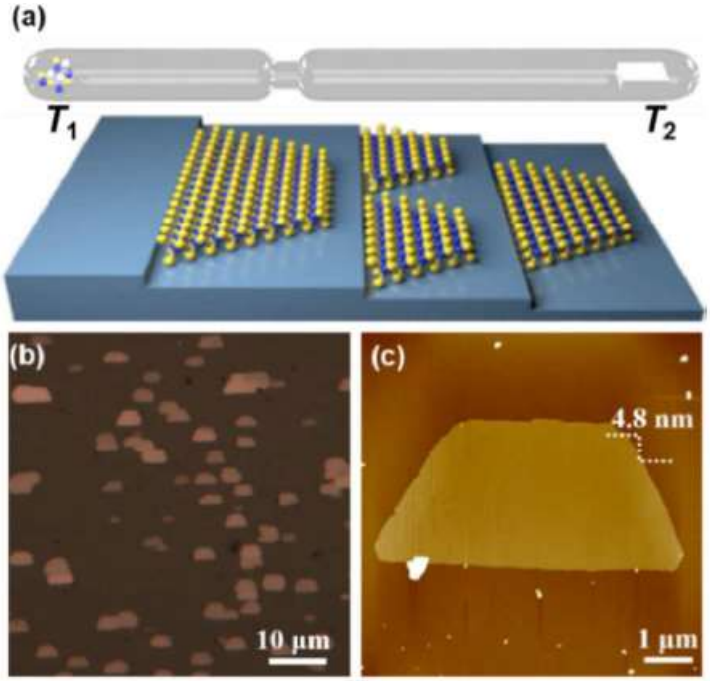

Figure 2.14 (a) Schematic for growth of 2D $TiSe_2$ using CVT method. (b and c) Optical and AFM images of the as-obtained $TiSe_2$ flakes.

VX_2: VX_2, is a transition metal dichalcogenide in group VB. The VX_2 has shown potential applications in energy storage devices. For example, Xie's group has reported that high two-dimensional conductivity of metallic few-layered VS_2 ultra nanosheets can be exfoliated from VS_2 crystals used for in-plane supercapacitors. Recently, VS_2 thick flakes show excellent properties in hydrogen evolution reaction. More importantly, theoretical results showed that VX_2 reveals magnetism in their monolayer, as shown in Figure 2.15.[53] Moreover, density functional theory (DFT) calculations showed that the phase changes from metal to semimetal when their thickness reduces to bilayer or monolayer. So far, researchers have studied the pristine magnetism in VX_2, for example, ultrathin nanosheets of VSe_2 showing the ferromagnetic CDW behavior has been reported by Xie's group, as shown in Figure 2.16.[54] Antiferromagnetic order was observed in V_5S_8.[55] However, there was rare work report about the ferromagnetic in monolayer VX_2 due to the difficulty of synthesizing monolayer VX_2. By now, only the thick VS_2 has been reported by CVD method, as shown in Figure 2.17.[56] Preparing monolayer VX_2 is urgent for study their pristine ferromagnetic properties.

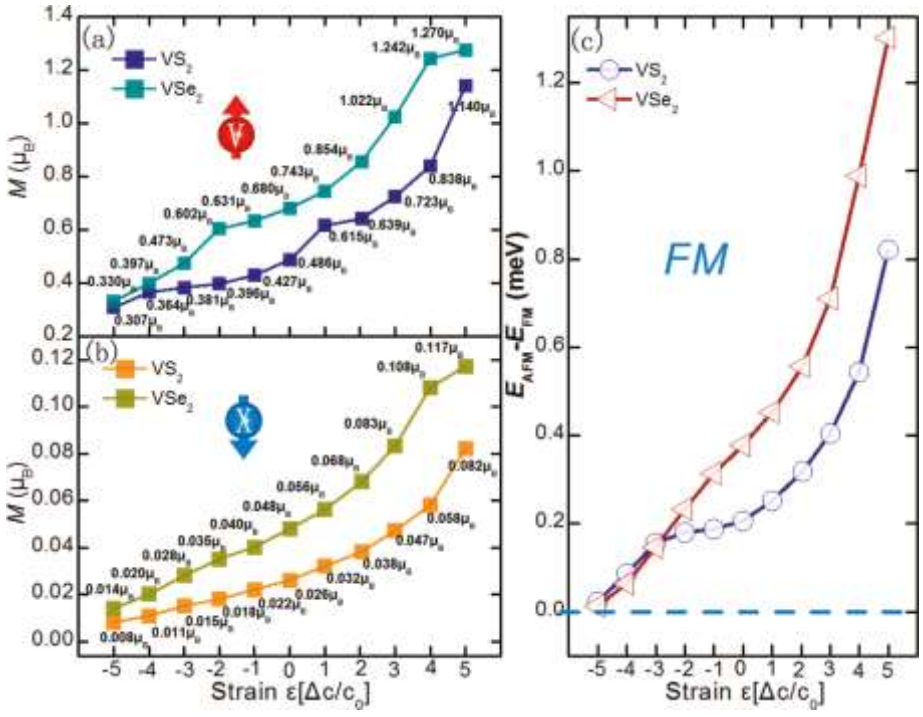

Figure 2.15 (a) The magnetic moment per X atom MX (b), and the energy difference between FM and AFM order (c) of VX_2 monolayers.

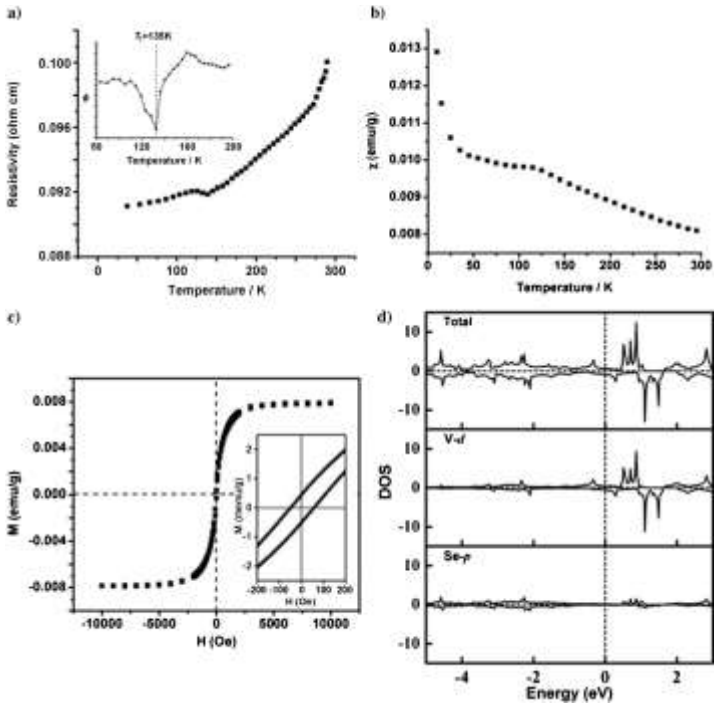

Figure 2.16 (a) Temperature dependence of resistance in the temperature range 80–200 K. (b) ZFC magnetization of the obtained ultrathin VSe_2 nanosheets. (c) M–H curves of VSe_2 nanosheets at 300 K. (d) TDOS and PDOS of VSe_2 monolayer.

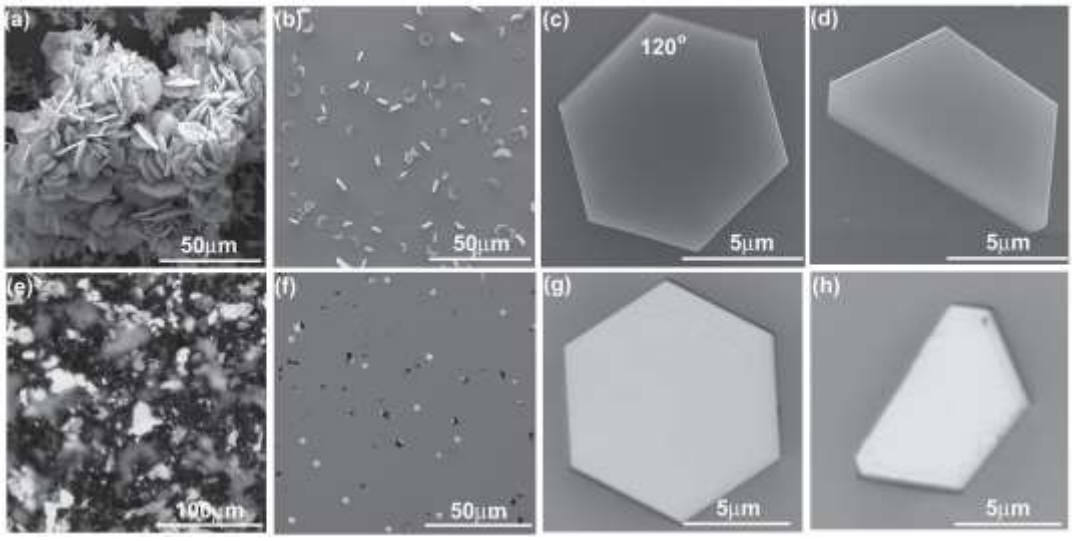

Figure 2.17 (a) Scanning electron microscope (SEM) images of VS_2 nanosheets, (b) SEM image of VS_2 with aligned parallel to the substrate, and (c) dominant hexagon and (d) nearly "half-hexagon" shape of VS_2. (e–h) Optical images of VS_2 crystals.

NbX_2: NbX_2 includes NbS_2, $NbSe_2$ and $NbTe_2$. The bulk NbX_2 exhibits metal properties. The CDW and superconducting transition behavior have been observed in NbX_2 bulk. For the NbS_2, two phases 2H and 3R are existed. For the $NbSe_2$, theoretical studies have predicted that CDW and superconductivity behavior also exist in monolayer NbX_2. For example, the enhanced CDW behavior has been observed in the exfoliated $NbSe_2$ monolayer (Figure 2.18) and has been confirmed by STM.[57] Furthermore, the strong evidence of unconventional Ising pairing protected by spin-momentum locking was observed in monolayer $NbSe_2$. Quantum metal in $NbSe_2$ was also reported. For the $NbTe_2$, which shows the same CDW and superconducting behavior as in the $NbSe_2$. Synthesis of large NbX_2 monolayer offers the platform to study their CDW and superconducting behavior. However, few papers reported about the preparation of NbX_2 to date. For example, $NbCl_5$ and S have been used to synthesizing NbS_2, however, only thick flakes with small size about 300 nm were obtained, as shown in Figure 2.19.[58] And then, the BN was used as the substrate for the growth of NbS_2, as shown in Figure 2.20.[59] However, the size is also small. Compared with NbS_2, the preparation of $NbSe_2$ has been prepared by MBE method, which cannot produce a large scale size. For the $NbTe_2$, there was not any paper reporting about its preparation by CVD or PVD method. Synthesizing the monolayer NbX_2 is very urgently for researchers to study their CDW behavior and applications in superconducting devices.

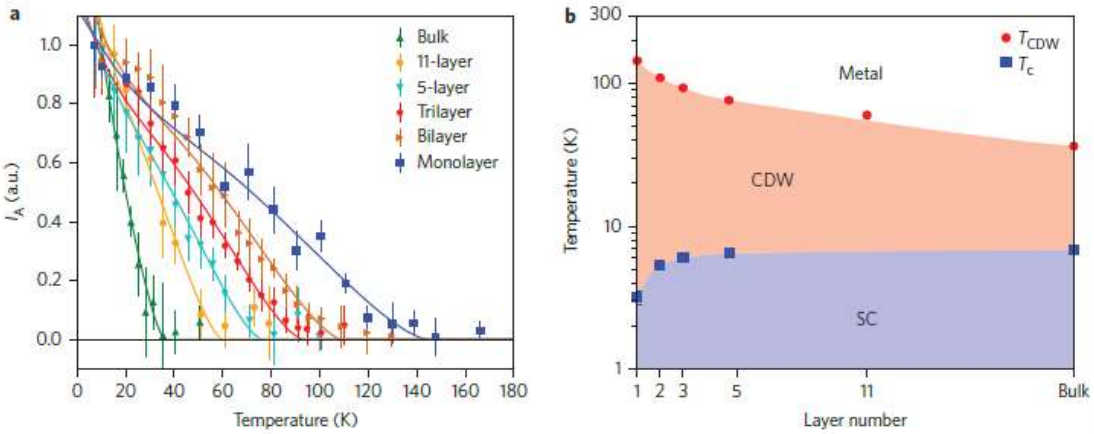

Figure 2.18 Many-body phase diagram of two-dimensional $NbSe_2$. (a) Temperature dependence of IA mode for $NbSe_2$. (b) The boundaries between the phases are guides to the eye.

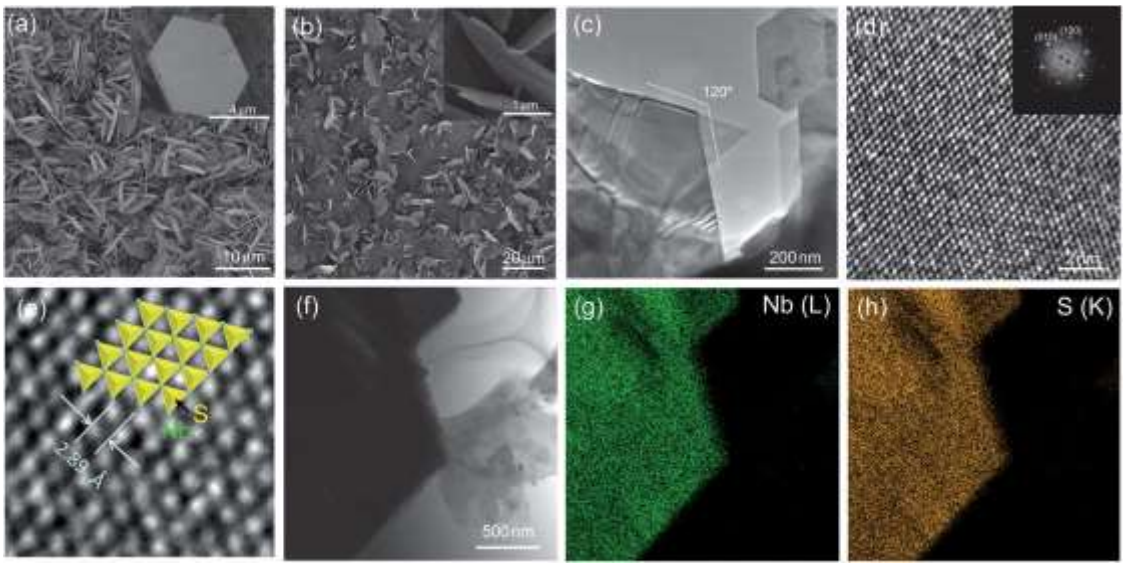

Figure 2.19 (a-b) SEM images (a, High density and b, Low density) of NbS_2 nanosheets. (c–e) TEM images of the NbS_2. (f) TEM image and mapping images of Nb (g) and S (h) elements.

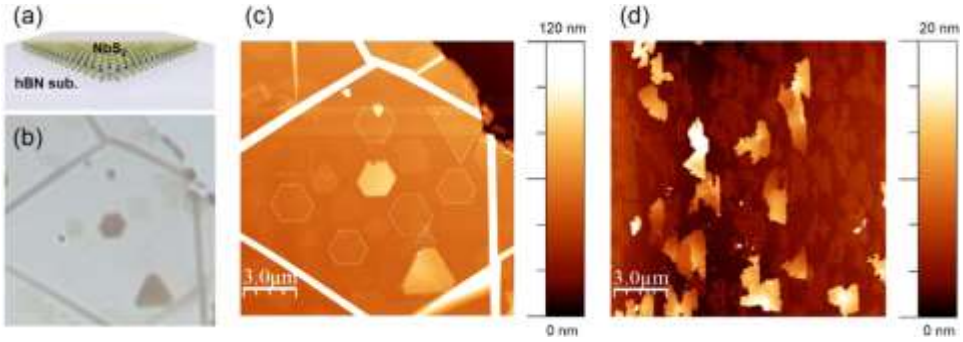

Figure 2.20 (a) Structure schematic for the growth of NbS_2. (b) Optical image of NbS_2. (c) AFM image. (d) AFM topographic image of NbS_2 flakes.

2.1.3 Synthesis, properties and applications of heterostructures

Due to the development of 2D TMDs, two dimensional transition metal dichalogenides heterostructures based on different 2D TMDs have drawn intensive attention due to their great potential applications in speed electronics, optoelectronic devices, transistors, sensors, photodetectors, LEDs and spin valleytronic devices.[60-66] Traditional 2D TMDs heterostructures are often obtained via combining the TMDs with different chemical composition and properties by sequential mechanical method, as shown in Figure 2.21,[67]

which has been used to fabricate the heterostructures such as $MoS_2/MoSe_2$, MoS_2/WS_2. However, these heterostructures show a small overlap in sample size and their interface contamination is difficult to avoid.

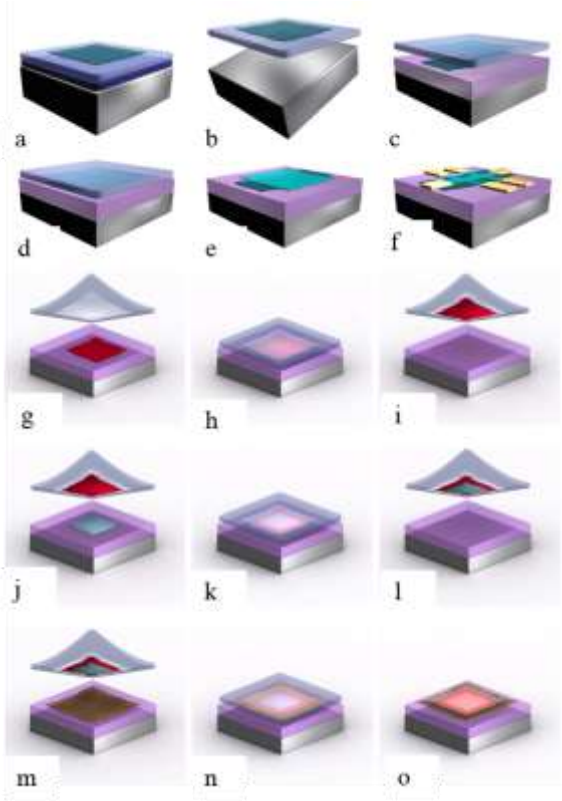

Figure 2.17 Wet-transfer and pick-and-lift techniques for assembly of van der Waals heterostructures. (a to f) Wet-transfer technique. (g to o) Pick-and-lift technique.

Chemical vapor deposition (CVD) method and physical vapor deposition (PVD) method have been successfully applied to produce the MoX_2/MX_2 heterostructures (MX_2, where M are the transition metals such as Mo or W, and X is S, or Se) via one step or two steps by vdW epitaxial method.[68-76] For example, the WS_2/MoS_2 vertically stacking and in-plane heterostructures were synthesized by CVD method, as shown in Figure 2.22.[74] WSe_2/MoS_2 heterostructure was produced by two steps CVD method, and shows a typical p-n junction as shown in Figure 2.23.[68] WS_2/WSe_2 ($MoS_2/MoSe_2$) and $MoSe_2/WSe_2$ heterostructures have been produced by PVD method, as shown in Figure 2.24 and Figure

2.25, respectively.[75, 76] However, the common characteristics of the heterostructures are based on that the monolayer TMDs single crystals can be prepared easily in a separated CVD process. More importantly, the similar lattice structures and constants offer the opportunity to form the MoX_2/MX_2 heterostructures with commensurate superlattice.

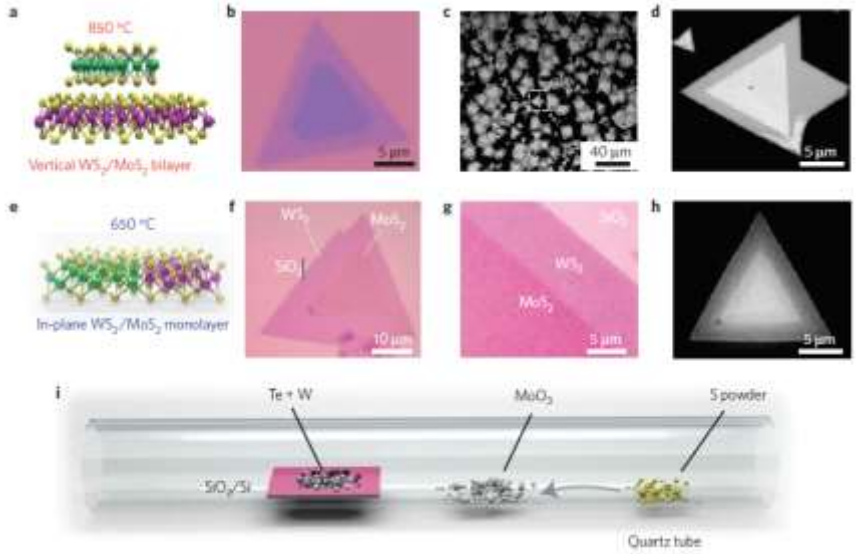

Figure 2.22 (a–h) Schematic, optical and SEM images of the vertically stacked and in-plane WS_2/MoS_2 heterostructures. (i) Schematic of the synthesis process for both heterostructures.

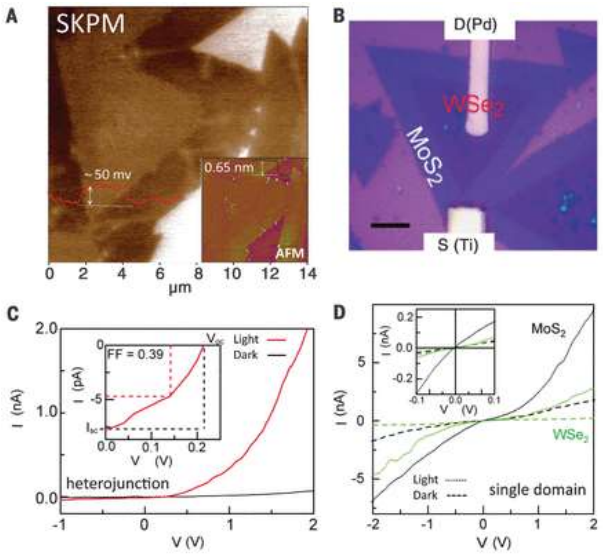

Figure 2.23 WSe_2/MoS_2 lateral heterojunction was synthesized by CVD method and showed a typical p-n junction.

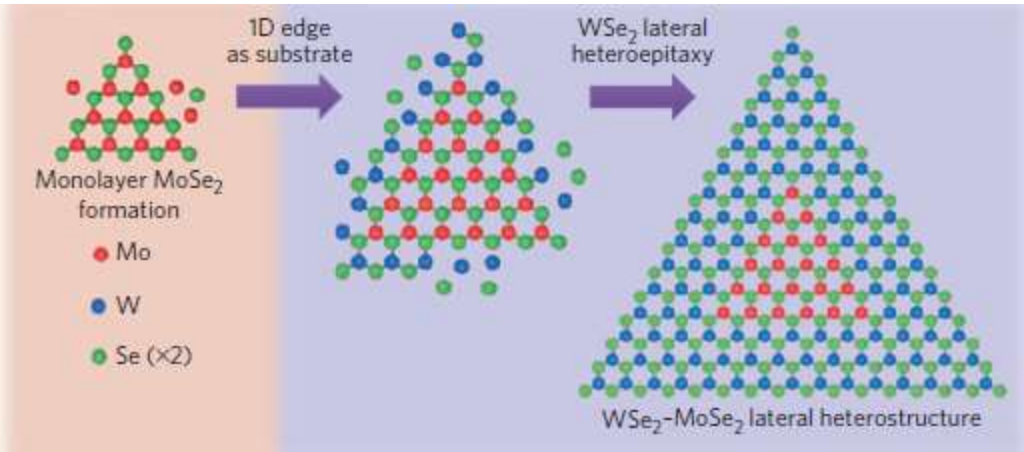

Figure 2.24 Synthesis of $WSe_2/MoSe_2$ lateral heterojunction by CVD method

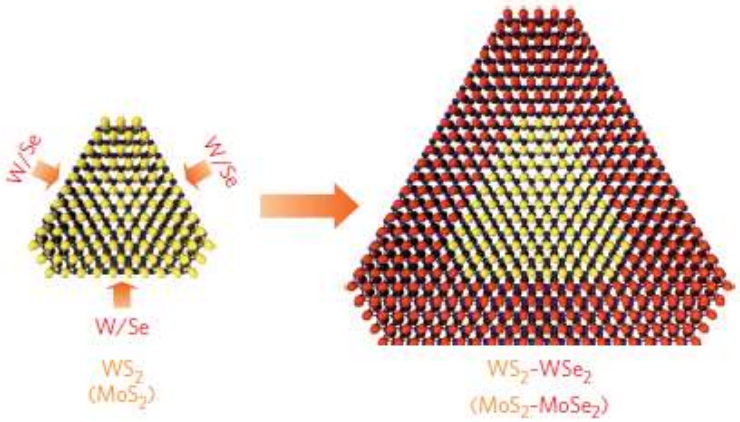

Figure 2.25 Schematic of lateral epitaxial growth of WS_2/WSe_2 and $MoS_2/MoSe_2$ heterostructures.

Recently, twinned growth behavior of vertical heterostructures between WS_2 and ReS_2 has been reported, as shown in Figure 2.26,[73] which opens a new route to synthesis of heterostructures with different crystal structure. However, the method has the similar characteristic as the method discussed above due to the monolayer ReS_2 single crystal can be synthesized separately. Moreover, the alloy foil formed is requested. So far, synthesis of the heterostrurctures, such as between MX_2 and group-10 TMDs (for example PtS_2, $PtSe_2$), cannot be realized due to the low chemical reactivity of Pt and Pd and their crystal structures are different from that of MX_2.

Group-10 TMDs have been demonstrated with a phase change from a semimetal in bulk to a semiconductor in monolayer with the band gap increasing from 0eV to 1.6eV and also demonstrated as a valid hydrogen evolution reaction activity.[77, 78] In addition, the theory predicted and experiment confirmed that high mobility and good air stability make them as typical candidates in the applications of field effect transistors (FETs).[79] Synthesis of group-10 TMDs as well as the heterostructure combined with MX_2, show the great opportunities to expand their properties and broad their applications. However, it is still a big challenge.

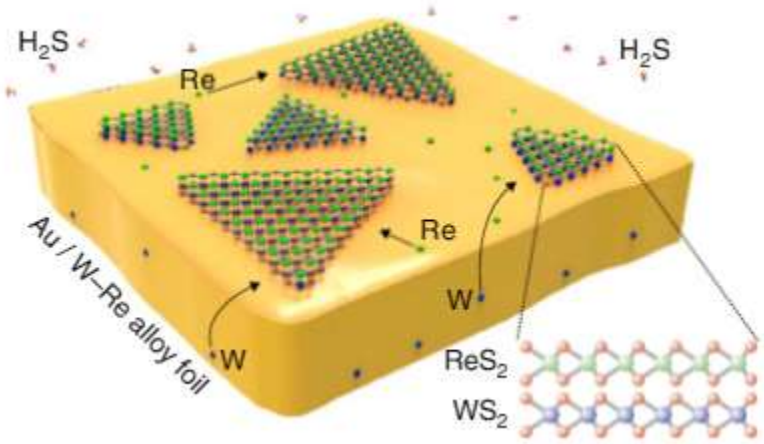

Figure 2.26 Schematic of vertically stacking growth of WS_2–ReS_2.

2.1.4 Synthesis and applications of In_2Se_3

In spite of substantial studies on TMDCs having been exerted, the non-transition metal chalcogenides such as In_xSe_y, Bi_2Se_3, Ga_xS_y, Bi_2Te_3 and Sb_2Te_3 were not studied in depth.[80-83] It is notable that these semiconductors show the exciting physics such as topological insulating effect and also excellent applications on energy, sensors and catalysis. The possible reasons for this overlooked because of the difficulty of synthesizing them by CVD method. For example, sulfides like MoS_2 and $MoSe_2$ were produced by CVD method while selenides and tellurides are more challenging due to low chemical reactivity and different reaction mechanism. Moreover, there are different chemical compositions, such as the InSe and In_2Se_3. More importantly, as for the In_2Se_3 or InSe, the difficulties in synthesizing monolayer originate from the fact that rich phases of In_xSe_y are easily

produced at high temperatures, such as InSe, $InSe_2$, In_2Se_3, In_3Se_4 and so on. Meanwhile, these 2D materials generally have many phases. For In_2Se_3, there are at least five known crystal forms (α, β, γ, δ and *k*) exist at various temperature,[82] which impede the researchers to identify the phase of the In_2Se_3. This problem especially cannot be overcome for the In_2Se_3 monolayer. As for the In_2Se_3, α phase is a layered crystallographic. The thickness of monolayer α-In_2Se_3 is ~ 1 nm.[84] The α → β phase transformation of In_2Se_3 has been studied for a few decades but most of the α-In_2Se_3 are amorphous and polycrystalline. The high-quality α-In_2Se_3 crystal is urgently required to clarify its phase transition. Meanwhile, the 1.3 eV of the direct-band gap of α-In_2Se_3 offers the opportunities to use in many applications such as nonvolatile phase change memory and optoelectronics.[85-89] So far, few growing technologies have been used to produce In_2Se_3 with various geometries. For instance, direct sputtering deposition has been used to prepare polycrystalline In_2Se_3 films in the past decades. And then, physical vapor deposition (PVD) has been applied to the synthesize In_2Se_3 nanowire arrays for visible-light photodetectors, which displays high photosensitivity and quick photoresponse due to the superior quality of the single-crystal In_2Se_3 and the large surface-to-volume ratio, as shown in Figure 2.27.[87] Recently, In_2Se_3 nanosheets were prepared successfully by micromechanical exfoliation.[85] Lin et al reported the few layer In_2Se_3 by epitaxial on mica and graphene.[90] This method opened a new way to synthesize the large-size In_2Se_3 monolayer. However, there are still some difficulties, e.g. transferring samples onto other substrates may be required for device fabrication. Also, the In_2Se_3 powders used as precursors will easily decompose to InSe under low pressure at high temperature. Synthesis of large monolayer In_2Se_3 is very urgent for its applications.

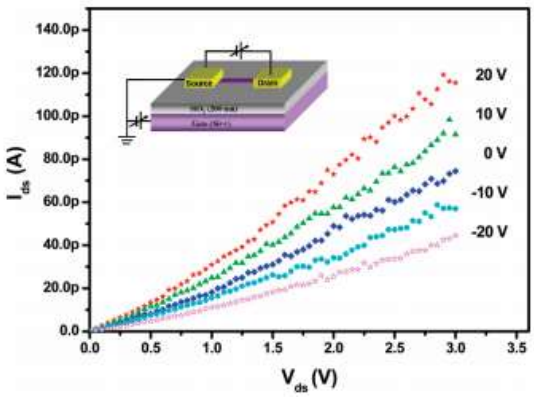

Figure 2.27 I-V characteristics of In_2Se_3 nanowire

2.2 Questions to Answer Based on Literature

As discussed in the literature review, although many efforts have been made about the synthesis, properties and application in MoS_2, $MoSe_2$, WS_2, WSe_2 and their heterostructures, there are many other 2D materials and heterostructures have not been touched. The questions are as follows:

First, MoS_2, $MoSe_2$, WS_2, and WSe_2 have been synthesized by PVD or CVD method successfully. Their applications in FETs, photodetectors and valley spintronics have been studied. People do not know if the monolayer $MoTe_2$ and WTe_2 single crystals can be synthesized. What are the properties of their monolayer? In the thesis, a CVD strategy to directly synthesize WTe_2 and $MoTe_2$ few-layer and monolayers at large scale is designed. The mixed compounds (weight ratio of the compound metal oxide WO_3 (MoO_3): metal chlorides WCl_6 ($MoCl_5$): Te is 1:1:1) and Te will be used as the source of W (Mo) and Te, respectively. Such configuration of the precursors makes the reaction between Te and the metal sources react easily. The Te in the mixed compounds can decrease the melting point of the mixed compounds, while the other Te powder is used as to keep the Te atmosphere in the whole reaction process.

Second, the MoX_2 and WX_2 (X: S, Se, Te) have the same crystal structures and in the same group-group VI TMDs. Whether other group such as group IV-, and V- based 2D TMDs can be synthesized? Do these 2D TMDs show the similar properties with their bulk? As discussed in the above literature review, the high melting point of the corresponding metal precursors impedes researchers to produce monolayer of these 2D TMDs. Over the past few decades, molten-salt assisted growth method has been successfully used to synthesize ceramic powders that were often produced at very high temperature. Similarly, in this thesis, the salt assisted growing will be designed for the growth of 2D TMDs. Molten-salt lowers the reaction activation energy by significantly reducing the melting point of the metal precursors. Promoted by salt, the metal precursors becoming volatile in a suitable temperature window, and thus make the reaction possible for the growth of the 2D TMDs.

Third, the heterostructures based on 2D TMDs (MoX_2, and WX_2 (X: S, Se, Te)) show excellent properties, which are often obtained by CVD or PVD method. One may wonder whether the vertically stacking heterostructure between MoX_2 and PtX_2 such as $MoSe_2/PtSe_2$ can be synthesized. The typical strong interlayer coupling has been observed in the vertical heterostructures such as MoS_2/WS_2, MoS_2/WSe_2 which were obtained by transferred method or CVD method. As for the group-10 TMDs, the strong interlayer coupling has been observed in $PtSe_2$ crystals. The realizable synthesis of MX_2 and strong interlayer coupling offer the opportunity to synthesis of their heterostructures. By utilizing these properties, strong coupling epitaxial growth of 2D vertical heterostructure between a typical group-10 TMD-$PtSe_2$ and $MoSe_2$ via one-step by CVD method is designed using the $PtCl_2$, MoO_3, and Se as sources.

Forth, the In_2Se_3 nanowires and nanosheets show excellent optoelectronic properties. The few layer In_2Se_3 has been obtained. Researchers maybe want to know how to synthesis the monolayer In_2Se_3 and how about the property of monolayer. In this thesis, the PVD method will be used for synthesis of monolayer In_2Se_3 at high temperature. Enhanced vapor pressure of In_2Se_3 at high temperature can promote the growth of In_2Se_3 monolayer.

2.3 PhD in Context of Literature

In this thesis, the novel 2D materials including $MoTe_2$, WTe_2, IV-, V-based 2D TMDs, the epitaxial heterstructure between $MoSe_2$ and $PtSe_2$, and monolayer α-In_2Se_3 were synthesized. The properties and applications of $MoTe_2$, WTe_2, $MoSe_2/PtSe_2$, and α-In_2Se_3 were studied. The contributions of this thesis are list as follow:

First, a CVD method was designed and successfully used to produce the large monolayer $MoTe_2$ and WTe_2. The size of as-synthesized $MoTe_2$ and WTe_2 is up to 300 μm. Their monolayer atomic structure were identified by STEM. The novel properties such as superconducting transition behavior in $MoTe_2$ and seminal-insulator transition in few layer WTe_2 were obtained.

Second, the molten salt-assisted method was designed to prepare the IV-, V-based 2D TMDs. We demonstrated that the IV-, V-based 2D TMDs were produced by the designed method. The superconductivity in monolayer $NbSe_2$ was observed for the first time using the as-prepared CVD samples.

Third, the vertically stacked heterostructure between monolayer $PtSe_2$ and $MoSe_2$ was produced by epitaxial method via one-step CVD method. The STEM confirmed their vertically stacked structure. The devices fabricated using $MoSe_2/PtSe_2$ show typical p-n junction properties.

Forth, the PVD method was used to synthesize atom-thin In_2Se_3 with different layers. AFM and STEM confirmed that the as-synthesized In_2Se_3 is monolayer. Temperature-dependent Raman spectra identified that the as-synthesized In_2Se_3 is α-In_2Se_3. The properties of FET and photodetector using few layer In_2Se_3 indicating that In_2Se_3 atomic layers is a promising candidate for the optoelectronic and photosensitive device applications.

References

[1] K. S. Novoselov, A. K. Geim, S. V. Morozov, D. Jiang, Y. Zhang, S. V. Dubonos, I. V. Grigorieva, A. A. Firsov, Science 2004, 306, 666.

[2] A. K. Geim, K. S. Novoselov, Nat Mater 2007, 6, 183.

[3] M. Chhowalla, H. S. Shin, G. Eda, L. J. Li, K. P. Loh, H. Zhang, Nat Chem 2013, 5, 263.

[4] 2016.

[5] R. Suzuki, M. Sakano, Y. J. Zhang, R. Akashi, D. Morikawa, A. Harasawa, K. Yaji, K. Kuroda, K. Miyamoto, T. Okuda, K. Ishizaka, R. Arita, Y. Iwasa, Nat Nanotechnol 2014, 9, 611.

[6] A. V. Kolobov, J. Tominaga, *Two-Dimensional Transition-Metal Dichalcogenides*, Vol. 239, Springer International Publishing, Switzerland 2016.

[7] G. R. Bhimanapati, Z. Lin, V. Meunier, Y. Jung, J. Cha, S. Das, D. Xiao, Y. Son, M. S. Strano, V. R. Cooper, L. B. Liang, S. G. Louie, E. Ringe, W. Zhou, S. S. Kim, R. R. Naik, B. G. Sumpter, H. Terrones, F. N. Xia, Y. L. Wang, J. Zhu, D. Akinwande, N. Alem, J. A. Schuller, R. E. Schaak, M. Terrones, J. A. Robinson, Acs Nano 2015, 9, 11509.

[8] K. J. Koski, Y. Cui, Acs Nano 2013, 7, 3739.

[9] K. F. Mak, C. Lee, J. Hone, J. Shan, T. F. Heinz, Phys Rev Lett 2010, 105.

[10] M. N. Ali, J. Xiong, S. Flynn, J. Tao, Q. D. Gibson, L. M. Schoop, T. Liang, N. Haldolaarachchige, M. Hirschberger, N. P. Ong, R. J. Cava, Nature 2014, 514, 205.

[11] Y. C. Lin, D. O. Dumcenco, Y. S. Huang, K. Suenaga, Nat. Nanotechnol. 2014, 9, 391.

[12] X. Xi, Z. Wang, W. Zhao, J.-H. Park, K. T. Law, H. Berger, L. Forró, J. Shan, K. F. Mak, Nat. Phys. 2015, 12, 139.

[13] B. Sipos, A. F. Kusmartseva, A. Akrap, H. Berger, L. Forro, E. Tutis, Nat. Mater. 2008, 7, 960.

[14] K. F. Mak, C. Lee, J. Hone, J. Shan, T. F. Heinz, Phys. Rev. Lett. 2010, 105.

[15] A. Ramasubramaniam, Phys. Rev. B 2012, 86.

[16] W. Bao, X. Cai, D. Kim, K. Sridhara, M. S. Fuhrer, Appl. Phys. Lett. 2013, 102, 042104.

[17] Q. H. Wang, K. Kalantar-Zadeh, A. Kis, J. N. Coleman, M. S. Strano, Nat. Nanotechnol. 2012, 7, 699.

[18] D. Xiao, G. Liu, W. Feng, X. Xu, W. Yao, Phys. Rev. Lett. 2012, 108.

[19] H. Zeng, J. Dai, W. Yao, D. Xiao, X. Cui, Nat. Nanotechnol. 2012, 7, 490.

[20] K. F. Mak, K. He, J. Shan, T. F. Heinz, Nat. Nanotechnol. 2012, 7, 494.

[21] T. Cao, G. Wang, W. Han, H. Ye, C. Zhu, J. Shi, Q. Niu, P. Tan, E. Wang, B. Liu, J. Feng, Nat. Commun. 2012, 3, 887.

[22] M. Chhowalla, H. S. Shin, G. Eda, L. J. Li, K. P. Loh, H. Zhang, Nat. Chem. 2013, 5, 263.

[23] M. Pumera, A. H. Loo, Trends Anal. Chem. 2014, 61, 49.

[24] D. C. Elias, R. R. Nair, T. M. G. Mohiuddin, S. V. Morozov, P. Blake, M. P. Halsall, A. C. Ferrari, D. W. Boukhvalov, M. I. Katsnelson, A. K. Geim, K. S. Novoselov, Science 2009, 323, 610.

[25] Z. Y. Zeng, Z. Y. Yin, X. Huang, H. Li, Q. Y. He, G. Lu, F. Boey, H. Zhang, Angew Chem Int Edit 2011, 50, 11093.

[26] J. N. Coleman, M. Lotya, A. O'Neill, S. D. Bergin, P. J. King, U. Khan, K. Young, A. Gaucher, S. De, R. J. Smith, I. V. Shvets, S. K. Arora, G. Stanton, H. Y. Kim, K. Lee, G. T. Kim, G. S. Duesberg, T. Hallam, J. J. Boland, J. J. Wang, J. F. Donegan, J. C. Grunlan, G. Moriarty, A. Shmeliov, R. J. Nicholls, J. M. Perkins, E. M. Grieveson, K. Theuwissen, D. W. McComb, P. D. Nellist, V. Nicolosi, Science 2011, 331, 568.

[27] Y. H. Lee, X. Q. Zhang, W. J. Zhang, M. T. Chang, C. T. Lin, K. D. Chang, Y. C. Yu, J. T. W. Wang, C. S. Chang, L. J. Li, T. W. Lin, Adv Mater 2012, 24, 2320.

[28] Q. Q. Ji, Y. Zhang, Y. F. Zhang, Z. F. Liu, Chem Soc Rev 2015, 44, 2587.

[29] Y. J. Zhan, Z. Liu, S. Najmaei, P. M. Ajayan, J. Lou, Small 2012, 8, 966.

[30] K. K. Liu, W. J. Zhang, Y. H. Lee, Y. C. Lin, M. T. Chang, C. Su, C. S. Chang, H. Li, Y. M. Shi, H. Zhang, C. S. Lai, L. J. Li, Nano Lett 2012, 12, 1538.

[31] J. C. Park, S. J. Yun, H. Kim, J. H. Park, S. H. Chae, S. J. An, J. G. Kim, S. M. Kim, K. K. Kim, Y. H. Lee, Acs Nano 2015, 9, 6548.

[32] N. Peimyoo, J. Z. Shang, C. X. Cong, X. N. Shen, X. Y. Wu, E. K. L. Yeow, T. Yu, Acs Nano 2013, 7, 10985.

[33] J. K. Huang, J. Pu, C. L. Hsu, M. H. Chiu, Z. Y. Juang, Y. H. Chang, W. H. Chang, Y. Iwasa, T. Takenobu, L. J. Li, Acs Nano 2014, 8, 923.

[34] A. A. Soluyanov, D. Gresch, Z. J. Wang, Q. S. Wu, M. Troyer, X. Dai, B. A. Bernevig, Nature 2015, 527, 495.

[35] Y. Sun, S. C. Wu, M. N. Ali, C. Felser, B. H. Yan, Phys Rev B 2015, 92.

[36] M. N. Ali, J. Xiong, S. Flynn, J. Tao, Q. D. Gibson, L. M. Schoop, T. Liang, N. Haldolaarachchige, M. Hirschberger, N. P. Ong, R. J. Cava, Nature 2014, 514, 205.

[37] S. Cho, S. Kim, J. H. Kim, J. Zhao, J. Seok, D. H. Keum, J. Baik, D. H. Choe, K. J. Chang, K. Suenaga, S. W. Kim, Y. H. Lee, H. Yang, Science 2015, 349, 625.

[38] M. A. Cazalilla, H. Ochoa, F. Guinea, Phys Rev Lett 2014, 113.

[39] D. H. Keum, S. Cho, J. H. Kim, D. H. Choe, H. J. Sung, M. Kan, H. Kang, J. Y. Hwang, S. W. Kim, H. Yang, K. J. Chang, Y. H. Lee, Nat Phys 2015, 11, 482.

[40] C. H. Naylor, W. M. Parkin, J. L. Ping, Z. L. Gao, Y. R. Zhou, Y. Kim, F. Streller, R. W. Carpick, A. M. Rappe, M. Drndic, J. M. Kikkawa, A. T. C. Johnson, Nano Lett 2016, 16, 4297.

[41] J. E. Callanan, G. A. Hope, R. D. Weir, E. F. Westrum, J Chem Thermodyn 1992, 24, 627.

[42] M. M. Biener, J. Biener, C. M. Friend, J Chem Phys 2005, 122.

[43] C. W. Lin, X. J. Zhu, J. Feng, C. Z. Wu, S. L. Hu, J. Peng, Y. Q. Guo, L. L. Peng, J. Y. Zhao, J. L. Huang, J. L. Yang, Y. Xie, J Am Chem Soc 2013, 135, 5144.

[44] Z. Y. Zeng, C. L. Tan, X. Huang, S. Y. Bao, H. Zhang, Energ Environ Sci 2014, 7, 797.

[45] C. L. Wan, X. K. Gu, F. Dang, T. Itoh, Y. F. Wang, H. Sasaki, M. Kondo, K. Koga, K. Yabuki, G. J. Snyder, R. G. Yang, K. Koumoto, Nat Mater 2015, 14, 622.

[46] J. Chen, S. L. Li, Z. L. Tao, F. Gao, Chem Commun 2003, 980.

[47] Y. Zhang, Z. K. Li, H. B. Jia, X. H. Luo, J. Xu, X. H. Zhang, D. P. Yu, J Cryst Growth 2006, 293, 124.

[48] E. Morosan, H. W. Zandbergen, B. S. Dennis, J. W. G. Bos, Y. Onose, T. Klimczuk, A. P. Ramirez, N. P. Ong, R. J. Cava, Nat Phys 2006, 2, 544.

[49] Y. I. Joe, X. M. Chen, P. Ghaemi, K. D. Finkelstein, G. A. de la Pena, Y. Gan, J. C. T. Lee, S. Yuan, J. Geck, G. J. MacDougall, T. C. Chiang, S. L. Cooper, E. Fradkin, P. Abbamonte, Nat Phys 2014, 10, 421.

[50] D. L. Duong, G. Ryu, A. Hoyer, C. T. Lin, M. Burghard, K. Kern, Acs Nano 2017, 11, 1034.

[51] J. Y. Wang, H. S. Zheng, G. C. Xu, L. F. Sun, D. K. Hu, Z. X. Lu, L. N. Liu, J. Y. Zheng, C. G. Tao, L. Y. Jiao, J Am Chem Soc 2016, 138, 16216.

[52] Y. Koike, M. Okamura, T. Nakanomyo, T. Fukase, J Phys Soc Jpn 1983, 52, 597.

[53] Y. D. Ma, Y. Dai, M. Guo, C. W. Niu, Y. T. Zhu, B. B. Huang, Acs Nano 2012, 6, 1695.

[54] K. Xu, P. Z. Chen, X. L. Li, C. Z. Wu, Y. Q. Guo, J. Y. Zhao, X. J. Wu, Y. Xie, Angew Chem Int Edit 2013, 52, 10477.

[55] W. J. Hardy, J. T. Yuan, H. Guo, P. P. Zhou, J. Lou, D. Natelson, Acs Nano 2016, 10, 5941.

[56] J. T. Yuan, J. J. Wu, W. J. Hardy, P. Loya, M. Lou, Y. C. Yang, S. Najmaei, M. L. Jiang, F. Qin, K. Keyshar, H. Ji, W. L. Gao, J. M. Bao, J. Kono, D. Natelson, P. M. Ajayan, J. Lou, Adv Mater 2015, 27, 5605.

[57] X. X. Xi, L. Zhao, Z. F. Wang, H. Berger, L. Forro, J. Shan, K. F. Mak, Nat Nanotechnol 2015, 10, 765.

[58] W. Y. Ge, K. Kawahara, M. Tsuji, H. Ago, Nanoscale 2013, 5, 5773.

[59] S. H. Zhao, T. Hotta, T. Koretsune, K. Watanabe, T. Taniguchi, K. Sugawara, T. Takahashi, H. Shinohara, R. Kitaura, 2d Mater 2016, 3.

[60] G. Fiori, F. Bonaccorso, G. Iannaccone, T. Palacios, D. Neumaier, A. Seabaugh, S. K. Banerjee, L. Colombo, Nat Nanotechnol 2014, 9, 768.

[61] K. F. Mak, J. Shan, Nat Photonics 2016, 10, 216.

[62] B. Radisavljevic, A. Kis, Nat Mater 2013, 12, 815.

[63] F. K. Perkins, A. L. Friedman, E. Cobas, P. M. Campbell, G. G. Jernigan, B. T. Jonker, Nano Lett 2013, 13, 668.

[64] Z. Y. Yin, H. Li, H. Li, L. Jiang, Y. M. Shi, Y. H. Sun, G. Lu, Q. Zhang, X. D. Chen, H. Zhang, Acs Nano 2012, 6, 74.

[65] J. S. Ross, P. Klement, A. M. Jones, N. J. Ghimire, J. Q. Yan, D. G. Mandrus, T. Taniguchi, K. Watanabe, K. Kitamura, W. Yao, D. H. Cobden, X. D. Xu, Nat Nanotechnol 2014, 9, 268.

[66] D. Xiao, G. B. Liu, W. X. Feng, X. D. Xu, W. Yao, Phys Rev Lett 2012, 108.

[67] K. S. Novoselov, A. Mishchenko, A. Carvalho, A. H. C. Neto, Science 2016, 353.

[68] M. Y. Li, Y. M. Shi, C. C. Cheng, L. S. Lu, Y. C. Lin, H. L. Tang, M. L. Tsai, C. W. Chu, K. H. Wei, J. H. He, W. H. Chang, K. Suenaga, L. J. Li, Science 2015, 349, 524.

[69] K. Chen, X. Wan, J. X. Wen, W. G. Xie, Z. W. Kang, X. L. Zeng, H. J. Chen, J. B. Xu, Acs Nano 2015, 9, 9868.

[70] K. Chen, X. Wan, W. G. Xie, J. X. Wen, Z. W. Kang, X. L. Zeng, H. J. Chen, J. B. Xu, Adv Mater 2015, 27, 6431.

[71] X. F. Li, M. W. Lin, J. H. Lin, B. Huang, A. A. Puretzky, C. Ma, K. Wang, W. Zhou, S. T. Pantelides, M. F. Chi, I. Kravchenko, J. Fowlkes, C. M. Rouleau, D. B. Geohegan, K. Xiao, Sci Adv 2016, 2.

[72] Y. D. Yoo, Z. P. Degregorio, J. E. Johns, J Am Chem Soc 2015, 137, 14281.

[73] T. Zhang, B. Jiang, Z. Xu, R. G. Mendes, Y. Xiao, L. F. Chen, L. W. Fang, T. Gemming, S. L. Chen, M. H. Rummeli, L. Fu, Nat Commun 2016, 7.

[74] Y. J. Gong, J. H. Lin, X. L. Wang, G. Shi, S. D. Lei, Z. Lin, X. L. Zou, G. L. Ye, R. Vajtai, B. I. Yakobson, H. Terrones, M. Terrones, B. K. Tay, J. Lou, S. T. Pantelides, Z. Liu, W. Zhou, P. M. Ajayan, Nat Mater 2014, 13, 1135.

[75] X. D. Duan, C. Wang, J. C. Shaw, R. Cheng, Y. Chen, H. L. Li, X. P. Wu, Y. Tang, Q. L. Zhang, A. L. Pan, J. H. Jiang, R. Q. Yu, Y. Huang, X. F. Duan, Nat Nanotechnol 2014, 9, 1024.

[76] C. M. Huang, S. F. Wu, A. M. Sanchez, J. J. P. Peters, R. Beanland, J. S. Ross, P. Rivera, W. Yao, D. H. Cobden, X. D. Xu, Nat Mater 2014, 13, 1096.

[77] P. F. Li, L. Li, X. C. Zeng, J Mater Chem C 2016, 4, 3106.

[78] X. Y. Chia, A. Adriano, P. Lazar, Z. Sofer, J. Luxa, M. Pumera, Adv Funct Mater 2016, 26, 4306.

[79] Y. D. Zhao, J. S. Qiao, Z. H. Yu, P. Yu, K. Xu, S. P. Lau, W. Zhou, Z. Liu, X. R. Wang, W. Ji, Y. Chai, Adv Mater 2017, 29.

[80] S. H. Kwon, B. T. Ahn, S. K. Kim, F. Adurodija, K. H. Kang, K. H. Yoon, J. S. Song, J Korean Phys Soc 1997, 31, 796.

[81] P. A. Hu, L. F. Wang, M. Yoon, J. Zhang, W. Feng, X. N. Wang, Z. Z. Wen, J. C. Idrobo, Y. Miyamoto, D. B. Geohegan, K. Xiao, Nano Lett 2013, 13, 1649.

[82] C. Schumacher, K. G. Reinsberg, R. Rostek, L. Akinsinde, S. Baessler, S. Zastrow, G. Rampelberg, P. Woias, C. Detavernier, J. A. C. Broekaert, J. Bachmann, K. Nielsch, Adv Energy Mater 2013, 3, 95.

[83] L. Goncalves, C. Couto, P. Alpuim, D. M. Rowe, J. H. Correia, Mater Sci Forum 2006, 514-516, 156.

[84] J. P. Ye, S. Soeda, Y. Nakamura, O. Nittono, Jpn J Appl Phys 1 1998, 37, 4264.

[85] X. Tao, Y. Gu, Nano Lett 2013, 13, 3501.

[86] S. T. Lakshmikumar, A. C. Rastogi, Sol Energ Mat Sol C 1994, 32, 7.

[87] T. Y. Zhai, X. S. Fang, M. Y. Liao, X. J. Xu, L. Li, B. D. Liu, Y. Koide, Y. Ma, J. N. Yao, Y. Bando, D. Golberg, Acs Nano 2010, 4, 1596.

[88] K. J. Lai, H. L. Peng, W. Kundhikanjana, D. T. Schoen, C. Xie, S. Meister, Y. Cui, M. A. Kelly, Z. X. Shen, Nano Lett 2009, 9, 1265.

[89] B. Yu, S. Y. Ju, X. H. Sun, G. Ng, T. D. Nguyen, M. Meyyappan, D. B. Janes, Appl Phys Lett 2007, 91.

[90] M. Lin, D. Wu, Y. Zhou, W. Huang, W. Jiang, W. S. Zheng, S. L. Zhao, C. H. Jin, Y. F. Guo, H. L. Peng, Z. F. Liu, J Am Chem Soc 2013, 135, 13274.

Chapter 3

Experimental Methodology

In this chapter, the rationale for the synthetic methods of 2D materials, the process and the techniques used for characterization are summarized. First, the rationale for the chemical and physic vapor deposition method used for synthesis of $MoTe_2$, WTe_2, TiX_2, VX_2, NbX_2, $PtSe_2/MoSe_2$ heterostructure and In_2Se_3 are discussed. Second, the chemical reagents and experiment procedures for synthesis of these 2D materials are presented. The techniques and equipment that are used for characterization of as-produced samples are also described. Third, the details on the device fabrications and performance measurements of as-prepared samples are summarized.

3.1 Rationale for Selection

In the first part of this thesis, the $MoTe_2$ and WTe_2 were selected to be studied. As introduced in the literature review part, the synthesis of large monolayer MoS_2, WS_2, $MoSe_2$ and WSe_2 has been realized by CVD or PVD method. Their applications in FETs have been exploited. From the materials point of view, the chemical compositions of $MoTe_2$ and WTe_2 contain the chalcogen - Te, which is in the same group as the S and Se. From the synthetic method point of view, preparation of $MoTe_2$ polycrystalline film has been realized by tellurization of the pre-deposited Mo film, indicating that the Mo source can react with Te under high temperature. However, the normal CVD method cannot be used to obtain the $MoTe_2$ single crystal, especially for $MoTe_2$ monolayer. The Te powder with a low melting point about 450 ºC has been used to produce the MoS_2/WS_2 heterostructure, while no $MoTe_2$ and WTe_2 samples were found due to the low chemical reactivity between Te and MoO_3 or WO_3. Compared with MoO_3 or WO_3, the source of $MoCl_5$ or WCl_6 has low melting point and high pressure, indicating that they can be evaporated easily at high temperature. However, it is not good for the growth of $MoTe_2$ and WTe_2. Designing a new method is requested for preparation of $MoTe_2$ and WTe_2. From the property point of view, monolayer $MoTe_2$ and WTe_2 have been predicted as potential candidates for topological devices and also promising candidates of type-II Weyl materials, synthesis of $MoTe_2$ and WTe_2 single crystals are urgently for researchers to study their excellent properties.

In the second part of this thesis, the new 2D TMDs in group IV including TiS_2, $TiSe_2$ and $TiTe_2$, group V including VS_2, VSe_2, VTe_2, NbS_2, $NbSe_2$ and $NbTe_2$ were selected as the studied targets. The molten salt-assisted CVD method was performed to prepare these 2D TMDs. As discussed in the literature review, the exited properties such as CDW behavior, superconducting transition, and magnetism are predicted in these 2D materials. However, so far, few papers reported about synthesis and properties of the few layer or monolayer of these 2D TMDs because there was not a suitable method to prepare their monolayer or few layer. The reason is because the melting point of the corresponding metal oxide is very high, as shown in table 3.1. Therefore, the few or mono-layer group IV or group V 2D

TMDs using the metal oxides as the precursors cannot be produced. Although the Te powder has been used to decrease the melting point of W, the low melting point of 450 ºC makes it evaporate readily so that the Te cannot be controlled for the TMDs' growth. The molten salt-assisted method has been used to produce the ceramic powders by reducing the precursor's melting point. In this thesis, the salt such as NaCl and KI were used to reduce the melting point of TiO_2, Nb_2O_5 and V_2O_5.

Table 3.1 The melting point of metal oxides

Precursors	**TiO_2**	**Nb_2O_5**
Melting point(℃)	1850	1485

In the third part of this thesis, the heterostructure between $PtSe_2$ and $MoSe_2$ was selected as the research target. The heterostructures including in-plane and vertical have been realized in MX_2 (X: S, Se) and WS_2/ReS_2. These 2D TMDs have the similar crystal structure and lattice constant. More importantly, all these 2D materials can be synthesized by a separated CVD method. Synthesizing the heterostructure with different crystal structures and lattice constants is very difficult. As for the group-10 TMDs, the strong interlayer coupling has been observed in the PtS_2 and $PtSe_2$ crystals, maybe which offers the possibility to form epitaxial behavior with MX_2. In this thesis, the CVD method was used to produce the heterostructure.

In the last part of this thesis, the In_2Se_3 was selected as the research target. From the material point of view, In_2Se_3 has five phases. The α and ϒ phases are layered materials. The different phases offer the possibility to study its phase transition. From the synthetic method point of view, few layers In_2Se_3 has been produced by PVD method under low pressure using mica as the substrate, indicating the possibility of synthesizing monolayer In_2Se_3 by PVD method. Meanwhile, the nanowires and nanosheets of In_2Se_3 have shown excellent optoelectronic properties. Synthesis of large monolayer In_2Se_3 is very important for studying their structure and novel properties.

3.2 Synthesis

3.2.1 Chemicals

MoO_3 powder (99.9%), WO_3 powder (99.9%), Te powder (99%), S powder (99.9%), Se powder (99.9%), TiO_2 powder (99.9%), V_2O_5 powder (99.9%), Nb_2O_5 powder (99%), NaCl particle (99.9%), KI particle (99.9%), and In_2Se_3 powder (99%). All these chemicals were purchased from Sigma-aldrich (Singapore).

3.2.2 Synthesis of $MoTe_2$ and WTe_2

CVD method: The CVD method is a chemical process, which is often used to synthesize high performance, high quality semiconductor films. In a typical CVD process, the silicon wafer will be used as the substrate. The precursors will be used and react on the substrate or react before reaching the substrate and then the products will deposit on the substrate. The Ar or the mix Ar and H_2 will be used as the carrier gas. In the experiment, the CVD method is used to prepare the 2D TMDs and heterostructure.

Synthesis of $MoTe_2$ and WTe_2: The WTe_2 ($MoTe_2$) crystals were synthesized by CVD method using WO_3 (MoO_3) and WCl_6 ($MoCl_5$) (Sigma) as the W (Mo) sources. The Te powder was used as the Te sources. The crystals were synthesized in a quartz tube (1 inch diameter) with temperature from 700 ºC to 850 ºC. The system of the reaction is shown in Figure 3.1. Specifically, for the WTe_2, the mixed gas of H_2/Ar with 15 sccm and 150 sccm flow rate were used as the carrier gas, the silicon boat contained 30 mg mixed powders with WO_3: WCl_6: Te=1:1:1(weight ratio) was put in the center of the tube. The SiO_2/Si substrate was placed on the silicon boat with surface down. Another silicon boat containing 0.5 g Te powder was put on the upstream. The temperature ramped up to the 820 ºC in 17 min, and keeping at the reaction temperature for about 5 min to 15 min. Then the furnace cooled down to room temperature gradually. For the $MoTe_2$, the mixed gas of H_2/Ar with 15 sccm and 200 sccm were used as the carrier gas, the silicon boat contained 30mg mixed powder with MoO_3: $MoCl_5$: Te=1:1:1 was put in the center of the tube. The SiO_2/Si

substrate was placed on the silicon boat with surface down. Another silicon boat that contained 0.5 g Te powders was put on the upstream. The temperature ramped up to the 780 ºC in 16 min, and keeping at the reaction temperature for about 5 min to 15 min. Then the furnace cooled down to room temperature gradually.

3.2.3 Synthesis of TiX_2, VX_2 and NbX_2

The 2D materials were synthesized in a quartz tube with 1 inch in diameter. The length of the furnace is about 36 cm. The system of the reaction is shown in Figure 3.1. Mixed gas of H_2/Ar was used as the carrier gas. Specifically, the alumina boat with the volume about 8cm × 1.1 cm × 1.2 cm containing precursor powder was put in the center of the tube. The precursor powder and the salt were mixed together first. The Si substrate with 285 nm SiO_2 top layer was placed on the alumina boat with surface down, the distance between the sources and substrate is about 1 cm. Another alumina boat containing S or Se or Te powder was put on the upstream of tube furnace with temperature of about 200 ^oC, 300 ^oC, and 450 ^oC, respectively. The distance between the S or Se or Te boat and the precursor's boat is about 18 cm, 16 cm, and 15 cm, respectively. The heating rate of all reactions was 50 ^oC/min. All the reactions were carried out at atmospheric pressure. The temperature cooled down to room temperature naturally. All reaction materials were bought from Alfa Aesar with purity more than 99%. The CVD setup for the growth of 2D TMD monolayers is shown in Figure 3.1.

Synthesis of TiX_2: the mixed powder of NaCl and TiO_2 with weight of 3 mg and 20 mg in the alumina boat was placed in the center of the tube. Another alumina boat containing S powder was placed in the upstream. The Silicon wafer with 285 nm top layer was put on the alumina boat with front surface down. The furnace was heated with a ramp rate of 50 ^oC/min to the growth temperatures (750 to 810 ^oC) and held at this temperature for 8-15 mins before cooled down to room temperature naturally. The Ar/H_2 with flow 80/20 sccm was used as the carrier gas.

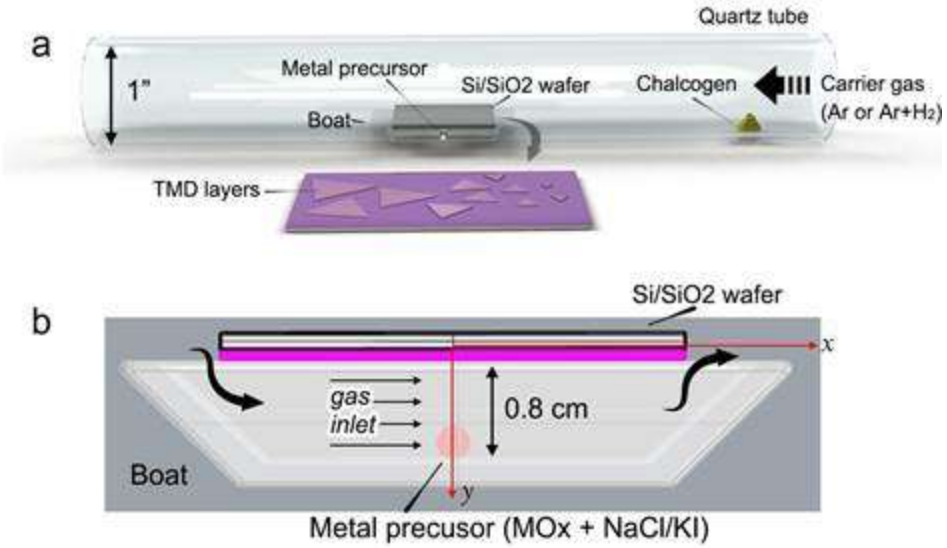

Figure 3.1 CVD setup and geometries for the growth of TMD layers.

Synthesis of VX_2: the mixed powder of KI and V_2O_5 with weight of 1 mg and 3 mg in the alumina boat was placed in the center of the tube. Another alumina boat contains S/Se/Te powder was placed in the upstream. The Silicon wafer with 285 nm top layer was put on the alumina boat with front surface down. The furnace was heated with a ramp rate of 50 ^oC/min to the growth temperatures (680 to 750 ^oC) and held at this temperature for 10-15 mins before cooled down to room temperature naturally. The Ar/H_2 with a flow rate of 80/16 sccm was used as the carrier gas.

Synthesis of NbX_2: the mixed powder of NaCl and Nb_2O_5 with weight of 2 mg and 10 mg in the alumina boat was placed in the center of the tube. Another alumina boat containing S/Se/Te powder was placed in the upstream. The Silicon wafer with 285 nm top layer was put on the alumina boat with front surface down. The furnace was heated with a ramp rate of 50 ^oC/min to the growth temperatures (750 to 850 ^oC) and held at this temperature for 4-10 mins before cooling down to room temperature naturally. The Ar/H_2 with a flow rate of 80/16 sccm was used as carrier gas.

3.2.4 Synthesis of $PtSe_2/MoSe_2$ heterostructure

In this thesis, the strong coupling epitaxial growth of 2D vertical heterostructure between a typical group-10 TMD-$PtSe_2$ and $MoSe_2$ via one-step CVD method was realized. In the experiment, the $PtCl_2$, MoO_3 and Se were used as the sources. The $PtSe_2$ and $PtSe_2/MoSe_2$ were synthesized in a quartz tube (2 inch diameter) under different temperature from 200 ^oC to 810 ^oC. The mixed Ar/H_2 gas with a flow rate of 80/10 sccm was used as the carrier gas. The Al_2O_3 boat contained 5 mg $PtCl_2$ and 5 mg MoO_3 was put in the center of the tube. The distance between $PtCl_2$ and MoO_3 is 0.5 mm. The SiO_2/Si or sapphire substrate was placed on the boat with surface downside. Another Al_2O_3 boat containing 10 g S powder was put on the upstream. The temperature ramped up to the 810 ^oC in 16 min, and held at the reaction temperature for about 15 mins. Then the furnace was cooled down to room temperature gradually.

3.2.5 Synthesis of In_2Se_3 monolayer and few layer

PVD method: The PVD method including the vacuum deposition process and atmosphere pressure process is often used to synthesize semiconductor films, in which, the materials go from a condensed phase to a vapor phase. The vapor phase will deposit on the substrate to form the condensed phase again. The Ar or Ar/H_2 mixed gas is often used as the carrier gas. For the In_2Se_3, at least five phases have been confirmed. Existence of different phases reveals that the In_2Se_3 is different from the 2D TMDs and enhances the difficulty of synthesizing In_2Se_3. Interestingly, the bulk In_2Se_3 can be obtained easily, which can be used as the precursor for synthesis of the In_2Se_3 by PVD method. The synthetic details are as follows:

Synthesis of In_2Se_3: The silica boat containing In_2Se_3 (99.99, Alfar) powders was put in the center of the tube. A piece of Si wafer with 285 nm SiO_2 was placed in the downstream about 10-15 cm far away, served as the substrate for the sample growth. Argon flow of 60 standard cubic centimeters per second (sccm) was used as the carrier gas to provide an inert atmosphere, which also carried the vaporized In_2Se_3 gas to deposit on the surface of the

substrate. The In_2Se_3 powder was heated to 850 °C in 30 min and kept at 850 °C for 5min to 20min for the growth of In_2Se_3 atomic layers. Then the temperature of the system was cooled down to natural temperature.

3.3 Characterization

After preparation of the monolayer and few layer of the 2D TMDs, heterostructure and In_2Se_3, different techniques including the Raman spectroscopy and AFM were used to characterize their quality and thickness. The TEM and STEM were performed to characterize their atomic structure. The properties and applications of as-prepared 2D materials were exploited based on their devices such as FETs or Hall bar. However, the techniques have their own advantages and limitations. Understanding the work principle is very important for us to analyze the obtained data. In the following part, the techniques that were used to characterize the 2D materials in this thesis are introduced.

3.3.1 AFM

AFM is the atomic force microscopy that is often used to check the thickness and surface of as-prepared samples. It has three different abilities such as test image, force measurement and manipulation. AFM is also used to measure the forces between the samples and the probe. For the imaging, the reaction will occurr when the probe touches the sample surface. Subsequently, the image of the three-dimensional topography of a sample surface will be obtained. When it scans the position of the sample by raster with respect to the tip, it will record the height of the probe corresponding to a constant probe-sample interaction. The topography of surface will be displayed as a pseudocolor plot. For the manipulation, the force between sample and tip is used to change the properties of the sample in a controlled way. Simultaneous with the acquisition of topographical images, some properties of the sample are measured locally and the images which often has the similarly high resolution will be obtained.

After producing the 2D materials, the AFM was used to check the thickness and morphology of 2D materials. The monolayer thickness of 2D materials is less than 1 nm, and the thickness of bilayer is about 1.5 nm. Most of the time, the monolayer 2D TMDs are the preferred target. If the thickness of the as-synthesized 2D TMDs is less than 1 nm, it can be considered as a monolayer. Such as the thickness of MoS_2 monolayer is about 0.8 nm. For the morphology, AFM can be used to illustrate the uniform of as-prepared 2D TMDs.

In this thesis, the type of the atomic force microscopy (AFM) is Asylum Research, Cypher S. The probe type for AC mode is Arrow-NCR-50-Silicon SPM-Sensor. The force constant is 42N/m. The resonance frequency is 285kHz. The thickness is 4.6 μm, length is 160 μm, and width is 45 μm. The tip radius is 10 nm ~ 15 nm. All the AFM mages are acquired under ambient conditions. The system is shown in Figure 3.2.

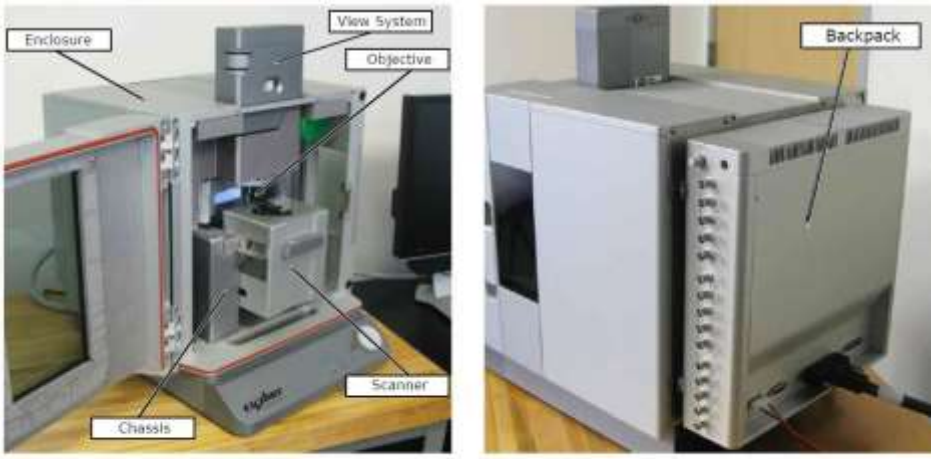

Figure 3.2 (a) Front view of AFM. (b) Rear view.

3.3.2 Raman spectroscopy

Raman spectroscopy is a spectroscopic technique that is often used to observe vibrational, rotational, and other low-frequency modes in a system. Raman spectroscopy is commonly used in chemistry to provide a fingerprint by which molecules can be identified. It relies

on inelastic scattering, or Raman scattering. The laser light interacts with phonons or other excitations in the system, resulting in the energy of the laser photons being shifted up or down. The shift in energy gives information about the vibrational modes in the system. The Raman effect is shown in Figure 3.3.

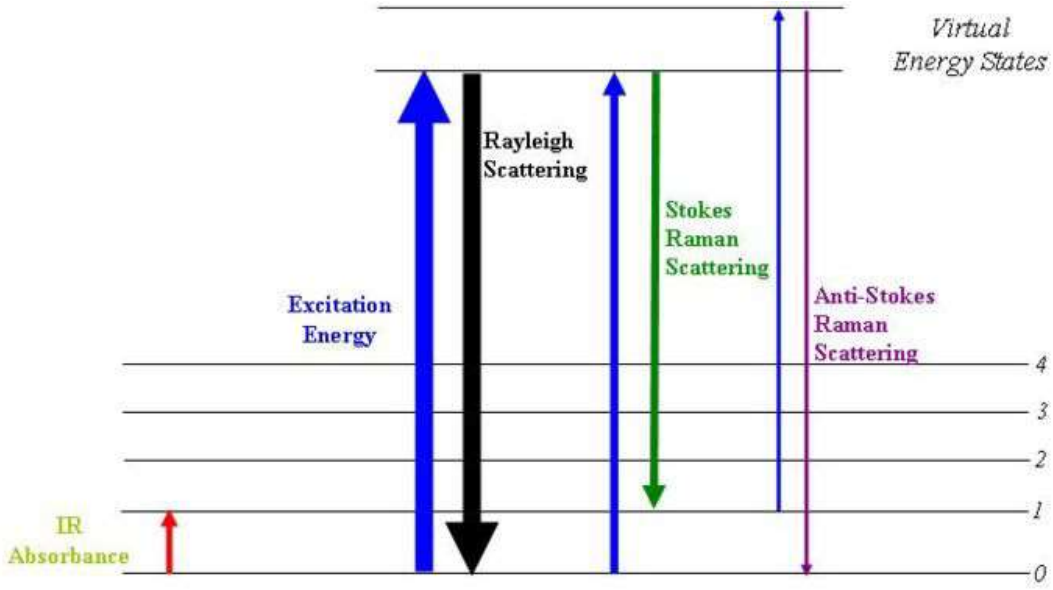

Figure 3.3 Analysis of the Raman effect.

Different 2D materials have different vibrational modes, Raman spectroscopy can be used to confirm the as-synthesized 2D materials. Such as the Ag mode ~ 401 cm^{-1} and Eg mode ~ 381 cm^{-1} resulting from the out-of-plane vibration of S atoms and in-plane vibration of Mo atoms in MoS_2.[1] Similarly, the Raman spectroscopy can be used to confirm the synthesized $MoTe_2$, WTe_2, and so on.

In the experiment, Raman measurements with an excitation laser of 532 nm was performed using a WITEC alpha 300R Confocal Raman system, as shown in Figure 3.4. Before Raman characterization, the system is calibrated with the Raman peak of Si at 520 cm^{-1}. The Raman and PL mapping are performed on a Renishaw inVia microscope with a laser of 514.5 nm. The laser powers are less than 1mW.

Figure 3.4 Raman system used in my thesis.

3.3.3 TEM and STEM

Transmission electron microscope (TEM): TEM is a microscopy technique that is often used to test the crystal structure. When electrons transmit through the thin specimen such as WTe_2, $PtSe_2$/$MoSe_2$, they will interact with the specimen when they pass through the specimen. Meanwhile, an image will be formed due to the interaction between the electrons and the specimen. Then the image can be magnified to focus on an imaging device which is often detected by a CCD camera.

A higher resolution can be obtained by TEM. This is because of the small de Broglie wavelength of electrons. TEM can help to find out the fine detail from the samples. After

synthesizing the 2D materials, the TEM will be used to confirm the atomic structure of 2D materials such as the atomic structure of $MoTe_2$, WTe_2, and In_2Se_3.

Scanning transmission electron microscope (STEM): STEM is a type of transmission electron microscopy. The image is formed when the electrons pass through the thin specimen. However, unlike TEM, in STEM the electron beam is focused to a fine spot which is then scanned over the sample in a raster. The rastering of the beam across the sample makes STEM suitable for analytical techniques such as the Z-contrast annular dark-field imaging, and spectroscopic mapping by energy dispersive X-ray (EDX) spectroscopy, or electron energy loss spectroscopy (EELS). So that these signals can be obtained at the same time, allowing direct correlation of spectroscopic data and images. A schematic diagram of a STEM instrument is shown in Figure 3.5.[2] Moreover, the equivalence between bright-field STEM and HRTEM imaging is shown in Figure 3.6.[2] By combining the TEM and STEM, the atomic structure of 2D materials can be clearly studied.

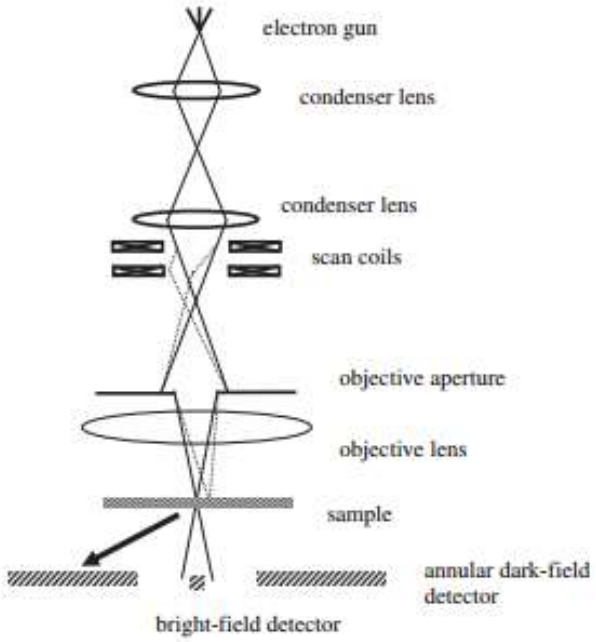

Figure 3.5 A schematic diagram of a STEM instrument.

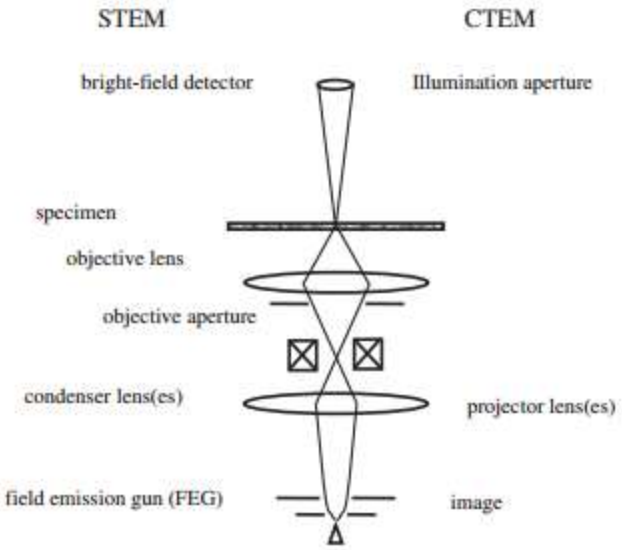

Figure 3.6 Equivalence between bright-field STEM and HRTEM imaging

3.3.4 Transferred method

The 2D materials and heterostructure were grown on the SiO_2 substrate and cannot be used for TEM measurement. In order to measure their atomic structure, the as-grown 2D layers need to be transferred onto TEM grid such as the Mo grid. The transfer methods including all-dry transfer process and wet chemical method have been used to transfer the graphene, the process as shown in Figure 3.7[3] and Figure 3.8.[4, 5] In this thesis, the PMMA assistant method was used to transfer the 2D TMDs including $MoTe_2$, WTe_2, $PtSe_2/MoS_2$ and In_2Se_3 onto the TME grid. However, other 2D TMDs including TiS_2 and $NbSe_2$ are very easily oxidized in air and can react with water that has to be used in the PMMA assistant method. In order to transfer the as-synthesized TiS_2 and $NbSe_2$, a new transfer method in this thesis was used to transfer them onto the TEM grid. The method used the poly (bisphenol A carbonate) (abbreviated as PC) coating on the 2D flakes which could be directly lifted up by adhesive PDMS sheet. The process is shown in Figure 3.9.[6]

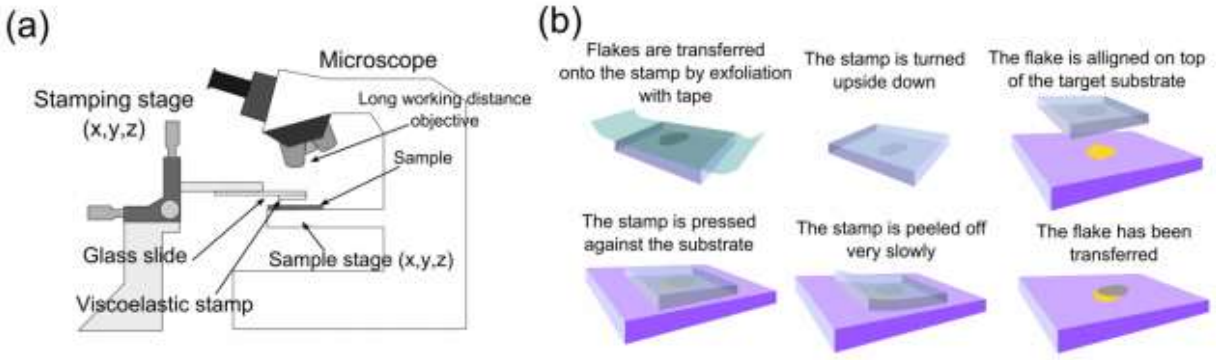

Figure 3.7 Deterministic transfer setup and process for 2D materials.

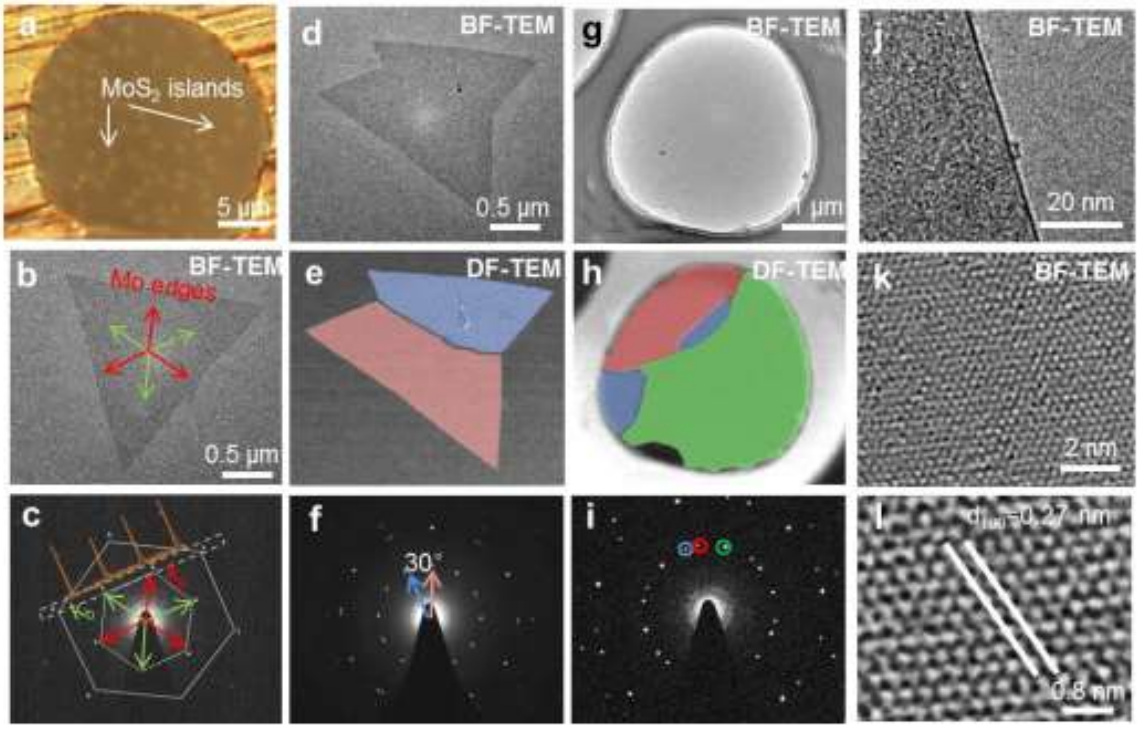

Figure 3.8 Transferability of MoS_2 onto TEM grids using wet chemical method.

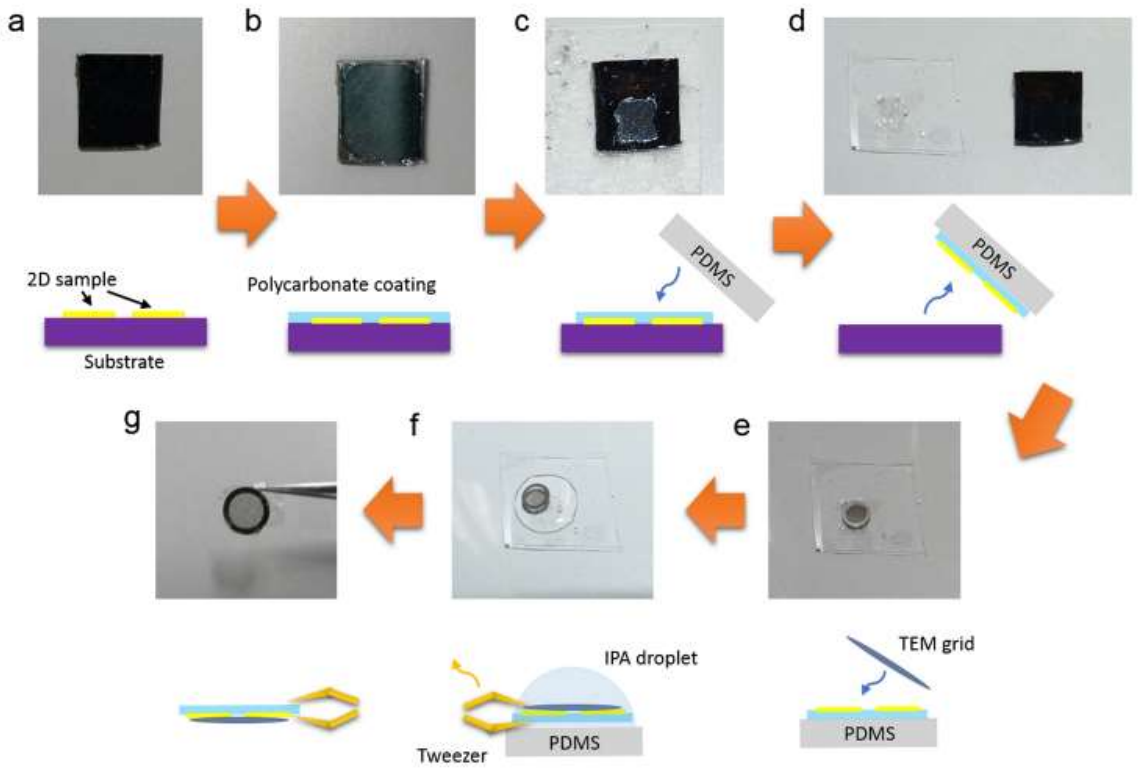

Figure 3.9 Step-by-step schematic and optical images of the transfer method.

The transferred process is as follows: The method about TEM samples was prepared using the PMMA assisted. A layer of PMMA of about 1 μm thick was spin-coated on the wafer with samples deposited, and then baked at 170 °C for 5 min. Afterwards, the wafer was immersed in KOH solution (1M) to etch the SiO_2 layer over night. After lifting off, the PMMA/samples film was transferred to DI water for several cycles to wash away the residual contaminations, and then it was fished by a TEM grid (Quantifoil Mo grid). The transferred specimen was dried naturally in ambient environment, and then dropped into the acetone overnight to wash away the PMMA coating layers. The ADF-STEM were done with a FEI Titan ChemiSTEM equipped with a so-called probe corrector. This microscope was operated with an acceleration voltage of 200 kV. The convergent angle for illumination was about 22 mrad with a probe current of < 70 pA, and the collection angle was about 43.4 to 200 mrad. The selected area diffraction patterns were recorded with a FEI Tecnai F20 operated at 200 kV.

Preparation of $MoTe_2$ and WTe_2 for STEM: The STEM samples were prepared with a poly (methyl methacrylate) (PMMA) assisted method. A layer of PMMA of about 1 μm thick was spin-coated on the wafer with WTe_2 ($MoTe_2$) samples deposited, and then baked at 180 °C for 3min. Afterwards, the wafer was immersed in NaOH solution (1M) to etch the SiO_2 layer over night. After lift-off, the PMMA/WTe_2 ($MoTe_2$) film was transferred into DI water for several cycles to wash away the residual contaminants, and then it was fished by a TEM grid. The transferred specimen was dried naturally in ambient environment, and then dropped into acetone overnight to wash away the PMMA coating layers. The STEM imaging of WTe_2 and $MoTe_2$ shown in the corresponding part was performed on an aberration-corrected Nion UltraSTEM-100 operating at 100 kV. The convergence semi-angle for the incident probe was 31 mrad. Z-contrast images were collected for a half-angle range of ~ 86-200 mrad. STEM imaging and EELS analysis on $MoTe_2$ were performed on a JEOL 2100F with a cold field-emission gun and an aberration corrector (the DELTA-corrector) operating at 60 kV. A Gatan GIF Quantum was used for recording the EELS spectra. The inner and outer collection angles for the STEM image (β1 and β2) are 62 and 129–140 mrad, respectively, with a convergence semi-angle of 35 mrad. The beam current is about 15 pA for the ADF imaging and EELS chemical analyses. All imaging was performed at room temperature.

Preparation of IV-, V-based 2D TMDs for TEM: TEM samples were prepared with a poly (methyl methacrylate) (PDMS) assisted method (or PMMA-free method with the assistance of Iso-Propyl alcohol (IPA) droplet). For some water sensitive materials such as TiS_2 and $NbSe_2$, a non-aqueous transfer method that was described elsewhere was used. STEM imaging and EELS analysis were performed on a JEOL 2100F with a cold field-emission gun and an aberration corrector (the DELTA-corrector) operating at 60 kV. A Gatan GIF Quantum was used for recording the EELS spectra. The inner and outer collection angles for the STEM image (β1 and β2) are 62 and 129–140 mrad, respectively, with a convergence semi-angle of 35 mrad. The beam current is about 15 pA for the annular dark-field (ADF) imaging and EELS chemical analysis.

Preparation of $PtSe_2$/$MoSe_2$ for STEM: The STEM samples were prepared similar to the preparation of $MoTe_2$ and WTe_2. A layer of PMMA of about 0.8 μm thick was spin-coated on the wafer with samples deposited, and then baked at 150 °C for 5 min. Afterwards, the wafer was immersed in KOH solution (2M) to etch the SiO_2 layer over night. After lift-off, the PMMA/$PtSe_2$/$MoSe_2$ film was transferred into DI water for several cycles to wash away the residual contaminants, and then it was fished by a TEM grid (Quantifoil Mo grid).

Preparation of In_2Se_3 for TEMP: The TEM samples were prepared with a poly (methyl methacrylate) (PMMA) assisted method. A layer of PMMA of about 1 μm thick was spin-coated on the water with In_2Se_3 samples deposited, and then baked at 150 °C for 1min. Afterwards, the wafer was immersed in NaOH solution (1M) to etch the SiO_2 layer over night. After lifting off, the PMMA/In_2Se_3 film was transferred to DI water for several cycles to wash away the residual contaminations, and then it was fished by a TEM grid (Quantifoil Mo grid). The transferred specimen was dried naturally in an ambient environment, and then dropped into the acetone overnight to wash away the PMMA coating layers. The ADF-STEM were done with a FEI Titan ChemiSTEM equipped with a so-called probe corrector. This microscope was operated with an acceleration voltage of 200 kV. The convergent angle for illumination is about 22 mrad with a probe current of < 70 pA, and the collection angle is about 43.4 to 200 mrad. The selected area diffraction patterns in Figure 3d were recorded with a FEI Tecnai F20 operated at 200 kV.

3.3.5 Devices and applications

After synthesizing the 2D materials, their properties such as the mobility, photoresponsibility and applications in superconducting devices and photodetectors were further exploited. First, the devices were fabricated. Subsequently, the suitable measurement station was chosen according to different properties, such as the superconductivity in $MoTe_2$ was measured with the temperature ranging from 0K to 300K.

Mechanical probe station: Probe station is often used to detect physical signals from the internal nodes of semiconductor devices. The manipulators are used to control the precise

position of thin needles on the surface of semiconductor devices. When the device is stimulated by adding electric field, the signal can be detected by the mechanical probe and then displays on the oscilloscope. Two types of the mechanical probes such as the active and passive can be used.

Devices fabrication and transport measurement of $MoTe_2$ amd WTe_2: The Hall bar was patterned on few layer $MoTe_2$ and WTe_2 using e-beam lithography. The Ti/Au (5/50 nm) electrodes were deposited using the thermal evaporator, followed by the lift off process. For the measurements of WTe_2, the transport measurement was performed in the Quantum Design PPMS system with temperature ranging from 300 K to 2 K, and magnetic field up to 14T. For the superconductivity measurements of $MoTe_2$, the transport experiment was carried out in a top-loading Helium-3 cryostat in a superconducting magnet. An ac probe current I_{ac}=10 nA at 30.9 Hz was applied from the source to the drain. Then a lock-in amplifier monitored the longitudinal R_{xx} through two additional electrical contacts. Figure 3.10 shows the system that was used to measure the superconducting behavior in $MoTe_2$ and semimetal-insulator transition in WTe_2.

Figure 3.10 3He cryostat (Oxford, HelioxTL, Top-loading, Base T=250 mK with a 17 T magnet) used for measure the superconducting in $MoTe_2$.

Devices fabrication and transport measurement of $PtSe_2/MoSe_2$: The Hall bar were patterned on few layer $PtSe_2/MoSe_2$ using e-beam lithography. The Ti/Au (5/50 nm) electrodes were deposited using the thermal evaporator, followed by the lift off process.

Device fabrication and characterization of In_2Se_3: The as-grown In_2Se_3 monolayer was patterned to a rectangle with UV-lithography and oxygen plasma, then 5/50 nm Cr/Au layers were deposited on the rectangle with E-beam vapor deposition as electrodes with UV-lithography. The channel length L_{ch} was designed to be 1.1 μm while the channel width W_{ch}=1 μm. The devices were measured with a probe station in a vacuum chamber.

The transport properties of In_2Se_3 and $PtSe_2/MoSe_2$ were measured in our own lab, the corresponding probe station is shown in Figure 3.11.

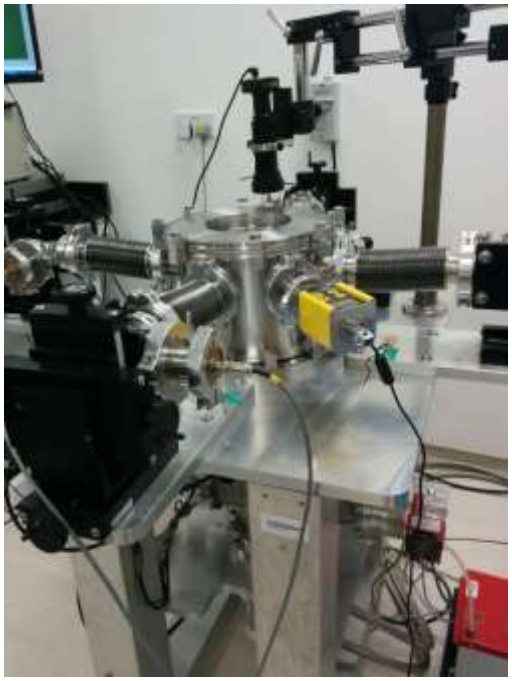

Figure 3.11 Probe station used to measure the properties of In_2Se_3 and $PtSe_2/MoSe_2$.

References

[1] H. Li, Q. Zhang, C. C. R. Yap, B. K. Tay, T. H. T. Edwin, A. Olivier, D. Baillargeat, Adv Funct Mater 2012, 22, 1385.

[2] P. D. Nellist, 2011, 91.

[3] A. Castellanos-Gomez, M. Buscema, R. Molenaar, V. Singh, L. Janssen, H. S. J. van der Zant, G. A. Steele, 2d Mater 2014, 1.

[4] Y. Yu, P. W. K. Fong, S. F. Wang, C. Surya, Sci Rep-Uk 2016, 6.

[5] H. V. Ngoc, Y. Qian, S. K. Han, D. J. Kang, Sci Rep-Uk 2016, 6.

[6] J. H. Lin, Y. C. Lin, X. S. Wang, L. M. Xie, K. Suenaga, Apl Mater 2016, 4.

Chapter 4

High-Quality 2D Transition Metal Telluride*

In this charter, the synthesis of 2D TMDs such as $MoTe_2$ and WTe_2 by chemical vapor deposition (CVD) method will be presented. The sizes of as-synthesized samples are up to 300 μm. The atomic force microscopy (AFM) was used to measure the thickness of the as-synthesized samples. Raman spectroscopy as well as scanning transmission electron microscopy (STEM) were used to characterize the quality and crystal structure of the as-synthesized samples, respectively. Devices fabricated using few layer $MoTe_2$ and WTe_2 show the enhancement of superconducting transition temperature in $MoTe_2$ and semimetal-insulator transition in WTe_2, respectively.

*This chapter published substantially as: Large-Area and High-Quality 2D Transition Metal Telluride, Zhou jiadong, etc. (Advanced Materials, 29, 1603471, 2016)

4.1 Introduction

In these years, many efforts have been devoted to synthesize monolayer TMDs, especially sulfides and selenides, by CVD and PVD methods.[1-5] Among these TMDs, the facile synthesis of monolayer MoS_2 and WS_2 has been demonstrated by different groups. Recently the wafer-size MoS_2 and WS_2 monolayers were successfully obtained by CVD and metal organic chemical vapor deposition (MOCVD) method, respectively.[6, 7] Following this strategy, the synthesis of monolayer $MoSe_2$ and WSe_2, although is a big challenge, could also be achieved by CVD or PVD method with or without the assistant of hydrogen gas.[8-12] Meanwhile, various TMD heterojunctions such as MoS_2/WS_2, MoS_2/WSe_2 and so on were also successfully prepared.[13-16] As mentioned above, most studies focused on sulfides and selenides and the synthesis of telluride atomic layers is rarely reported, mainly due to the less inactive and environmental stability of tellurium than those of sulfur and selenium. Thus, it is hard to synthesize layered tellurides, for example, $MoTe_2$ and WTe_2.

For the bulk WTe_2, which is a distorted layered transition-metal dichalcogenide with one-dimensional crystal structure and exhibits a semimetal property. The tungsten atom chains within WTe_2 layers are along a axis of orthorhombic unit cell.[17] Its thermoelectric properties have been investigated in the bulk crystal.[18] The large and non-saturating magnetoresistance has been reported by Ali *et al.* at low temperature and high magnetic field.[5] Moreover, superconductivity in few layer WTe_2 under the high pressure has also been reported by Zhongxian Zhao et al. They found that the few layer WTe_2 has a maximum superconducting critical temperature of Tc=7K at around 16.8 GPa.[19] These properties of WTe_2 show a new direction for studying the magnetoresistivity and great potential applications in the spintronics and thermoelectric devices. Compared with the WTe_2, the 1T′-$MoTe_2$ exhibits a maximum mobility and a 16,000% magnetoresistance at the low temperature (1.8 K), which offers the opportunity to fabricate topological quantum devices.[20] The difficulty in synthesizing $MoTe_2$ and WTe_2 atomic layers restricts their research progress, such as the quantum spin Hall (QSH) effect in monolayer $MoTe_2$ and WTe_2.[21]

The challenges in the synthesis of $MoTe_2$ and WTe_2 mainly lie in the following aspects: The electronegativity difference between Te and Mo(W) is only 0.3 (0.4) eV, so that the bonding energy of Mo(W)-Te bonds is quite small. Therefore stoichiometric $MoTe_2$ and WTe_2 are difficult to obtain. Moreover, at a high temperature, instead of evaporating into $MoTe_2$ and WTe_2 gas phases, WTe_2 tends to decompose to W and simultaneously lose Te vapor at around 600 ^oC.[18]

4.2 Synthesis and Discussion

4.2.1 Synthesis of $MoTe_2$ and WTe_2

Here, a CVD strategy was demonstrated to directly synthesize few-layer and monolayers WTe_2 and $MoTe_2$ at a large scale. The mixed compounds (metal oxide: metal chlorides: Te is 1:1:1 in weight ratio) and Te powder were used as the source of W (Mo) and Te, respectively. Such composition of the precursors made the reaction between Te and the metal sources carry out easily. Te in the mixed compounds could decrease the melting point of the mixed compounds, while the other Te powder in the upstream was used to keep the Te atmosphere in the whole reaction process. The reaction system is schematically shown in Figure 4.1.

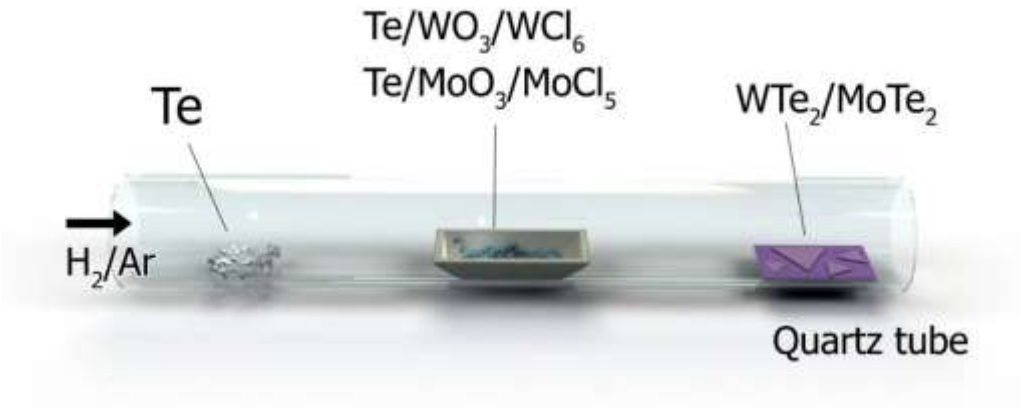

Figure 4.1 Schematic of the chemical vapor deposition setup for the controlled growth of WTe_2 and $MoTe_2$ atomic layers.

The corresponding chemical reaction are shown as follows:

$$WO_3 + WCl_6 + Te + H_2 \rightarrow WTe_2 + H_2Te\ (g) + HCl\ (g) + H_2O\ (g)$$

$$MoO_3 + MoCl_5 + Te + H_2 \rightarrow MoTe_2 + H_2Te\ (g) + HCl\ (g) + H_2O\ (g)$$

Figure 4.2a and Figure 4.2b show the side view and top view of the crystal structure of 1T′ WTe_2 and $MoTe_2$, respectively. Here, the reaction temperature for $MoTe_2$ and WTe_2 is from 700 to 850 ^oC. Different thickness of the WTe_2 and $MoTe_2$ single crystals can be obtained by controlling the growth time. For the WTe_2, monolayer WTe_2 single crystal can be obtained at 820 ^oC for 5 min with the flow amount of carrier gas about 100 sccm Ar/15 sccm H_2. A single-crystalline WTe_2 monolayer with a length about 350 μm and width about 20 μm is shown in Figure 4.2c. Optical image of a polycrystalline WTe_2 monolayer film with the domain size larger than 100 μm is shown in Figure 4.2d. Besides, bilayer WTe_2 can be obtained, as shown in Figure 4.2e. The grain boundary is highlighted by the dashed line. In order to better visibility, the enhanced contrast of the grain boundary using false color is also provided in Figure 4.2e. Similar to WTe_2, ribbon-like 1T′ $MoTe_2$ with size of 150 μm (shown in Figure 4.2f) can be obtained. Meanwhile, few layered 1T′ $MoTe_2$ with larger size up to 200 μm (Figure 4.2g) can be attained by controlling the temperature of Te source. Note that the different layer numbers appear in the same flake (Figure 4.2g) of the $MoTe_2$. The monolayer (1L), bilayer (2L) and trilayer (3L) $MoTe_2$ can be distinguished easily due to the sharp contrast. AFM was used to check the thickness of $MoTe_2$ and the corresponding AFM images of $MoTe_2$ flakes are shown in Figure 4.3.

Thick WTe_2 flakes were obtained with increasing reaction time increases. Optical images of WTe_2 with different thickness and their corresponding AFM images are provided in Figure 4.4 and Figure 4.5, respectively.

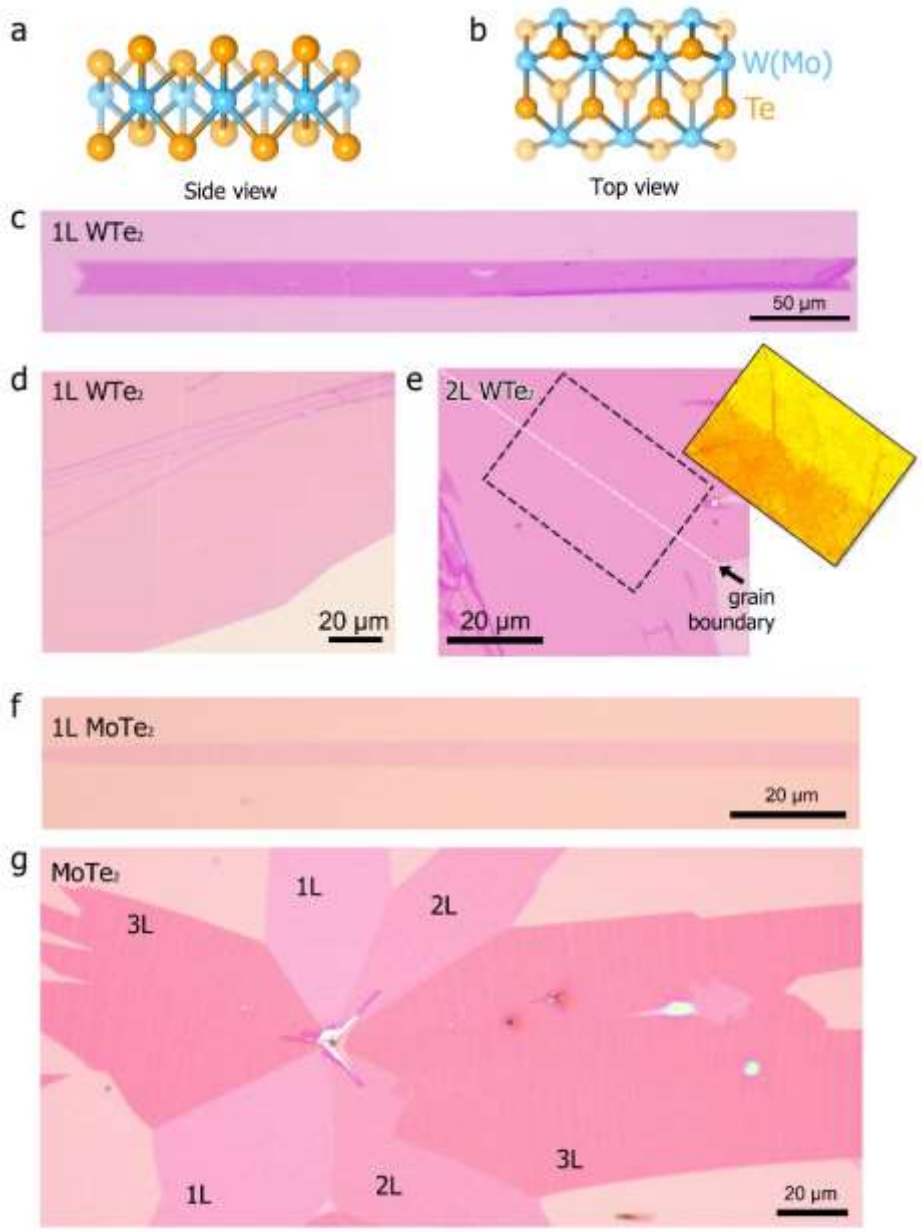

Figure 4.2 (a and b) Side and top views of the crystal structure of 1T′ W(Mo)Te_2. (c) Optical image of WTe_2 monolayer. (d**)** Optical image of a WTe_2 monolayer film**. (**e) Optical image of a large WTe_2 bilayer. (f) Optical image of a single crystalline $MoTe_2$ monolayer. (g) Optical image of a $MoTe_2$ flake.

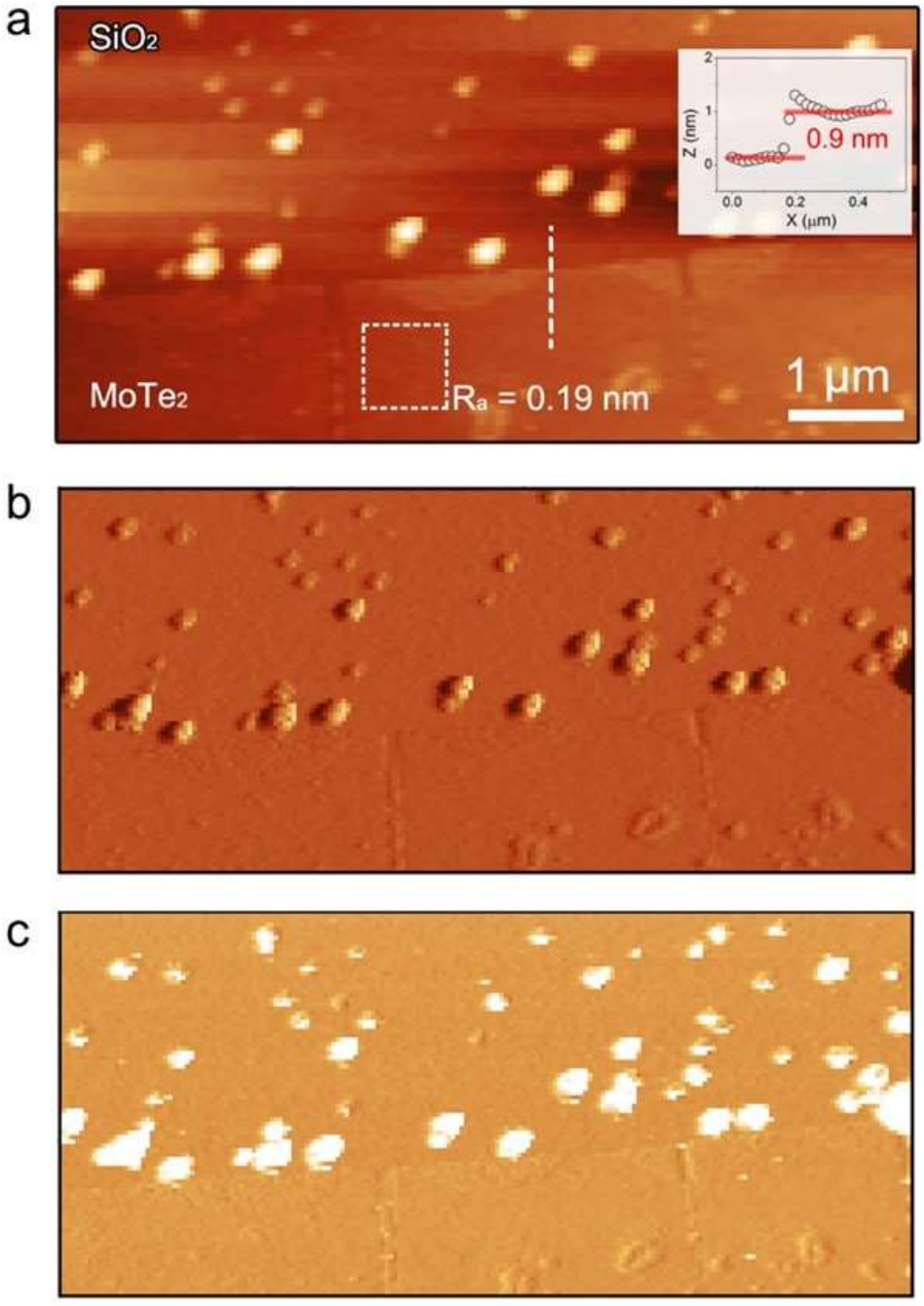

Figure 4.3 (a) AFM image of $MoTe_2$ monolayer. The thickness of 0.9 nm demonstrates the monolayer of as-produced $MoTe_2$. (b and c) The corresponding amplitude and phase image, respectively.

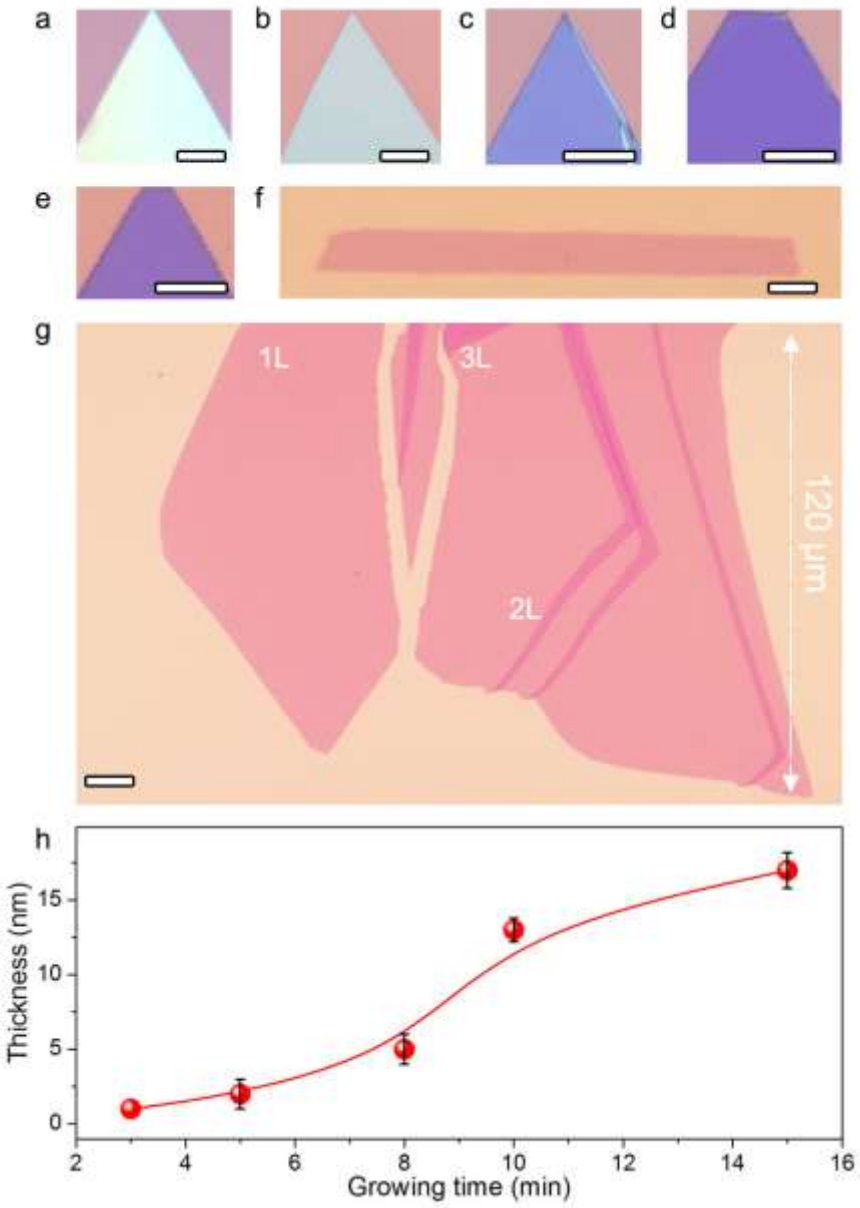

Figure 4.4 (a –f) Triangle WTe_2 single crystals with thicknesses from 25 nm to monolayer layer. 10 nm and thicker WTe_2 flakes can be obtained when the reaction time prolongs to more than 10 min. Scale bar: 10 μm. (g) Large monolayer WTe_2 with size up to 120 μm. Scale bar: 20 μm. A few regions are bi-layer and tri-layer WTe_2 (dark purple) as labeled. Such few-layer regions also facilitate forming a ribbon-like structure, complying with the 1T′ structure of WTe_2. (h) The thickness of the WTe_2 flake as a function of the growth time.

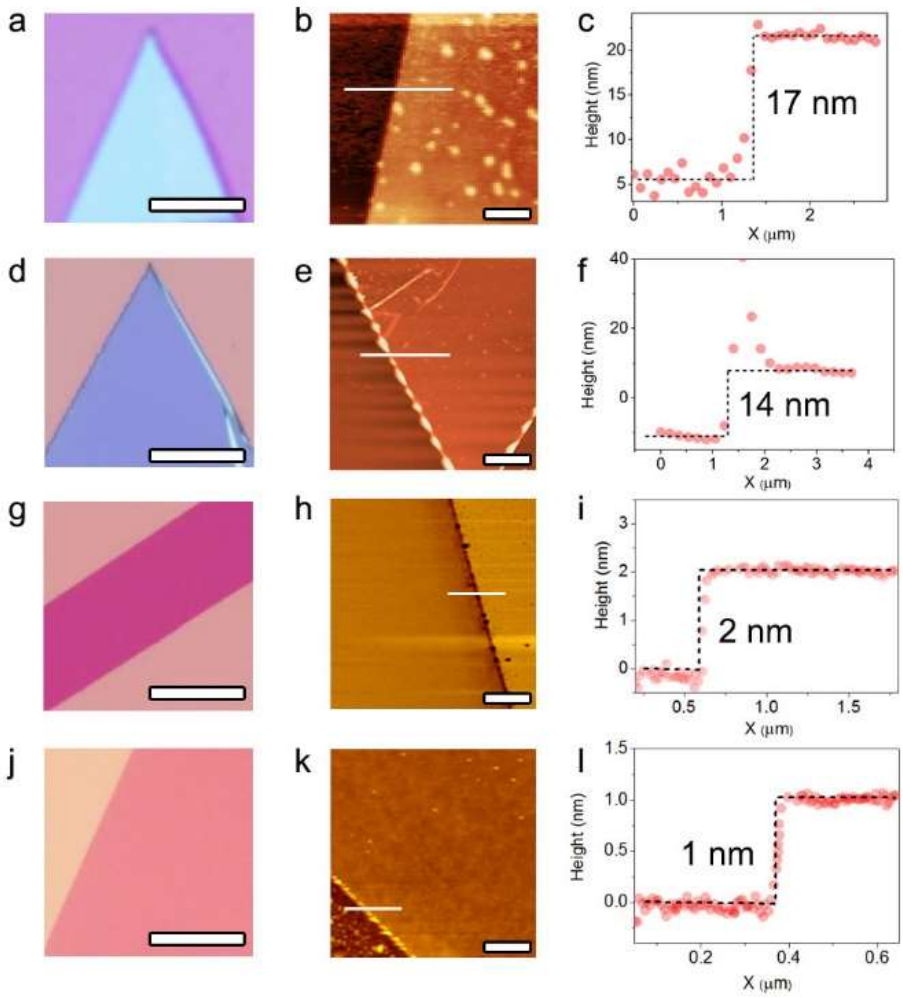

Figure 4.5 (a, d, g, j) Optical images of WTe_2 flakes captured by AFM measurement. Scale bar: 10 μm. The corresponding AFM images are shown in b, e, h and k, respectively. Scale bar: 2 μm. The corresponding thickness shown in c, f, i, and l is about 17 nm, 14 nm, 2 nm and 1 nm, respectively. Because the thickness of monolayer WTe_2 is about 0.8 nm, the WTe_2 flakes in g and j correspond to bilayer and monolayer ones, respectively.

4.2.2 Raman spectra of $MoTe_2$ and WTe_2

Raman spectroscopy was used to characterize the quality of the WTe_2 ($MoTe_2$) atomic layers. From Raman spectra of WTe_2 crystals with different thicknesses ranging from monolayer to bulk (see Figure 4.6a), only four optical vibrational modes can be obtained, ascribed to B_1^{10}, A_2^3, A_1^7 and A_1^9, respectively.[22, 23] To our knowledge, this is the first time

to detect the B_1^{10}mode in few-layer WTe_2. Moreover, with increasing layer number, the intensity of A_1^7 peak becomes stronger than other modes, which is similar to previous reports on mechanically exfoliated WTe_2 atomic layer collected along the *b* axis.[24] The optical image and Raman intensity mapping using the A_1^9 peak of WTe_2 are shown in Figure 4.6b and Figure 4.6c, respectively. The homogeneous intensity indicates a high quality of the as-synthesized WTe_2 monolayers. Figure 4.6d shows the Raman spectra contour map of monolayer and few-layer $MoTe_2$. The Raman peaks locating at 127, 161, 189 and 267 cm^{-1} are corresponding to the Raman-active A_g modes of monolayer 1T′ phase $MoTe_2$,[25] which is in good agreement with the previous reported results.[20, 26, 27] A typical optical image of 1T′ $MoTe_2$ few layer and Raman mapping of monolayer and bilayer 1T' $MoTe_2$ are shown in Figure 4.6e and Figure 4.6f, respectively. Due to their high contrast, the zone of monolayer and bilayer can be distinguished. Meanwhile, the grain boundary in WTe_2 can also be detected from Raman intensity mapping (Figure 4.7).

4.2.3 STEM characterization of WTe_2 and $MoTe_2$

Atomic resolution scanning transmission electron microscope (STEM) was applied to investigate the atomic structure of $MoTe_2$ and WTe_2 atomic layers. A high-resolution Z-contrast STEM image of monolayer WTe_2, as shown in Figure 4.8a, indicates the 1T′ phase of as-synthesized WTe_2. The highlighted dashed white rectangle shows the quasi-one-dimensional tungsten-tellurium zigzag chains along the *a* axis of the unit cell. The Fast Fourier transformation (FFT) pattern (inset of Figure 4.8a) confirms the rectangular shape of the WTe_2 unit cell. Figure 4.8b shows a line intensity profile along the *b* axis of the crystal, exhibiting that the measured distance of 2.49 Å and 1.61 Å formed between two distinct positions of Te atoms bonding to the W atom. Subsequently, the overlaid atomic structural model was used to simulate the STEM image, as shown in Figure 4.8a, and the simulation result is in good agreement with the experimental image. Furthermore, it is found that two different stacking sequences exist in the bilayer WTe_2, which is similar to other 2D materials. The atomic structures of two WTe_2 bilayer regions are shown in Figure 4.8c and Figure 4.8d. Figure 4.8c shows a bilayer stacking of WTe_2. It shows that the

second layer is mirror symmetric to the first layer along the *b* axis of the WTe_2 unit cell, as shown by the dashed diamonds (top view of the structural model) in Figure 4.8c.

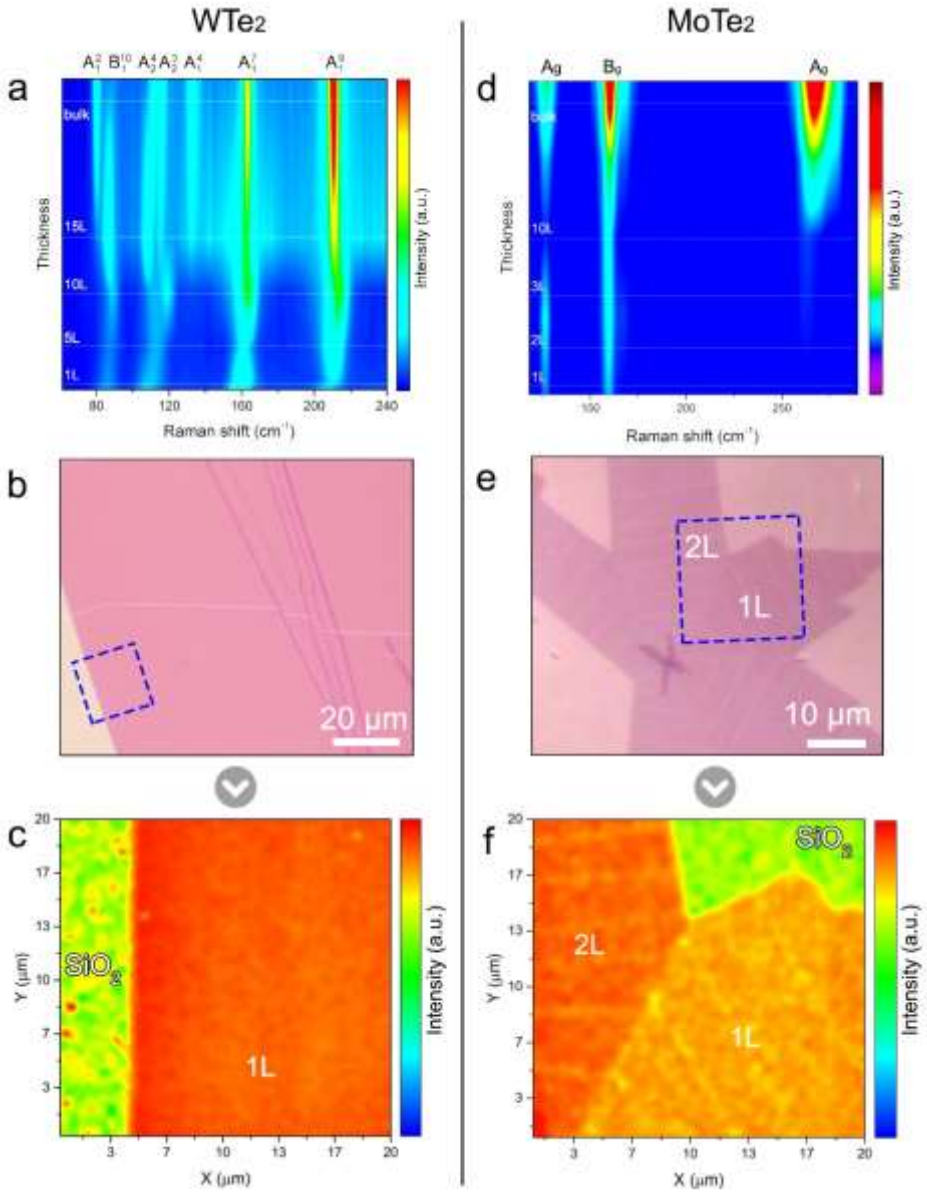

Figure 4.6 Raman spectra and mapping of WTe_2 and $MoTe_2$ monolayers. (a) Raman spectra of WTe_2 with different thickness. (b) Optical image of a monolayer WTe_2. (c) Raman intensity mapping using A_1^9 from the region in b. (d) Raman spectra of $MoTe_2$ with different thickness. (e) Optical image of monolayer and bilayer $MoTe_2$. (f) Raman intensity mapping of A_g at 161 cm^{-1}.

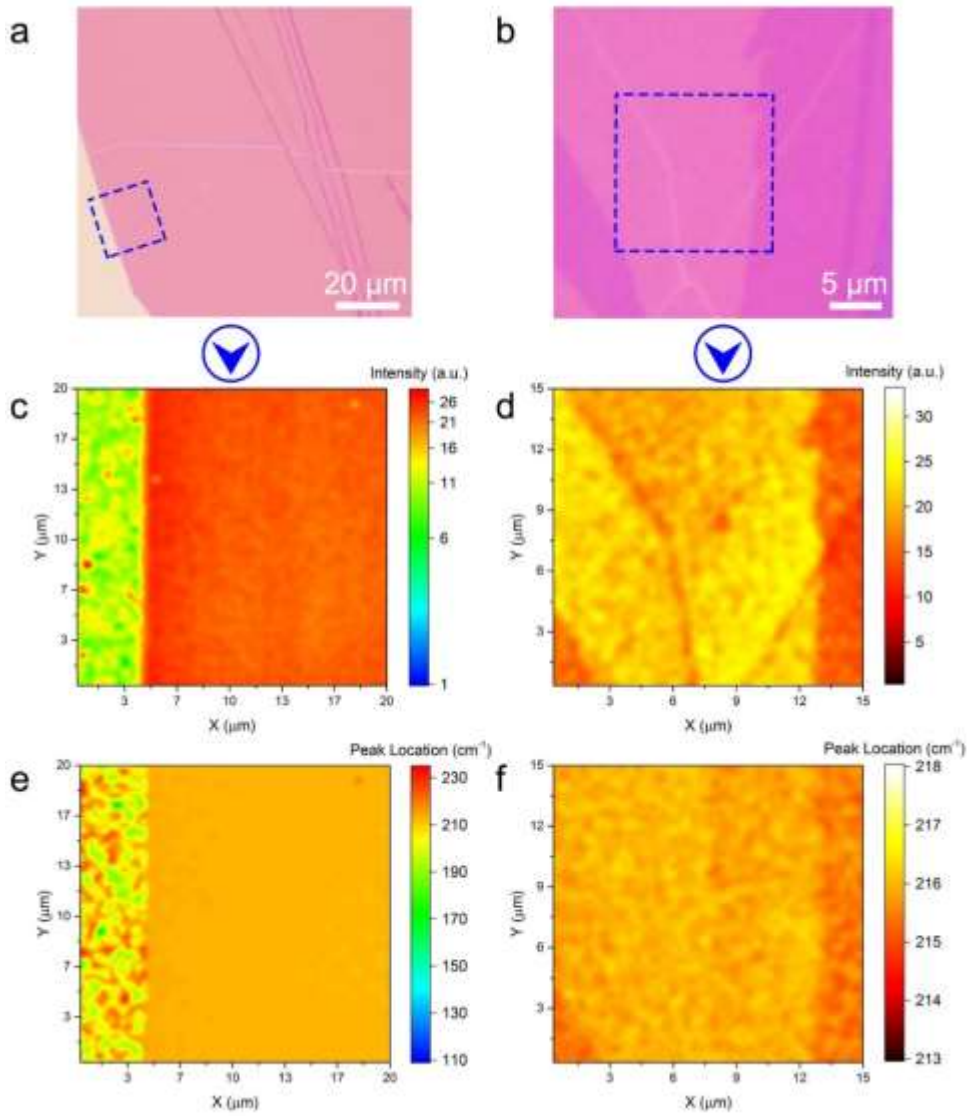

Figure 4.7 Raman mapping of monolayer and bilayer WTe_2. (a) Optical image of a large monolayer WTe_2. The corresponding Raman intensity and Raman center mapping are shown in c and e, respectively. (b) Optical image of bilayer WTe_2. (d and f) The corresponding Raman intensity and center mapping of bilayer WTe_2 with grain boundary, respectively.

Another stacking pattern of bilayer WTe_2 (Figure 4.8d) shows shift of half of a unit cell along *b* axis for the second layer of WTe_2, as illustrated in the structural model, which is different from the 2H structure. This stacking is called as 2H′ stacking. The both stacking patterns form periodic stripe patterns consisting of overlapped Te and W-Te chains from the two layers, which is in good agreement with the simulated result. The atomically sharp

stacking boundary between the 2H and 2H′ stacking domains is shown in Figure 4.8e.[28] DFT calculations were carried out to study the mirror twin boundary, as shown in Figure 4.8f. The Te_2 columns are misaligned in the relaxed structure, which is different from that observed in other TMDs.[29-31] The density of states (DOS) in Figure 4.8f reveals that the W atoms in the mirror twin boundary have more states at the Fermi level, indicating that they are more metallic than the bulk counterpart. This structure is very important for the electrical behavior of monolayer and few-layer WTe_2 and also shows potential implications on the quantum spin Hall effect in WTe_2. The further characterizations of thick flakes WTe_2, as shown in Figure 4.9, indicate the high quality of as-synthesized sample.

The as-synthesized atomic layered $MoTe_2$ has the same structure as the 1T′ phase WTe_2, as shown in Figure 4.10, where the electron-energy-loss spectra (EELS) are provided for direct comparisons between the two materials. Monolayer $MoTe_2$ shows the same atomic structure as WTe_2 (1T′ quasi-one dimensional chains), but different intensity distribution in the atomic columns in the STEM images. Interestingly, in the multiple layer samples, the interlayer stacking of WTe_2 is slightly different from $MoTe_2$ in the room temperature (the temperature for the STEM experiment). WTe_2 is in 1Td stacking phase while $MoTe_2$ is in 1T′, which consists of a distorted unit cell with the misaligned layers. Such $MoTe_2$ is analogous to the direct stacking layers on each other reported in literature.[5] STEM images show that the shape of the atomic columns in $MoTe_2$ few layers (Figure4.10a) are different from that in WTe_2 few layer (Figure 4.10b) when a small tilting is presented due to the small interlayer misalignment. This is confirmed by the simulated images. EELS spectra exhibit that the Te $N_{4,5}$ edge is overlapped with Mo $N_{2,3}$ and W $O_{2,3}$ edge, respectively, leading to a distinct shape of their EELS spectrum.

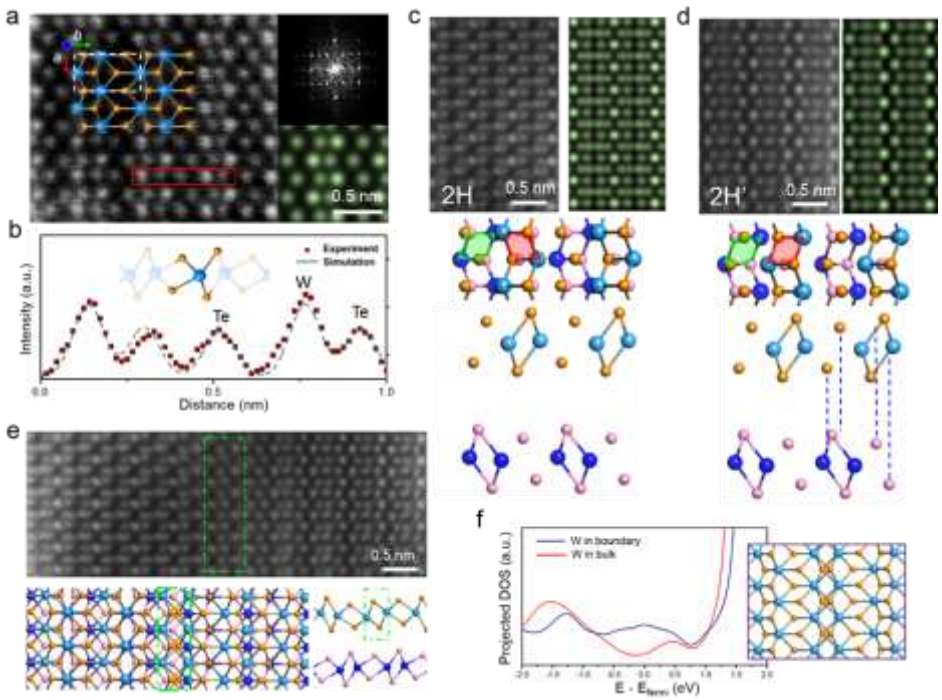

Figure 4.8 STEM characterization of WTe_2 atomic layer. (a) STEM Z-contrast image of a monolayer WTe_2. The coordinate and structural model are overlaid on the image. Insets: FFT pattern and simulated STEM image of the monolayer WTe_2. (b) Line intensity profile file of the region highlighted by red rectangle in a. (c, d) STEM Z-contrast image of a bilayer WTe_2 with 2H stacking c and 2H' stacking (d). The green and red dash diamonds indicate the orientation of the zigzag W-Te chains in the first and second layer, respectively. 2H and 2H′ stacking is differed by half of a unit cell shifting along the *b* aixs in the second layer. Images in green are simulated images. (e) STEM Z-contrast image of an atomically sharp stacking boundary between the 2H (left) and 2H′ (right) stacking. The structural model is optimized by DFT calculations. (f) Projected DOS of the W atoms in the mirror twin boundary and in the bulk, showing more states near the Fermi level for W atoms in the boundary region. Inset: the structural model of the mirror twin boundary.

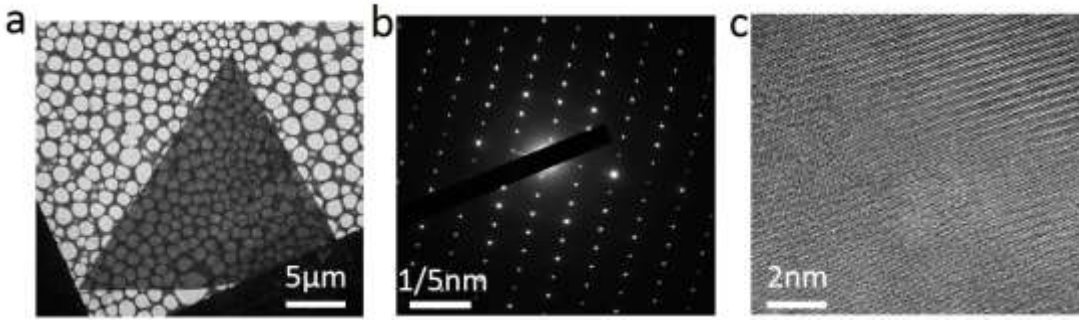

Figure 4.9 TEM characterize of WTe_2 flakes. a, Low magnification TEM imaging of WTe_2 thick flake. The triangle WTe_2 flake can be seen in Figure 4.9a and b, the selected area electron diffraction (SAED) in a, which shows reciprocal lattice of the WTe_2 single crystal. c is the high resolution image of WTe_2 in a and b, and c show the high quality of the thick WTe_2 flakes.

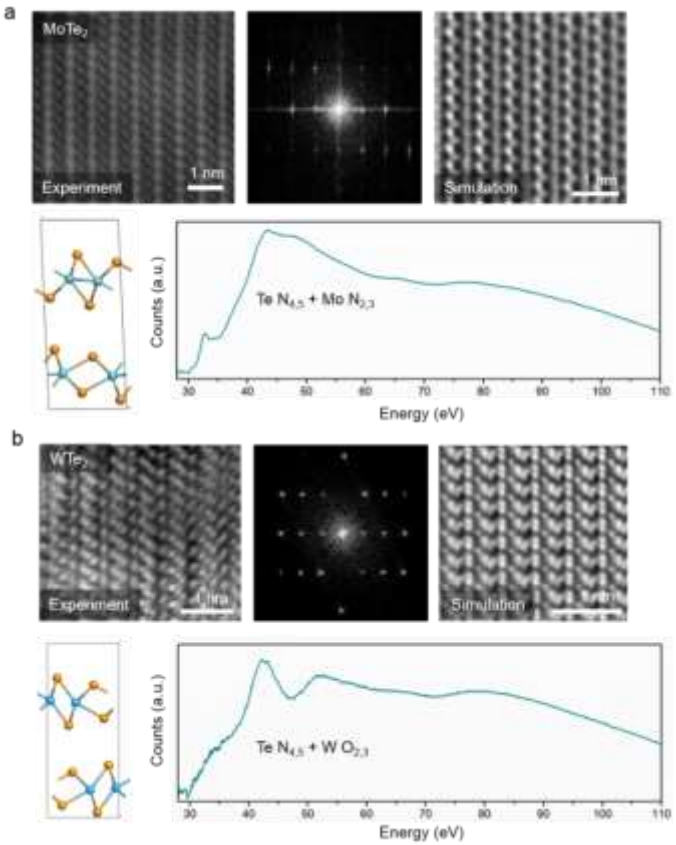

Figure 4.10 Atomic structure of $MoTe_2$ and WTe_2 few layers. a, b Experimental STEM image, FFT pattern, simulated STEM images with corresponding atomic model and EELS spectra of $MoTe_2$ (a) and WTe_2 (b) few layer. $MoTe_2$ and WTe_2 are very similar in structures. The simulations were done on a 6-layer model with a small tilting away from the [001] direction.

4.2.4 Performance of WTe_2 and $MoTe_2$

Layered ditelluride crystals provide a wonderful platform to study their electric transport. Figure 4.11 shows the measured field- and temperature-dependent transport properties of WTe_2 with different thickness. The corresponding optical images and AFM images of WTe_2 devices are shown in Figure 4.12. The temperature-dependent resistivity in WTe_2 flakes including the thickness of ~ 4 nm (5 layer WTe_2) and ~2 nm (2 layer WTe_2) is shown in Figure 4.11a. The resistivity of WTe_2 few layer shows abnormal insulating behavior with and without the magnetic field under different temperature, which is different from those have been observed in the bulk WTe_2 crystals.[5] Note that, the resistivity of 5 layer sample decreases monotonically with decreasing temperature (above 50 K) under zero magnetic field (0T) (Figure 4.11a), which is similar to the transport properties observed in bulk WTe_2, indicating that WTe_2 maintains the metallic behavior even thinned to 4 nm (down to 5 layers). However, a turning point appears with the further decreasing temperature, and the resistance of the samples starts to increase. This phenomenon is attributed to the electron-electron interactions at the reduced dimensions.[32] However, the bilayer WTe_2 flake displays solely insulating behavior under zero magnetic field, indicating the semimetal-to-insulator transition originating from the effect of the reduced thickness, which has been observed in mechanically exfoliated WTe_2 and $MoTe_2$ few layer.[20, 33] The insulating state may be contributed to the Anderson localization or band gap opening in two dimensional limit.

Figure 4.11b shows the magnetoresistance (MR) calculated by $MR=[\rho(H)-\rho(0)]/\rho(0)$ of bilayer WTe_2 under different temperature as a function of the magnetic field. The large and non-saturating magnetoresistance are observed in the CVD-grown WTe_2 samples even thinned to 2 nm, demonstrating the high quality of as-produced samples. The MR is about 28% at 2 K. Moreover, for the thicker WTe_2 flakes (12 nm), the MR reaches a maximum value of 2000% at 25K in the magnetic field of 10T, as shown in Figure 4.13. It should be noted that the obtained MR values on the few layer WTe_2 are lower than that reported in the WTe_2 bulk crystal.[2, 5]

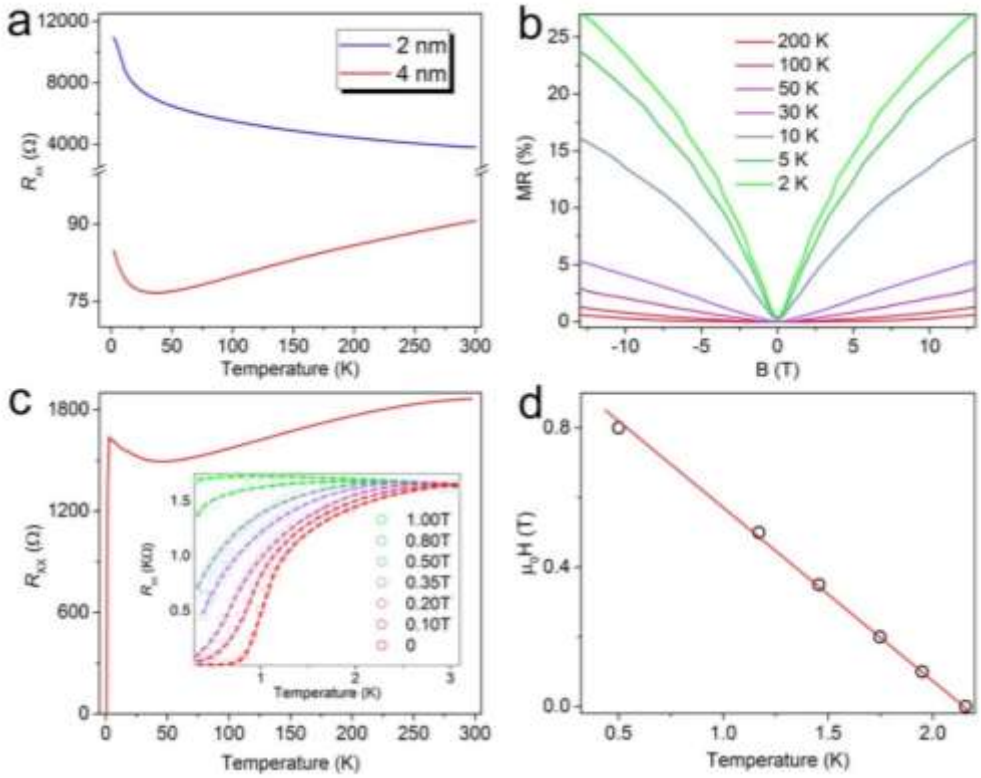

Figure 4.11 Transport in different thicknesses of WTe_2 and superconductivity in few layered $MoTe_2$. (a) The resistance of 4 nm and 2 nm WTe_2 flakes at different temperature under zero magnetic field, respectively. (b) Field-dependent magnetoresistance of 2 nm WTe_2 flake under different temperatures. (c) Superconducting transition behavior of a few layered $MoTe_2$ under zero magnetic field. (Inset: Superconductivity at different perpendicular magnetic fields). (d) The upper critical field H_{c2} under dependence temperature. The solid red line is the linear fit to H_{c2}.

Superconducting behavior has been observed in the exfoliated $MoTe_2$. Here, the devices using different thickness of $MoTe_2$ were fabricated by e-beam lithography (EBL). The optical image of the $MoTe_2$ devices is shown in Figure 4.14. Figure 4.11c shows the temperature-dependent longitudinal resistance R_{xx} of a few layer $MoTe_2$ device under different perpendicular magnetic fields. It is notable that the R_{xx} decreases from 300K to 40K, demonstrating a metallic behavior of the sample, which is similar to the previous reported result on exfoliated $MoTe_2$.[20] With temperature further decreasing, the sample shows a superconducting behavior at the temperature T=2.5K, especially, the zero

resistance presents at T_c=0.5K. Surprisingly, the temperature of superconducting transition behavior in thinner sample is enhanced compared with that reported in bulk counterpart T_c=0.1K.[34] This phenomenon has also been observed in 2H TaS_2.[35] This phenomenon is attributed to the effective electron–phonon coupling constant in thinner samples. The temperature-dependent longitudinal resistance R_{xx} in different perpendicular magnetic fields is inserted in Figure 4.11c. The superconducting transition temperature can be defined when the resistance drops to 10% of the normal state resistance R_N. The systematically shifted T_c to lower temperatures can be observed with increasing magnetic fields *B*. The superconductivity was almost completely suppressed when the applied magnetic field is larger than 1T. The upper critical field H_{c2}-T_c phase diagram are summarized in Figure 4.11d. It is found that the H_{c2} and T_c show linear relationship near T_c. This can be explained by the standard linearized Ginzburg-Landau (GL) theory,

$$H_{c2}(T) = \frac{\phi_0}{2\pi\xi_{GL}(0)^2}\left(1 - \frac{T}{T_c}\right)$$

where GL in-plane coherence length, $\xi_{GL}(0)$ is the zero-temperature, and ϕ_0 is the magnetic flux quantum. The coherence length is shown to be 38 nm.

4.3 Conclusions

To summarize, large-size ditellurides including WTe_2 and $MoTe_2$ were synthesized by CVD method. High-resolution STEM imaging revealed the atomic structure of WTe_2 and $MoTe_2$. The domain wall in bi-layer WTe_2 with stacking boundary and two distinct stacking sequences were observed. Transport measurements demonstrated the semimetal-to-insulator transition in WTe_2 and enhanced superconductivity in $MoTe_2$. This work opens up a new approach to synthesis of telluride materials and offers the possibility to realize the quantum spin Hall devices.

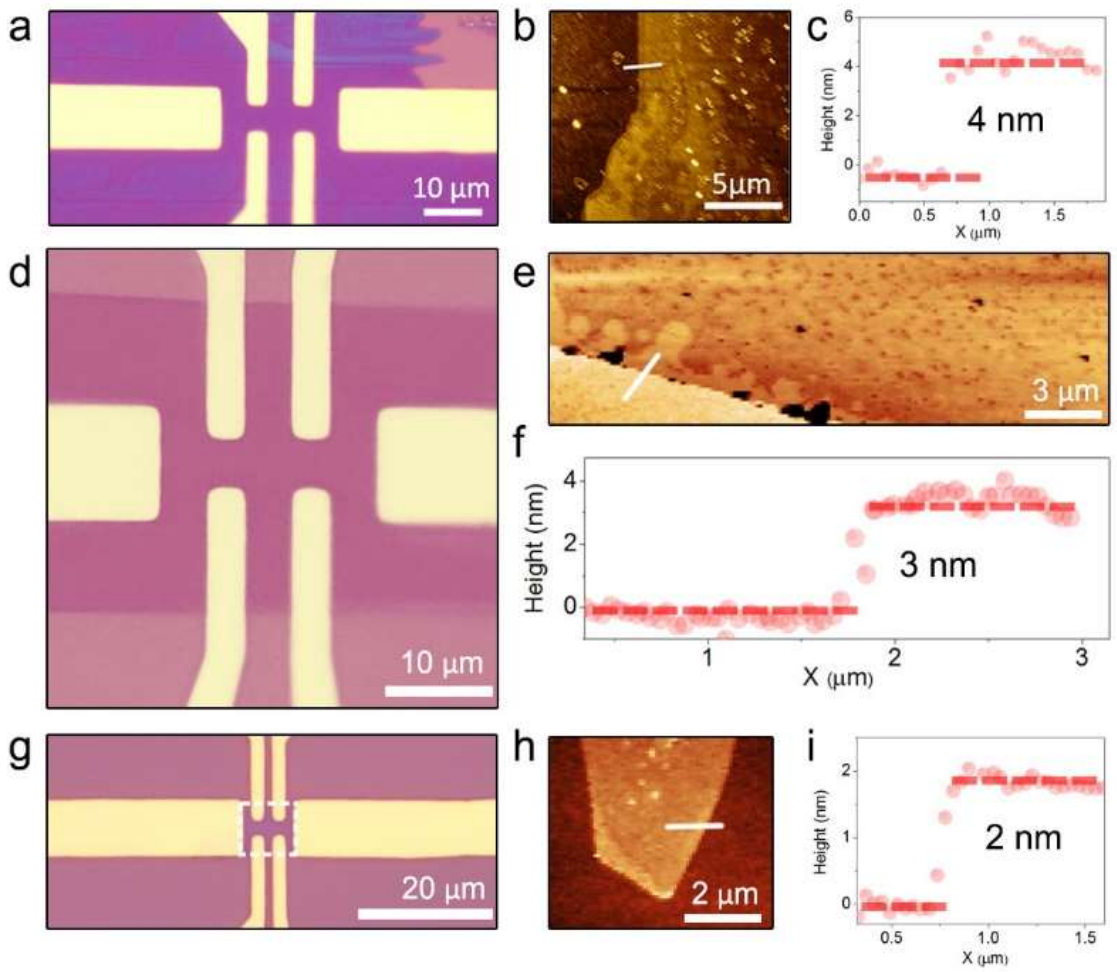

Figure 4.12 AFM images of the WTe_2 flakes used in the devices. (a, d, and g) Show optical images of the devices and samples with 4 nm, 3nm and 2nm, respectively. The 2 nm WTe_2 is highlighted by the dotted square in g due to its low contrast. b, e, and h are corresponding AFM high profiles of the WTe_2 samples in a, d, and g, respectively. Their thicknesses are shown in c, f, and i, respectively.

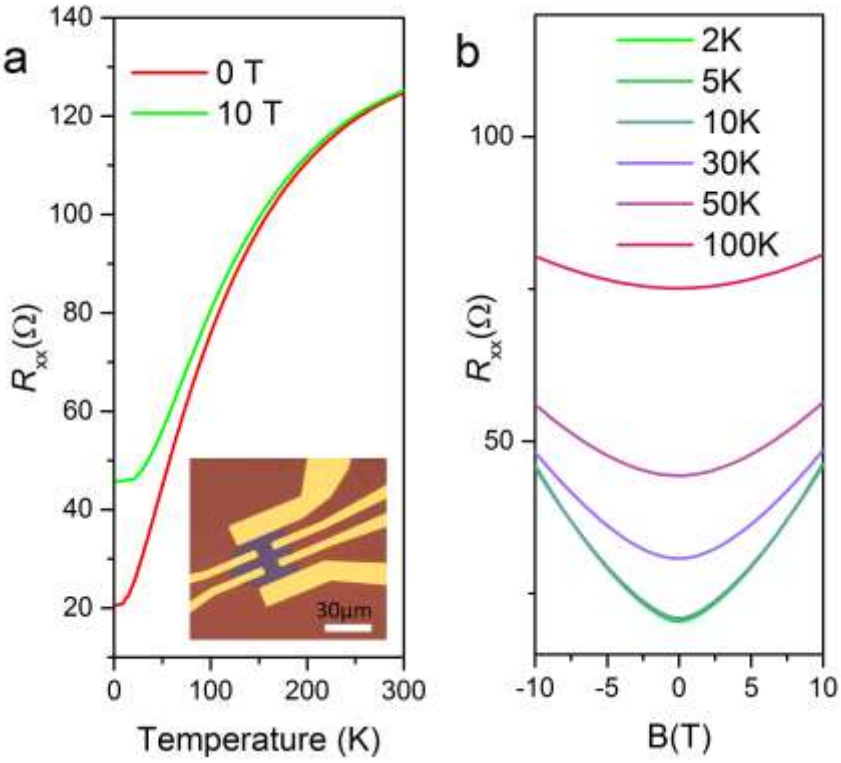

Figure 4.13 Magnetoresistance of thick WTe_2 flakes. For the 12 nm WTe_2 flake, the resistivity decrease with the temperature decreased. The MR is about 2000%, which is large than that in the few layers WTe_2 and smaller than the reported result in the thickness of 70 nm and bulk WTe_2, respectively. The result shows that the magnetoresistance decreases with decreasing thickness of WTe_2 flake.

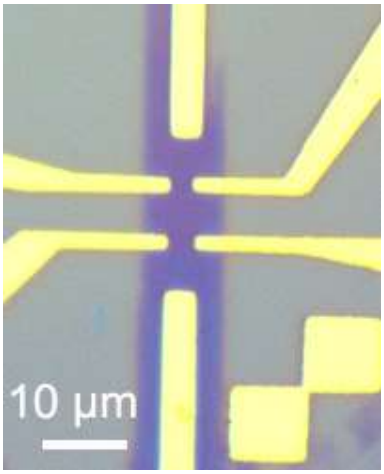

Figure 4.14 Optical image of $MoTe_2$ device.

References

[1] Z. Y. Yin, H. Li, H. Li, L. Jiang, Y. M. Shi, Y. H. Sun, G. Lu, Q. Zhang, X. D. Chen, H. Zhang, Acs Nano 2012, 6, 74.

[2] D. Xiao, G. B. Liu, W. X. Feng, X. D. Xu, W. Yao, Phys Rev Lett 2012, 108.

[3] K. K. Liu, Y. H. Lee, Y. C. Lin, J. K. Huang, X. Q. Zhang, T. W. Lin, L. J. Li, Low-Dimensional Nanoscale Electronic and Photonic Devices 5 -and- State-of-the-Art Program on Compound Semiconductors 54 (Sotapocs 54) 2012, 50, 61.

[4] C. X. Cong, J. Z. Shang, X. Wu, B. C. Cao, N. Peimyoo, C. Qiu, L. T. Sun, T. Yu, Adv Opt Mater 2014, 2, 131.

[5] M. N. Ali, J. Xiong, S. Flynn, J. Tao, Q. D. Gibson, L. M. Schoop, T. Liang, N. Haldolaarachchige, M. Hirschberger, N. P. Ong, R. J. Cava, Nature 2014, 514, 205.

[6] J. K. Huang, J. Pu, C. L. Hsu, M. H. Chiu, Z. Y. Juang, Y. H. Chang, W. H. Chang, Y. Iwasa, T. Takenobu, L. J. Li, Acs Nano 2014, 8, 923.

[7] X. L. Wang, Y. J. Gong, G. Shi, W. L. Chow, K. Keyshar, G. L. Ye, R. Vajtai, J. Lou, Z. Liu, E. Ringe, B. K. Tay, P. M. Ajayan, Acs Nano 2014, 8, 5125.

[8] K. Kang, S. E. Xie, L. J. Huang, Y. M. Han, P. Y. Huang, K. F. Mak, C. J. Kim, D. Muller, J. Park, Nature 2015, 520, 656.

[9] H. L. Zhou, C. Wang, J. C. Shaw, R. Cheng, Y. Chen, X. Q. Huang, Y. Liu, N. O. Weiss, Z. Y. Lin, Y. Huang, X. F. Duan, Nano Lett 2015, 15, 709.

[10] D. Dumcenco, D. Ovchinnikov, K. Marinov, P. Lazic, M. Gibertini, N. Marzari, O. L. Sanchez, Y. C. Kung, D. Krasnozhon, M. W. Chen, S. Bertolazzi, P. Gillet, A. F. I. Morral, A. Radenovic, A. Kis, Acs Nano 2015, 9, 4611.

[11] Y. H. Chang, W. Zhang, Y. Zhu, Y. Han, J. Pu, J. K. Chang, W. T. Hsu, J. K. Huang, C. L. Hsu, M. H. Chiu, T. Takenobu, H. Li, C. I. Wu, W. H. Chang, A. T. S. Wee, L. J. Li, Acs Nano 2014, 8, 8582.

[12] W. Zhang, M. H. Chiu, C. H. Chen, W. Chen, L. J. Li, A. T. S. Wee, Acs Nano 2014, 8, 8653.

[13] Y. J. Gong, J. H. Lin, X. L. Wang, G. Shi, S. D. Lei, Z. Lin, X. L. Zou, G. L. Ye, R. Vajtai, B. I. Yakobson, H. Terrones, M. Terrones, B. K. Tay, J. Lou, S. T. Pantelides, Z. Liu, W. Zhou, P. M. Ajayan, Nat Mater 2014, 13, 1135.

[14] X. D. Duan, C. Wang, J. C. Shaw, R. Cheng, Y. Chen, H. L. Li, X. P. Wu, Y. Tang, Q. L. Zhang, A. L. Pan, J. H. Jiang, R. Q. Yu, Y. Huang, X. F. Duan, Nat Nanotechnol 2014, 9, 1024.

[15] C. M. Huang, S. F. Wu, A. M. Sanchez, J. J. P. Peters, R. Beanland, J. S. Ross, P. Rivera, W. Yao, D. H. Cobden, X. D. Xu, Nat Mater 2014, 13, 1096.

[16] M. Y. Li, Y. M. Shi, C. C. Cheng, L. S. Lu, Y. C. Lin, H. L. Tang, M. L. Tsai, C. W. Chu, K. H. Wei, J. H. He, W. H. Chang, K. Suenaga, L. J. Li, Science 2015, 349, 524.

[17] K. Ikeura, H. Sakai, M. S. Bahramy, S. Ishiwata, Apl Mater 2015, 3.

[18] J. E. Callanan, G. A. Hope, R. D. Weir, E. F. Westrum, J Chem Thermodyn 1992, 24, 627.

[19] D. F. Kang, Y. Z. Zhou, W. Yi, C. L. Yang, J. Guo, Y. G. Shi, S. Zhang, Z. Wang, C. Zhang, S. Jiang, A. G. Li, K. Yang, Q. Wu, G. M. Zhang, L. L. Sun, Z. X. Zhao, Nat Commun 2015, 6.

[20] D. H. Keum, S. Cho, J. H. Kim, D. H. Choe, H. J. Sung, M. Kan, H. Kang, J. Y. Hwang, S. W. Kim, H. Yang, K. J. Chang, Y. H. Lee, Nat Phys 2015, 11, 482.

[21] X. F. Qian, J. W. Liu, L. Fu, J. Li, Science 2014, 346, 1344.

[22] M. K. Jana, A. Singh, D. J. Late, C. R. Rajamathi, K. Biswas, C. Felser, U. V. Waghmare, C. N. R. Rao, J Phys-Condens Mat 2015, 27.

[23] Y. Kim, Y. I. Jhon, J. Park, J. H. Kim, S. Lee, Y. M. Jhon, Nanoscale 2016, 8, 2309.

[24] Y. C. Jiang, J. Gao, L. Wang, Sci Rep-Uk 2016, 6.

[25] M. Kan, H. G. Nam, Y. H. Lee, Q. Sun, Phys Chem Chem Phys 2015, 17, 14866.

[26] L. Zhou, K. Xu, A. Zubair, A. D. Liao, W. J. Fang, F. P. Ouyang, Y. H. Lee, K. Ueno, R. Saito, T. Palacios, J. Kong, M. S. Dresselhaus, J Am Chem Soc 2015, 137, 11892.

[27] J. C. Park, S. J. Yun, H. Kim, J. H. Park, S. H. Chae, S. J. An, J. G. Kim, S. M. Kim, K. K. Kim, Y. H. Lee, Acs Nano 2015, 9, 6548.

[28] L. Brown, R. Hovden, P. Huang, M. Wojcik, D. A. Muller, J. Park, Nano Lett 2012, 12, 1609.

[29] X. Lu, M. I. B. Utama, J. H. Lin, X. Gong, J. Zhang, Y. Y. Zhao, S. T. Pantelides, J. X. Wang, Z. L. Dong, Z. Liu, W. Zhou, Q. H. Xiong, Nano Lett 2014, 14, 2419.

[30] A. M. van der Zande, P. Y. Huang, D. A. Chenet, T. C. Berkelbach, Y. M. You, G. H. Lee, T. F. Heinz, D. R. Reichman, D. A. Muller, J. C. Hone, Nat Mater 2013, 12, 554.

[31] J. H. Lin, S. T. Pantelides, W. Zhou, Acs Nano 2015, 9, 5189.

[32] J. Hu, X. Liu, C. L. Yue, J. Y. Liu, H. W. Zhu, J. B. He, J. Wei, Z. Q. Mao, L. Y. Antipina, Z. I. Popov, P. B. Sorokin, T. J. Liu, P. W. Adams, S. M. A. Radmanesh, L. Spinu, H. Ji, D. Natelson, Nat Phys 2015, 11, 471.

[33] L. Wang, I. Gutierrez-Lezama, C. Barreteau, N. Ubrig, E. Giannini, A. F. Morpurgo, Nat Commun 2015, 6.

[34] Y. P. Qi, P. G. Naumov, M. N. Ali, C. R. Rajamathi, W. Schnelle, O. Barkalov, M. Hanfland, S. C. Wu, C. Shekhar, Y. Sun, V. Suss, M. Schmidt, U. Schwarz, E. Pippel, P. Werner, R. Hillebrand, T. Forster, E. Kampert, S. Parkin, R. J. Cava, C. Felser, B. H. Yan, S. A. Medvedev, Nat Commun 2016, 7.

[35] E. Navarro-Moratalla, J. O. Island, S. Manas-Valero, E. Pinilla-Cienfuegos, A. Castellanos-Gomez, J. Quereda, G. Rubio-Bollinger, L. Chirolli, J. A. Silva-Guillen, N. Agrait, G. A. Steele, F. Guinea, H. S. J. van der Zant, E. Coronado, Nat Commun 2016, 7.

Chapter 5

TiX_2, VX_2 and NbX_2 2D TMDs

In this part, an effective and general synthetic strategy for producing TiX_2, VX_2 and NbX_2 (X: S, Se and Te), via molten-salt-assisted chemical vapor method will be introduced. These materials include a variety from semiconductors to semimetals, and even superconductors. Raman and PL spectroscopy were used to check the quality of the as-synthesized TiX_2, VX_2 and NbX_2. Scanning transmission electron microscopy (STEM) was performed to examine the atomic structures. Superconductivity in monolayer $NbSe_2$ indicates the high quality of as-synthesized 2D TMDs.

5.1 Introduction

Compared to the bulk counterparts, two-dimension (2D) transition-metal dichalcogenides (TMDs) show fantastic physical properties including 2D quantum-spin Hall effect (QSH), 1D charge density waves, valley polarization, etc.[1-9] By far, being the biggest family in 2D crystals, only a limited number of 2D TMDs have been produced, commonly via vapor deposition by sulfurization, selenization and tellurization of metals and metal compounds.[10-13] Among them, synthesis of large-size and monolayered TMD single crystal is still challenging. In the past few years, most of the synthetic work focused mostly on group-VI MX_2 (M: Mo, W; X: S, Se) compounds[14-17] and more than 40 TMDs are yet to be explored.[18] Note that many of them possess of diverse novel properties predicted by theory such as: high-mobility and phase-transition TMDs (Ti, Zr, Hf) in Group-IV;[19, 20] ferromagnetic monolayers, superconductors and charge density wave (CDW) effects in Group-V;[21-24] the type-II Weyl semimetals and topological insulators in group-VI tellurides;[25-27] and Re-, Pt-, Pd- and Fe-based TMDs in groups VII and VIII. Based on the discussion in the literature review part, I selected the TiX_2, VX_2 and NbX_2 TMDs as the research objectives.

5.2 Results and Discussion

5.2.1 Optical images, RM, and AFM of TiX_2

TiS_2, a new typical transition metal dichacogenide, is a semiconductor with a small band gap.[28] Monolayer TiS_2 consisting of S-Ti-S layers is considered as a promising candidate for potential applications in electronic because of its electronic structure. Theoretical work shows that monolayer TiS_2 crystal presents high-conductive properties. In order to study the property of TiS_2 few layer or monolayer, researchers have been trying to produce it by different methods. For instance, the TiS_2 nanocrystallities have been synthesized on Au (111).[28] However, to date, monolayer TiS_2 has not been reported . Here, a new molten salt-assisted CVD method is designed to grow the monolayered TiS_2, few-layered $TiSe_2$ and $TiTe_2$ for the first time. Figure 5.1a shows optical image of monolayered TiS_2 with

size of ~ 50 μm. The corresponding Raman spectrum (Figure 5.1b) shows that the Raman peaks located at 230 cm^{-1} and 332 cm^{-1} are the same as previous reported results, conforming that the flake is TiS_2 crystal. AFM image (Figure 5.1c) exhibits a thickness of ~ 0.9 nm for the TiS_2, demonstrating that the as-synthesized TiS_2 is monolayer. Compared with TiS_2, the octahedral titanium diselenide (1T-$TiSe_2$) is a semimetal and shows a charge-density wave (CDW) and superconductivity in its phase diagram.[29] The excellent physical phenomena analogous to other layered systems like copper oxides have attracted intense interest.[20] The phase change of $TiSe_2$ has been studied by applying an electric field in the exfoliated flakes and the superconductivity has been observed through chemical doping, such as Cu_xTiSe_2.[30] However, these properties have not been studied in the $TiSe_2$ few-layer or monolayer. Herein, the monolayered and few-layered $TiSe_2$ which can be used to study the superconductivity and phase transition are synthesized using this method. Figure 5.1d shows the optical image of few-layered $TiSe_2$ with size of ~30 μm. The Raman peaks locate at 190 cm^{-1} and 250 cm^{-1} are assigned to A_{1g} and E_{1g} modes, respectively (Figure 5.1e). In order to check the thickness of as-prepared $TiSe_2$, AMF measurement was further carried out, as shown in Figure 5.1f. The thickness of ~ 2 nm illustrates that the as-grown $TiSe_2$ is bilayer.

Similarly, $TiTe_2$ is also a layered transition metal dichalcogenide compound, and shows the semimetal property. Exfoliated $TiTe_2$ flakes reveal the CDW effect under different temperatures.[31] However, exploring the properties in $TiTe_2$ is still in a nascent stage. Here, the few-layered $TiTe_2$ was synthesized using the molten salt-assisted CVD method. Figure 5.1g shows optical image of $TiTe_2$ with a size of up to 10 μm. Raman spectrum of $TiTe_2$ (Figure 5.1h) exhibits the Raman peaks locate at around 90 cm^{-1}, 120 cm^{-1}, and 140 cm^{-1}, which are similar to the previous reported results. Specifically, the Raman peaks locating at 120 cm^{-1} and 140 cm^{-1} are ascribed to the vibration of A_{1g} and E_{1g}, respectively. AFM image, as shown in Figure 5.1i, displays that the thickness of the flake is about 5 nm, revealing 8 layers of the as-synthesized $TiTe_2$.

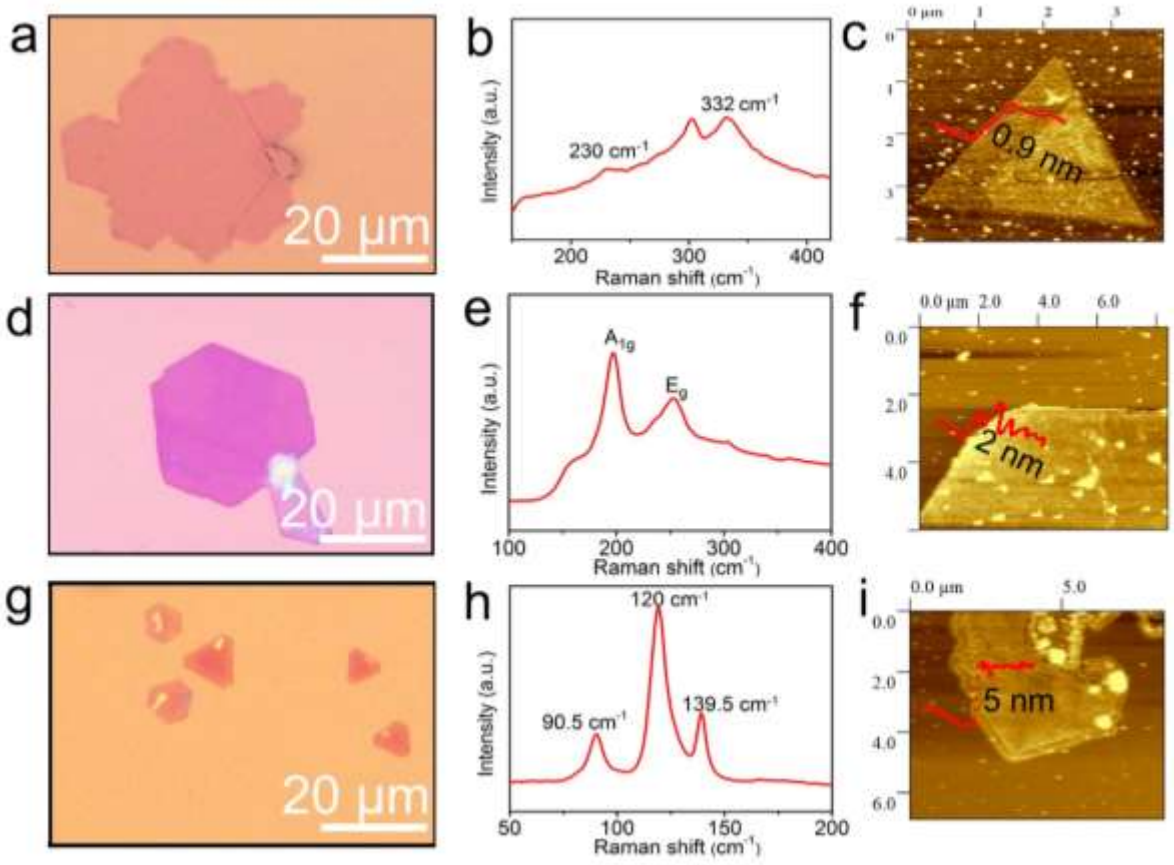

Figure 5.1 Characterizations of TiX_2 (X: S, Se, Te). (a) Optical image of monolayer TiS_2 with size of 50 μm. The corresponding Raman spectrum is shown in b, the Raman peaks located at 230 cm^{-1} and 332 cm^{-1} are the same as the reported result. (c) AFM image. The thickness of the TiS_2 is about 0.9 nm. (d) Optical image of few-layer $TiSe_2$. The corresponding Raman spectrum is shown in (e). The Raman peaks at 190 cm^{-1} and 250 cm^{-1} are ascribed to the A1g mode and E1g mode of $TiSe_2$, respectively. AFM image of bilayer $TiSe_2$ is shown in (f), where the height of the flake is about 2 nm. (g) Optical image of $TiTe_2$ with a size of around 10 μm. The Raman spectrum is shown in (h). The thickness of the flake is shown in (i), revealing ~8 layers of the as-produced $TiTe_2$.

5.2.2 Optical images, RM, and AFM of VX_2

VX_2 crystals which are the layered TMDs in group V, transfer from metals to semimetals when their thickness reduces to bilayer or monolayer. Theoretical results show that magnetism exists in the pristine VS_2, VSe_2 and VTe_2 monolayers.[24] VS_2 and VSe_2 have

been prepared and applied in the energy field such as supercapacitors and hydrogen evaluation reaction,[32] however, synthesis of monolayer VX_2 has not been reported. In order to prepare atom-thin VX_2, the V_2O_5 and S, Se, or Te were used as the reaction sources and the KI was used as the molten salt in this thesis. The procedure is presented as follows: the mixed powder of 1 mg KI and 3 mg V_2O_5 in the alumina boat was placed in the center of the tube, and another alumina boat containing S, Se or Te powder was placed in the upstream. The Silicon wafer with 285 nm top layer was put on the alumina boat with surface down. The furnace was heated with a ramp rate of 50 ºC/min to the growth temperatures from 600 ºC to 750 ºC, and held at this temperature for 15 mins before cooling down to room temperature naturally. The mixed Ar/H_2 gas was used as the carrier gas with the flow rate of 80/16 sccm. Figure 5.2a shows optical images of VS_2 flakes with the size of 30 μm. Figure 5.2b shows Raman spectrum of VS_2. The vibration of 2-photonon and A_{1g} analogous to the previously reported results, confirms that the as-synthesized flakes are VS_2 crystals.[33] It should be noted that the thickness of VS_2 is about 0.7 nm (Figure 5.2c), confirming the monolayer of the as-prepared VS_2. Surprisingly, optical image of VSe_2 (Figure 5.2d) shows the size is up to 50 μm. The corresponding Raman spectrum and AFM image of as-synthesized VSe_2 are given in Figure 5.2e and Figure 5.2f. The thickness of ~0.8 nm for the flake illustrates that the as-synthesized VSe_2 is monolayer, which can be further confirmed by STEM. Optical image of VTe_2 is shown in Figure 5.2g. Additionally, from Raman spectrum of VTe_2 (Figure 5.2h), one can see that the peaks locate at 117 cm^{-1} and 137 cm^{-1}, which are similar to the previous reported result.[33] However, it is difficult to obtain a VTe_2 monolayer. The thickness of the as-synthesized flake shown in Figure 5.2i is about 3 nm.

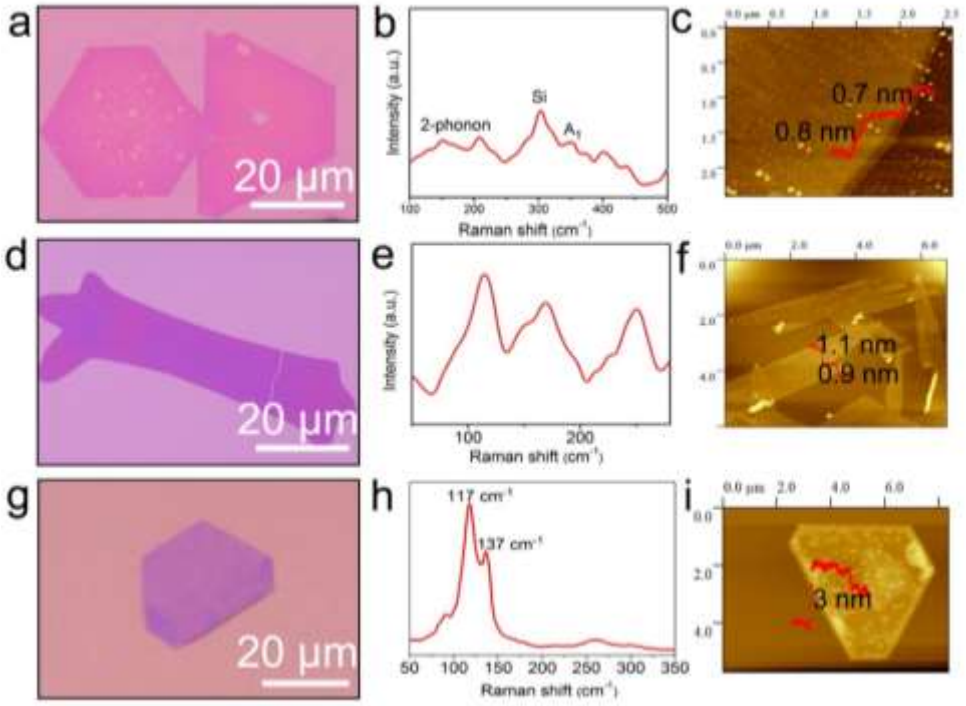

Figure 5.2 Characterizations of VX_2 (X: S, Se, and Te). (a) Optical image of VS_2. (b) Raman spectrum of VS_2. (c) AFM image of VS_2. The thickness is about 0.7 nm. (d) Optical image of VSe_2. (e) Raman spectrum of VSe_2. AFM image (0.8 nm) shown in (f) illustrates that the as-synthesized VSe_2 is monolayer. (g) Optical image of VTe_2. Raman spectrum in (h) shows the peaks located at 117 cm^{-1} and 137 cm^{-1}, which are similar to the previous reported result. (i) The thickness of the VTe_2 flakes.

5.2.3 Optical images, RM, and AFM of NbX_2

NbX_2 crystals, including NbS_2, $NbSe_2$ and $NbTe_2$, are semimetals. So far, many excellent properties such as superconductivity and CDW state in $NbSe_2$ have been observed.[34, 35] Synthesis of large-size monolayer NbX_2 is very critical to study their properties and applications.[36] Despite the thick NbS_2 flakes have been synthesized by CVD method, synthesis of monolayer NbX_2 is also challenging and has not been reported, especially for $NbSe_2$ and $NbTe_2$. Here, using the molten salt-assisted CVD method, large-size monolayer NbS_2, $NbSe_2$ and few-layer $NbTe_2$ were successfully synthesized. The corresponding procedures of synthesizing NbX_2 are almost same as that has been used for producing VX_2. Here, the growth temperature is set to be 800 ^oC. The mixed powder of 2 mg NaCl and10

mg Nb_2O_5 was used as the precursor. The Ar/H_2 with a flow rate of 80/16 sccm was used as the carrier gas. Figure 5.3a shows optical image of monolayer NbS_2 with ~ 80 μm in size. It should be pointing that it is the first time to report a large-size monolayer NbS_2 by using CVD approach. Raman peaks located at 306.7 cm^{-1}, 342.7 cm^{-1}, and 377.6 cm^{-1} are ascribed to the E1, E2, and A1 modes of pure NbS_2, respectively (Figure 5.3b). The observed thickness of ~ 0.7 nm demonstrates that the as-prepared NbS_2 is monolayer (Figure 5.3c). Along this strategy, large-sized $NbSe_2$ monolayer can also be obtained. The size of the as-grown monolaye $NbSe_2$ can be up to 50 μm (Figure 5.3d). Raman spectrum in Figure 5.3e confirms the high quality of the as-synthesized $NbSe_2$ monolayer. It is worth noting that Raman spectrum of the as-grown crystal shows two characteristic peaks, including the in-plane E2g mode at ~240 cm^{-1} and the out-of-plane A1g mode at ~220 cm^{-1}, respectively. The broad feature at ~180 cm^{-1} is described as a soft mode because of its frequency behavior with temperature. Figure 5.3f shows the thickness (0.8 nm) of as-synthesized $NbSe_2$, indicating that the as-grown $NbSe_2$ is monolayer. From optical image of $NbTe_2$ (Figure 5.3g), it can be seen that the thickness is thicker than that in NbS_2 and $NbSe_2$ due to the low chemical reactivity between V and Te. Also, Raman spectrum of VTe_2 is given in Figure 5.3h. However, only 4 nm-thickness few-layered VTe_2 was obtained, as shown in AFM image in Figure 5.3i.

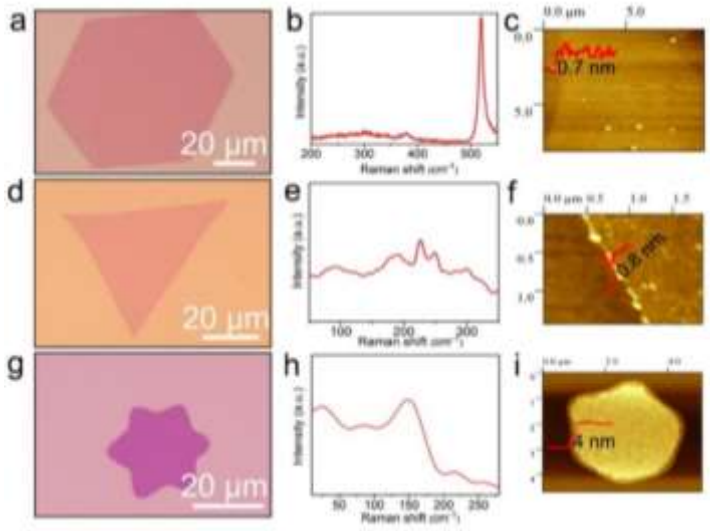

Figure 5.3 Characterizations of NbX_2 (X: S, Se, and Te). (a) Optical image of monolayer NbS_2. (b) Raman spectrum of the as-synthesized NbS_2 crystal. The thickness of 0.7 nm shown in (c) further

supports that the NbS_2 is monolayer. (d) Optical image of monolayer $NbSe_2$. (e) Raman spectrum of the as-synthesized $NbSe_2$ monolayer. The thickness of the flake (0.8 nm) confirms that the as-grown $NbSe_2$ is monolayer (f). (g) Optical image of the as-synthesized $NbTe_2$ few layer. (h) Raman spectrum of $NbTe_2$ crystal. (i) The thickness is around 4 nm of the as-synthesized $NbTe_2$.

5.2.4 SETM characterizations of TiS_2, VS_2 and NbS_2

In order to study the atomic structure of the as-synthesize TiX_2, VX_2 and NbX_2, STEM characterization was performed. Since these 2D TMDs are very easily oxidized by air and water, it is very difficult to obtain their atomic structure. In this thesis, the atomic structures of sulfides was studied because they are more stable than the selenides and tellurides. TiS_2 maintains the 1T structure and belongs to space group $P\bar{3}m1$ with a crystal lattice of a= 3.4071 Å, c=5.6953 Å. Figure 5.4a shows a high resolution Z-contrast STEM image of a monolayer TiS_2 region near the edge of the bilayered and few-layered TiS_2. Ti and S atoms can be easily identified by their distinguishable contrast, revealing the 1T phase with the hexagonal crystal structure. Energy dispersive x-ray spectra (EDS) and EELS of the as-synthesized TiS_2 flakes were provided in Figure 5.4b and 5.4c to confirm its chemical composition, showing that it consists of solely Ti and S elements without any impurities.

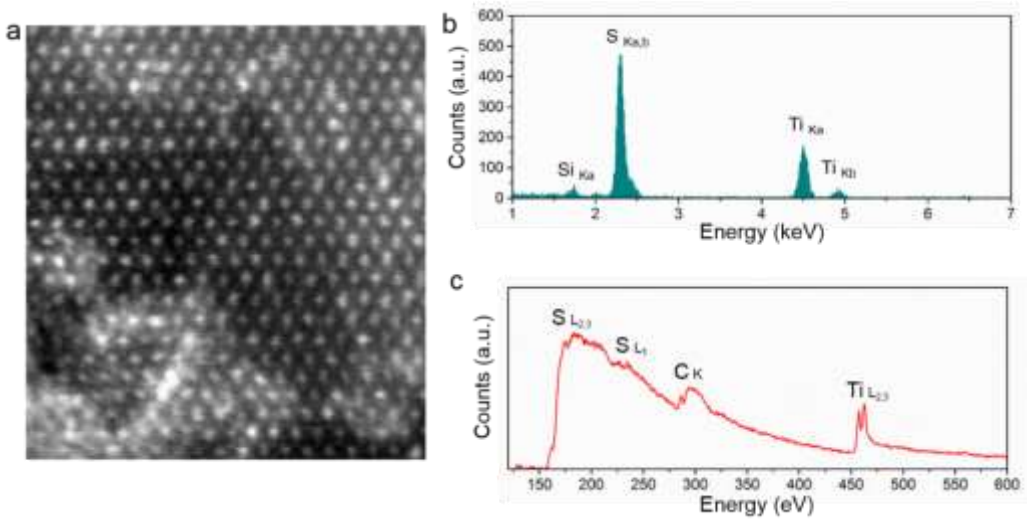

Figure 5.4 Atomic resolution STEM characterization of TiS_2. (a) STEM image of monolayer TiS_2. (b and c) EDS and EELS spectra of TiS_2 crystal.

VS_2 is in 1T structure that composes of layers of VS_6 octahedral separated by a van der Waals gap and belongs to space group $P\bar{3}m1$. The VS_2 monolayer is also sensitive to air and easy to be oxidized in the ambient condition. Figure 5.5a shows the STEM image of the VS_2 atomic layers. The hexagonal atomic arrangement observed at the edges confirms the 1T structure of VS_2. The EDS in Figure 5.5b shows the presence of only S and V atoms in this region. The EELS spectrum collected along the edge shown in Figure 5.5c further confirms the high quality of the as-synthesized VS_2.

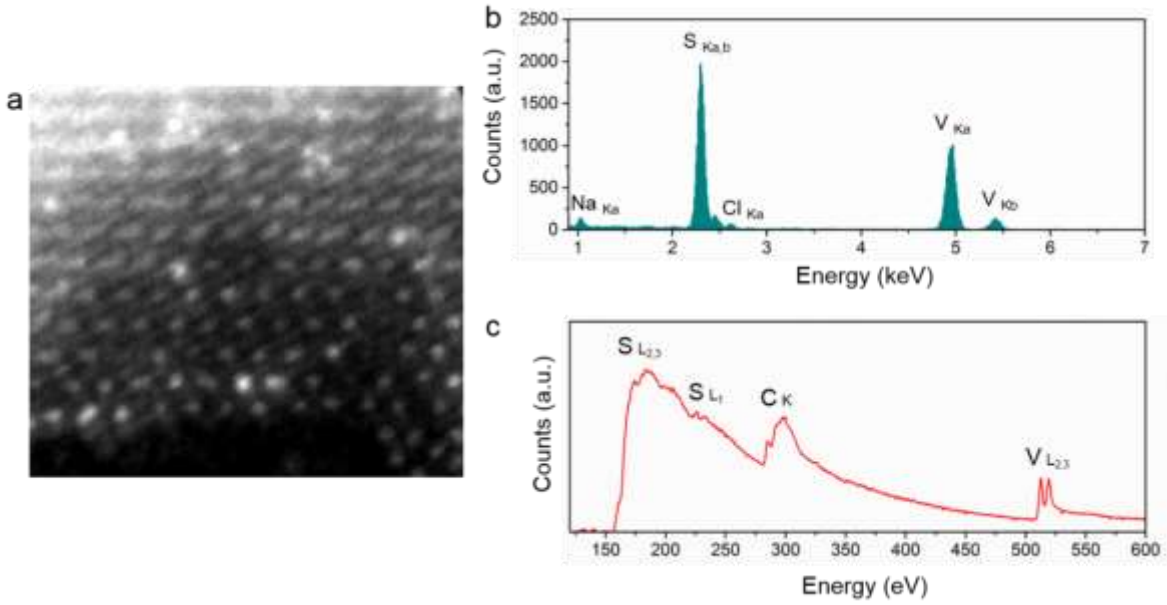

Figure 5.5 Atomic resolution STEM characterization of VS_2. (a) STEM image of the edge thin region of VS_2 atomic layers. (b and c) EDS and EELS spectra of VS_2 atomic layers.

NbS_2 is generally in 2H phase. Figure 5.6a shows the STEM image of a NbS_2 monolayer. Similar to the well-known atomic structure of MoS_2, the 2H phase of NbS_2 is directly identified by the hexagons composed of Nb and S_2 columns with different contrast profile. The clusters at the corners are Nb_xO_y which covers on top of the monolayer. The EDS shown in Figure 5.6b and EELS shown in Figure 5.6c were collected in this region, exhibiting the chemical composition of NbS_2 for the as-synthesized sample.

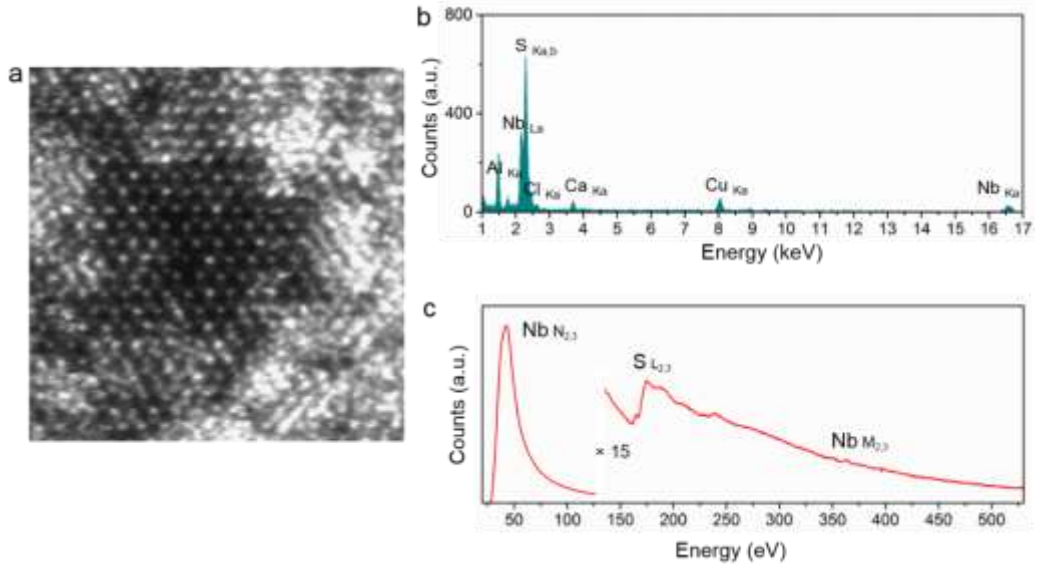

Figure 5.6 Atomic resolution STEM characterization of NbS_2. (a) STEM image of monolayer NbS_2. (b, c) EDS and EELS spectra of NbS_2 monolayer.

5.3 Superconductivity of CVD Grown $NbSe_2$ Monolayers

Superconductivity has been demonstrated in high-quality exfoliated $NbSe_2$ monolayer and in bulk TaS_2 and $MoTe_2$.[35, 37, 38] To examine the quality of the as-grown 2D crystals, the Hall-bar devices were fabricated and measured for studying their transport properties. As an example, the transport results of the as-synthesized monolayer $NbSe_2$ is presented in Figure 5.7a. At a high temperature, it exhibits metallic behavior, with $dR/dT > 0$. When the temperature is reduced to 1.5 K, the superconducting transition starts to emerge. Zero resistance is finally obtained at $T_{c0} = 0.4$ K for the monolayer $NbSe_2$. From the temperature and field dependence of the longitudinal resistance R_{xx} in Figure 5.7b, the phase diagrams of the upper critical field H_{c2}(T) as a function of temperature are obtained, as shown in Figure 5.8a. Accordingly, the coherence lengths of 35 nm is calculated for monolayer $NbSe_2$ using Ginzburg-Landau formula.

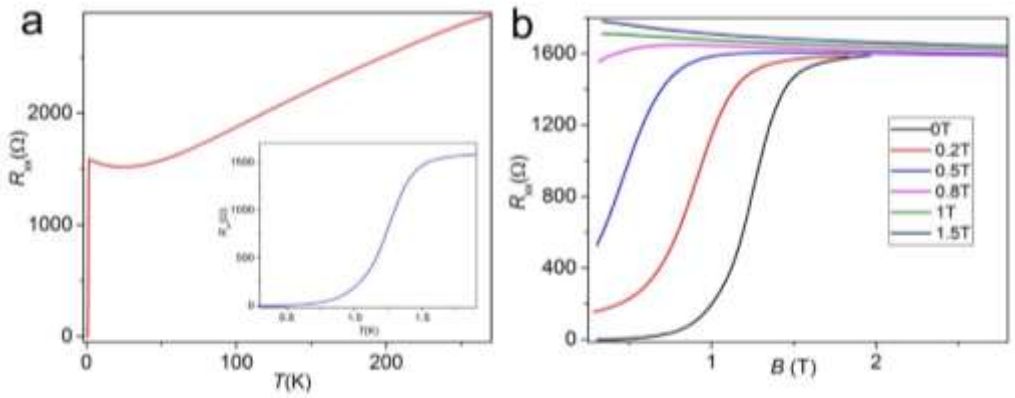

Figure 5.7 Transport measurements of monolayer $NbSe_2$ 2D crystals. (a) Temperature dependence of longitudinal resistance R_{xx} in a zero magnetic field from 300K to 0.26K of the monolayer $NbSe_2$. Inset shows an expanded view of the low-temperature data. (b) Temperature dependence of the longitudinal resistance R_{xx} in different magnetic fields applied perpendicular to the $NbSe_2$ crystal plane.

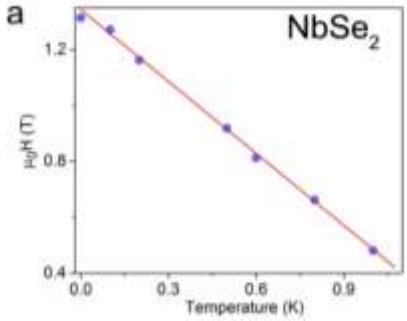

Figure 5.8 Temperature dependence of the upper critical field Hc2 of $NbSe_2$ and $MoTe_2$. The solid red line is the linear fit to Hc2.

5.4 Conclusions

In conclusion, a universal method that is molten salt-assisted chemical vapor deposition method for producing TiX_2, VX_2 and NbX_2 was demonstrated. Optical images of as-produced 2D crystals show large-size of as-produced samples. Moreover, STEM results confirm the atomic structure of as-grown 2D crystals. The superconductivity in monolayer $NbSe_2$ confirms the high quality of as-synthesized 2D TMDs. This method opens up a new route for synthesizing the new 2D TMDs and offers the possibility to study the novel properties in these 2D TMDs.

References

[1] K. S. Novoselov, A. K. Geim, S. V. Morozov, D. Jiang, Y. Zhang, S. V. Dubonos, I. V. Grigorieva, A. A. Firsov, Science 2004, 306, 666.

[2] B. Radisavljevic, A. Kis, Nat Mater 2013, 12, 815.

[3] D. Xiao, G. B. Liu, W. X. Feng, X. D. Xu, W. Yao, Phys Rev Lett 2012, 108.

[4] K. S. Novoselov, D. Jiang, F. Schedin, T. J. Booth, V. V. Khotkevich, S. V. Morozov, A. K. Geim, P Natl Acad Sci USA 2005, 102, 10451.

[5] Q. H. Wang, K. Kalantar-Zadeh, A. Kis, J. N. Coleman, M. S. Strano, Nat Nanotechnol 2012, 7, 699.

[6] M. Chhowalla, H. S. Shin, G. Eda, L. J. Li, K. P. Loh, H. Zhang, Nat Chem 2013, 5, 263.

[7] K. Roy, M. Padmanabhan, S. Goswami, T. P. Sai, G. Ramalingam, S. Raghavan, A. Ghosh, Nat Nanotechnol 2013, 8, 826.

[8] O. Lopez-Sanchez, D. Lembke, M. Kayci, A. Radenovic, A. Kis, Nat Nanotechnol 2013, 8, 497.

[9] A. M. Jones, H. Y. Yu, J. S. Ross, P. Klement, N. J. Ghimire, J. Q. Yan, D. G. Mandrus, W. Yao, X. D. Xu, Nat Phys 2014, 10, 130.

[10] Y. J. Zhan, Z. Liu, S. Najmaei, P. M. Ajayan, J. Lou, Small 2012, 8, 966.

[11] A. M. van der Zande, P. Y. Huang, D. A. Chenet, T. C. Berkelbach, Y. M. You, G. H. Lee, T. F. Heinz, D. R. Reichman, D. A. Muller, J. C. Hone, Nat Mater 2013, 12, 554.

[12] X. Lu, M. I. B. Utama, J. H. Lin, X. Gong, J. Zhang, Y. Y. Zhao, S. T. Pantelides, J. X. Wang, Z. L. Dong, Z. Liu, W. Zhou, Q. H. Xiong, Nano Lett 2014, 14, 2419.

[13] J. C. Park, S. J. Yun, H. Kim, J. H. Park, S. H. Chae, S. J. An, J. G. Kim, S. M. Kim, K. K. Kim, Y. H. Lee, Acs Nano 2015, 9, 6548.

[14] S. Najmaei, Z. Liu, W. Zhou, X. L. Zou, G. Shi, S. D. Lei, B. I. Yakobson, J. C. Idrobo, P. M. Ajayan, J. Lou, Nat Mater 2013, 12, 754.

[15] A. L. Elias, N. Perea-Lopez, A. Castro-Beltran, A. Berkdemir, R. T. Lv, S. M. Feng, A. D. Long, T. Hayashi, Y. A. Kim, M. Endo, H. R. Gutierrez, N. R. Pradhan, L. Balicas, T. E. M. Houk, F. Lopez-Urias, H. Terrones, M. Terrones, Acs Nano 2013, 7, 5235.

[16] X. L. Wang, Y. J. Gong, G. Shi, W. L. Chow, K. Keyshar, G. L. Ye, R. Vajtai, J. Lou, Z. Liu, E. Ringe, B. K. Tay, P. M. Ajayan, Acs Nano 2014, 8, 5125.

[17] J. K. Huang, J. Pu, C. L. Hsu, M. H. Chiu, Z. Y. Juang, Y. H. Chang, W. H. Chang, Y. Iwasa, T. Takenobu, L. J. Li, Acs Nano 2014, 8, 923.

[18] K. J. Koski, Y. Cui, Acs Nano 2013, 7, 3739.

[19] W. X. Zhang, Z. S. Huang, W. L. Zhang, Y. R. Li, Nano Res 2014, 7, 1731.

[20] L. J. Li, E. C. T. O'Farrell, K. P. Loh, G. Eda, B. Ozyilmaz, A. H. C. Neto, Nature 2016, 529, 185.

[21] Y. J. Yu, F. Y. Yang, X. F. Lu, Y. J. Yan, Y. H. Cho, L. G. Ma, X. H. Niu, S. Kim, Y. W. Son, D. L. Feng, S. Y. Li, S. W. Cheong, X. H. Chen, Y. B. Zhang, Nat Nanotechnol 2015, 10, 270.

[22] M. Bovet, D. Popovic, F. Clerc, C. Koitzsch, U. Probst, E. Bucher, H. Berger, D. Naumovic, P. Aebi, Phys Rev B 2004, 69.

[23] T. Sorgel, J. Nuss, U. Wedig, R. K. Kremer, M. Jansen, Mater Res Bull 2006, 41, 987.

[24] Y. D. Ma, Y. Dai, M. Guo, C. W. Niu, Y. T. Zhu, B. B. Huang, Acs Nano 2012, 6, 1695.

[25] A. A. Soluyanov, D. Gresch, Z. J. Wang, Q. S. Wu, M. Troyer, X. Dai, B. A. Bernevig, Nature 2015, 527, 495.

[26] Y. Sun, S. C. Wu, M. N. Ali, C. Felser, B. H. Yan, Phys Rev B 2015, 92.

[27] X. F. Qian, J. W. Liu, L. Fu, J. Li, Science 2014, 346, 1344.

[28] M. M. Biener, J. Biener, C. M. Friend, J Chem Phys 2005, 122.

[29] Y. I. Joe, X. M. Chen, P. Ghaemi, K. D. Finkelstein, G. A. de la Pena, Y. Gan, J. C. T. Lee, S. Yuan, J. Geck, G. J. MacDougall, T. C. Chiang, S. L. Cooper, E. Fradkin, P. Abbamonte, Nat Phys 2014, 10, 421.

[30] E. Morosan, H. W. Zandbergen, B. S. Dennis, J. W. G. Bos, Y. Onose, T. Klimczuk, A. P. Ramirez, N. P. Ong, R. J. Cava, Nat Phys 2006, 2, 544.

[31] J. Khan, C. M. Nolen, D. Teweldebrhan, D. Wickramaratne, R. K. Lake, A. A. Balandin, Appl Phys Lett 2012, 100.

[32] J. Feng, X. Sun, C. Z. Wu, L. L. Peng, C. W. Lin, S. L. Hu, J. L. Yang, Y. Xie, J Am Chem Soc 2011, 133, 17832.

[33] Z. Sofer, D. Sedmidubsky, J. Luxa, D. Bousa, S. Huber, P. Lazar, M. Vesely, M. Pumera, Chemistry 2017.

[34] X. X. Xi, L. Zhao, Z. F. Wang, H. Berger, L. Forro, J. Shan, K. F. Mak, Nat Nanotechnol 2015, 10, 765.

[35] X. X. Xi, Z. F. Wang, W. W. Zhao, J. H. Park, K. T. Law, H. Berger, L. Forro, J. Shan, K. F. Mak, Nat Phys 2016, 12, 139.

[36] S. Nagata, T. Abe, S. Ebisu, Y. Ishihara, K. Tsutsumi, J Phys Chem Solids 1993, 54, 895.

[37] E. Navarro-Moratalla, J. O. Island, S. Manas-Valero, E. Pinilla-Cienfuegos, A. Castellanos-Gomez, J. Quereda, G. Rubio-Bollinger, L. Chirolli, J. A. Silva-Guillen, N. Agrait, G. A. Steele, F. Guinea, H. S. J. van der Zant, E. Coronado, Nat Commun 2016, 7.

[38] Y. P. Qi, P. G. Naumov, M. N. Ali, C. R. Rajamathi, W. Schnelle, O. Barkalov, M. Hanfland, S. C. Wu, C. Shekhar, Y. Sun, V. Suss, M. Schmidt, U. Schwarz, E. Pippel, P. Werner, R. Hillebrand, T. Forster, E. Kampert, S. Parkin, R. J. Cava, C. Felser, B. H. Yan, S. A. Medvedev, Nat Commun 2016, 7.

Chapter 6

$PtSe_2/MoSe_2$ Heterostructure

In this chapter, the vertically stacked $PtSe_2/MoSe_2$ heterostructure will be synthesized by one-step chemical vapor deposition method. Raman and photoluminescence (PL) spectra confirm the stacking structure. The scanning transmission electron microscopy result shows that the Moiré pattern is formed between monolayer $PtSe_2$ and monolayer $MoSe_2$, indicating the epitaxial feature between $PtSe_2$ and $MoSe_2$. Devices fabricated using $PtSe_2/MoSe_2$ show a typical p-n junction, indicating the potential applications of the $PtSe_2/MoSe_2$ heterostructure.

6.1 Introduction

Two dimensional transition metal dichalogenides heterostructures have drawn intensive attention due to their great potential applications. Traditional 2D TMDs heterostructures are often obtained via combining the two or more TMDs with different chemical compositions and properties by sequentially mechanical method. However, the as-obtained heterostructure shows a small overlapped size and its interface contamination is hard to avoid. Chemical vapor deposition (CVD) method and physical vapor deposition (PVD) method have been successfully applied to produce the MoX_2/MX_2 heterostructures (MX_2, where M are the transition metals such as Mo or W, and X is S, or Se) via one-step or two-step vdW epitaxy process.[1-9] However, the common characteristics of the as-produced heterostructures are based on the feasibility that the monolayer TMDs single crystals can be prepared easily in a separated CVD process. More importantly, the similar lattice structures and constants offer the opportunity to form the MoX_2/MX_2 heterostructure with commensurate superlattice. Recently, twinned growth WS_2/ReS_2 vertical heterostructure has been reported,[6] which opens up a new route to synthesize heterostructure with different crystal structure. However, the method has the similar characteristic as discussed above since the monolayer ReS_2 single crystal can be synthesized easily. Moreover, alloyed foils as the growth substrate need to be formed at first. So far, synthesis of the heterostrurctures between MX_2 and group-10 TMDs (for example PtS_2, $PtSe_2$), cannot be realized due to the low chemical reactivity of Pt and Pd and their different crystal structures from the MX_2.

Group-10 TMDs have been demonstrated transition from a semimetal in bulk to a semiconductor in monolayer with the band gap increasing from 0 eV to 1.6 eV, [10] which is considered to be a moderate catalyst for hydrogen evolution reaction.[11] In addition, the theoretical prediction and experiment confirmed that high mobility and good air stability make them as promising candidates in the applications of field effect transistors (FETs).[12] Synthesis of group-10 TMDs together with the heterostructure combined with MX_2 shows the great opportunities to enrich their intrinsic properties and broad their applications.

However, so far, it is still challenging. In this chapter, one-step CVD method has been proposed to synthesize the $PtSe_2/MoSe_2$ vertical heterostructure.

6.2 Results and Discussion

6.2.1 The structure and morphology characterization of $PtSe_2/MoSe_2$

In order to synthesize $PtSe_2/MoSe_2$ heterostructure, the $PtCl_2$, MoO_3 and Se powder were used as the Pt, Mo and Se sources, respectively. Figure 6.1a shows the reaction system used to prepare the $PtSe_2$ and $MoSe_2/PtSe_2$ vertically stacked heterostructure via one-step CVD method. Figure 6.1b shows the atomic crystal structure of $MoSe_2/PtSe_2$ vertical heterostructure. The 1T phase of $PtSe_2$ crystal structure is different from the 2H phase of $MoSe_2$. Figure 6.1c and 6.1d show the $PtSe_2/MoSe_2$ vertical heterostructure with the rectangular and hexagonal shapes of the $PtSe_2$ on the $MoSe_2$ monolayer, respectively. The size of monolayer $PtSe_2$ single crystal is ~ 40 μm in Figure 6.1c and ~ 30 μm in Figure 6.1d, respectively. The area of the vertical heterojunction is about 1000 μm^2, which is larger than the previous reports. The comparison between our results with the reported ones is shown in Figure 6.1e.[1-8] As a comparison, the pure $PtSe_2$ was synthesized by CVD method, however, only thick flakes could be obtained. The corresponding optical images are shown in Figure 6.2. The AFM measurement was carried out to examine the thickness of as-synthesized $PtSe_2/MoSe_2$ and $PtSe_2$, as shown in Figure 6.3. The formation of monolayer $PtSe_2$ on monolayer $MoSe_2$ vertical heteostructure and few layer $PtSe_2$ obtained by the similar CVD method indicate that the epitaxy growth plays the key role on the preparation of monolayer $PtSe_2$.

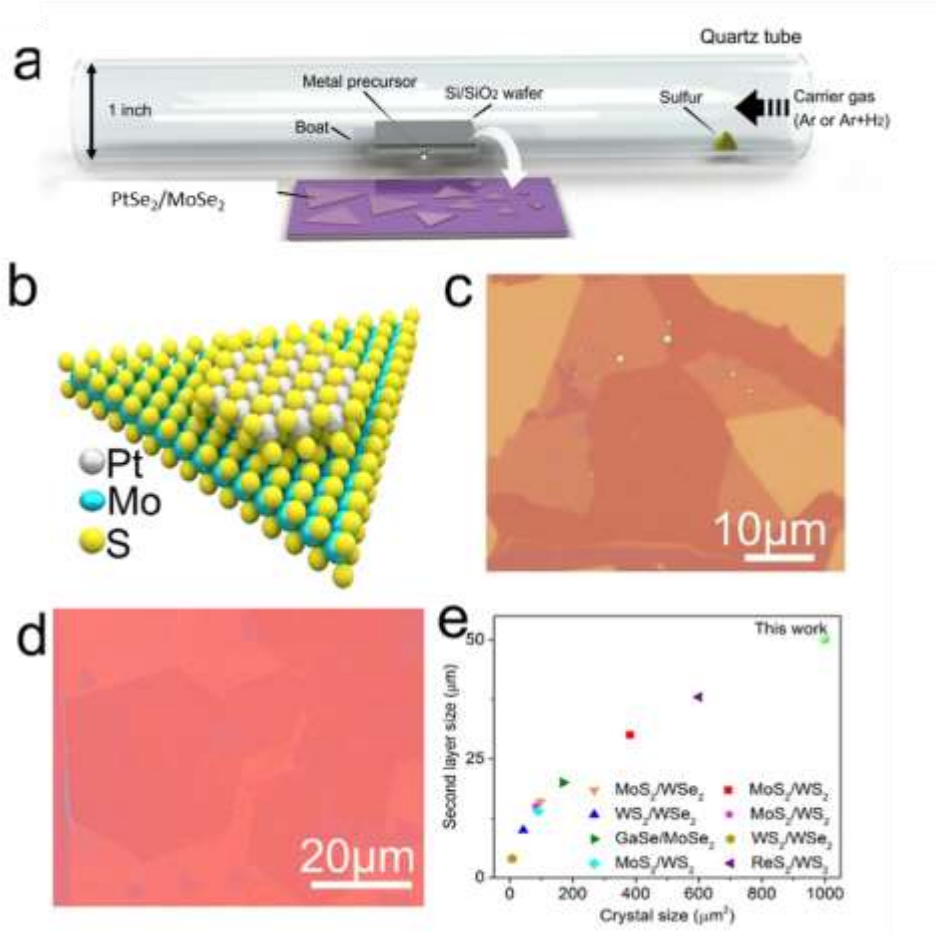

Figure 6.1 Reaction system and optical images of $PtSe_2/MoSe_2$. (a) The reaction system was used to synthesize $PtSe_2$ and $PtSe_2/MoSe_2$ vertical heterostructure. (b) The atomic crystal structure of $PtSe_2/MoSe_2$. (c, d) Optical images of as-synthesized $PtSe_2/MoSe_2$ heterostructure. (e) Comparison of the as-synthesized heterostructure via one or two CVD steps or PVD method.

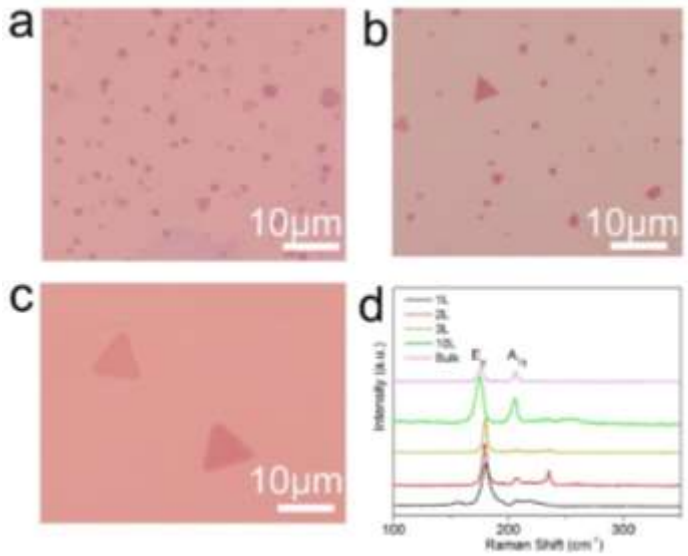

Figure 6.2 The spectra and optoelectronic characterization of $PtSe_2/MoSe_2$

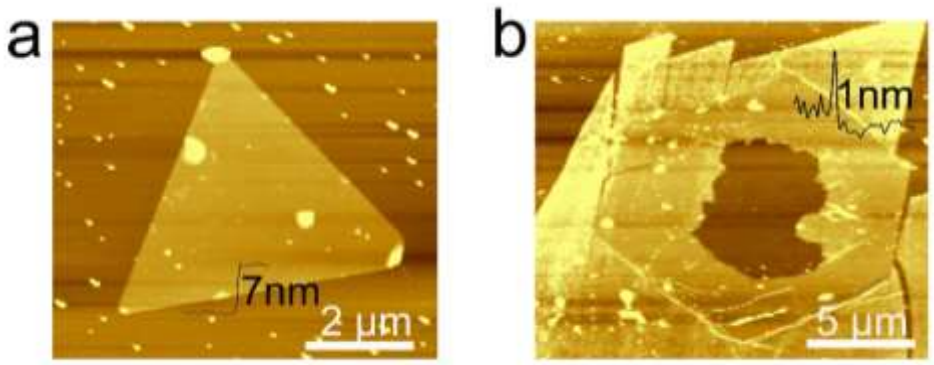

Figure 6.3. (a) Few layer $PtSe_2$ was synthesized without adding Mo sources. (b) The thickness of $PtSe_2$ is about 1 nm, indicating the as-synthesized $PtSe_2$ is monolayer.

6.2.2 Raman and PL characterizations of $PtSe_2/MoSe_2$

Raman spectroscopy was further used to characterize the structure and quality of as synthesized $PtSe_2/MoSe_2$ vertical heterojunction. Figure 6.4a shows Raman spectrum in the point 1 of the heterostructure (inset is the optical image of the vertical heterostructure). The Raman peak located at 240 cm^{-1} indicating the crystal is pure $MoSe_2$.[13] Figure 6.4b shows the Raman spectrum in the point 2. The Raman peaks locate at the 175 cm^{-1}, 205

cm^{-1} and 240 cm^{-1}, which are assigned to the E_g mode, A_{1g} mode of $PtSe_2$[14] and A_{1g} mode of $MoSe_2$, respectively. This indicates that the vertical heterojunction is formed between $PtSe_2$ and $MoSe_2$. Note that, a new Raman peak appears at 60 cm^{-1}, suggesting the strong coupling between $MoSe_2$ and $PtSe_2$. Figure 6.4d shows PL spectra of point 1 and point 2, however, almost no PL signal appears in the point 2 due to the charge transfer between the monolayer $MoSe_2$ and $PtSe_2$. This is because that the monolayer $MoSe_2$ is a direct band gap semiconductor and the monolayer $PtSe_2$ is an indirect band semiconductor.[15]

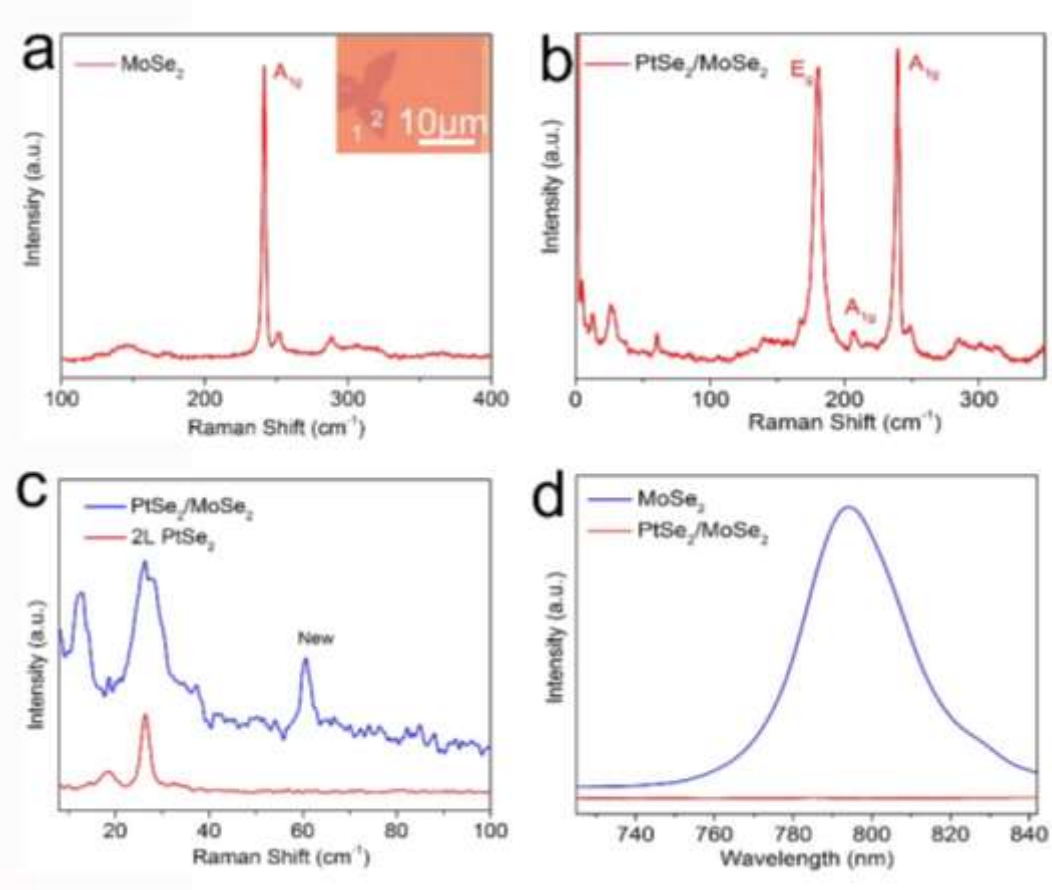

Figure 6.4 (a) Raman spectrum of monolayer $MoSe_2$ in the position 1 of the heterostructure (inset showing optical image of the vertical heterostructure). (b) Raman spectrum of $PtSe_2/MoSe_2$ in the position 2 of the heterostructure. (c) Raman spectra of $PtSe_2$ and $PtSe_2/MoSe_2$. (d) PL of pure $MoSe_2$ and $PtSe_2/MoSe_2$.

Raman and PL mapping were further measured to study the homogeneousness of as-synthesized heterostructure. Raman mappings of $PtSe_2$ (Figure 6.5a) and $MoSe_2$ (Figure

6.5b) show that no defect can be detected in the samples, indicating the uniform homogeneousness of as-synthesized $PtSe_2/MoSe_2$. Figure 6.5c and Figure 6.5d display the PL mapping of $PtSe_2$ and $MoSe_2$, respectively.

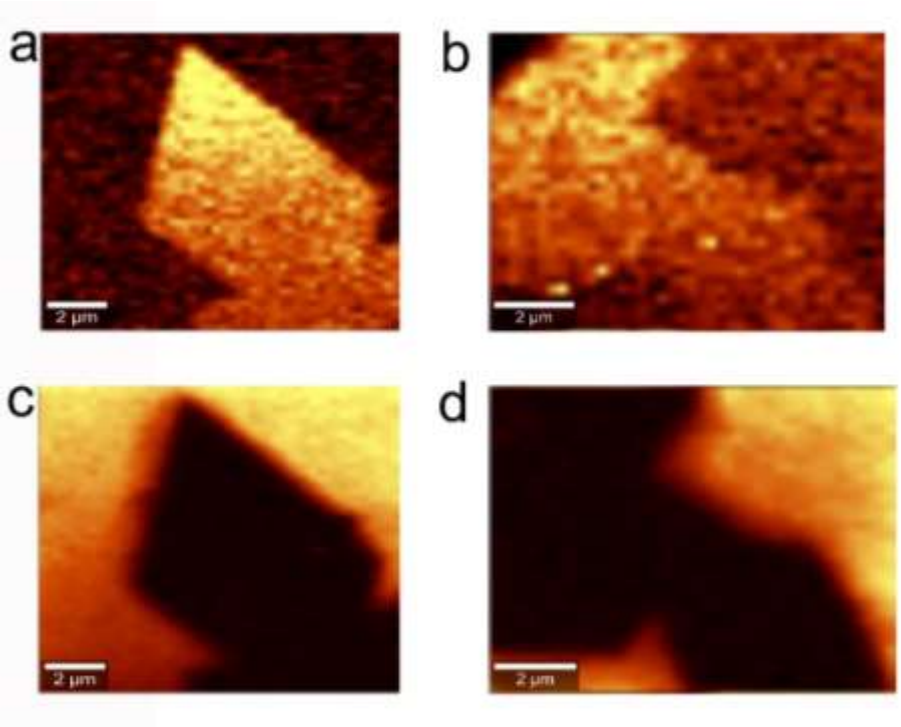

Figure 6.5 (a) Raman mapping of $PtSe_2$. (b) Raman mapping of $MoSe_2$. (c) PL mapping of $PtSe_2$. (d), PL mapping of $MoSe_2$.

6.2.3 XPS characterization of $PtSe_2/MoSe_2$

X-ray photoelectron spectroscopy (XPS) was further employed to check the element composition and the thickness dependent-spectra of as-synthesized $PtSe_2$. The (Pt and Mo): S atomic ration is closed to 1:2, indicating that the vertical heterjunction is stoichiometric. Furthermore, a 400 meV up-lift in the peak of the Mo 3d core level of $MoSe_2$ shows as compared with that of $PtSe_2/MoSe_2$ in the Figure 6.6a, illustrates a positive net charge on the $MoSe_2$ bottom layer. A 650 meV shifts in Pt 4f core level between pure $PtSe_2$ and $PtSe_2/MoSe_2$ in the Figure 6.6b, corresponds to a negative net charge from $PtSe_2$. All these evidences indicate the strong coupling between $MoSe_2$ and $PtSe_2$. The work function of

$PtSe_2$ and $MoSe_2$ is shown in Figure 6.6c. All these endow the $PtSe_2/MoSe_2$ heterostructure as an atomically thin capacitor with a potential up to 1050 meV.

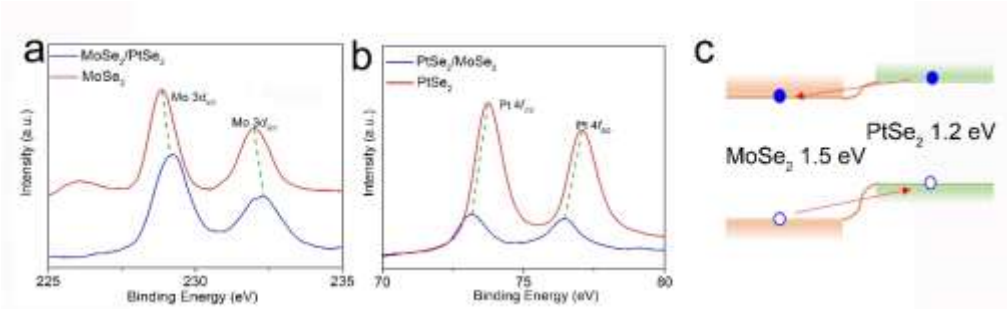

Figure 6.6 XPS of $PtSe_2/MoSe_2$. (a) XPS of Mo *3d*. (b) XPS of Pt *4f*. (c) The band structure of $PtSe_2/MoSe_2$.

6.2.4 STEM characterization of $PtSe_2/MoSe_2$

In order to study the vertically epitaxial behavior of the as-synthesized $PtSe_2/MoSe_2$ heterostructure, annular dark-field (ADF) imaging in an aberration-corrected scanning transmission electron microscopy (STEM) is performed to investigate its atomic structure. Figure 6.7a shows the experimental atomic-resolution ADF-STEM image of $PtSe_2/MoSe_2$. The periodic Moiré patterns was clearly observed along the basal plane of the heterostructure, which is caused by the interference from the lattice of monolayer $PtSe_2$ and $MoSe_2$. Fast Fourier transformation (FFT) of the $PtSe_2/MoSe_2$ is shown in the inset of Figure 6.7a. Two different sets of diffraction patterns are identified, and the corresponding lattice constants of 0.191 nm and 0.174 nm correspond to the lattice of $PtSe_2$ and $MoSe_2$, respectively, indicating that the as-synthesized $PtSe_2$ and $MoSe_2$ are single crystal. Moreover, the lattice orientations of the two monolayers are well aligned to each other, which is a representative evidence for vertically epitaxial growth. Although the fast Fourier transform (FFT, inset in Figure 6.7a) do not show the superlattice spots due to its large lattice spacing which is buried inside the central FFT pattern, the periodicity of the Moiré pattern can be directly measured in the atomic resolution image by filtering out the

diffraction spots from $PtSe_2$ and $MoSe_2$ which was estimated to be 2.45 nm. Such large supercell indicates the highly epitaxial feature due to the coupling growth between the two materials. Figure 6.7b and 6.7c shows the inverse FFT image of Figure 6.7a, which distinguishes the atomic structure of $PtSe_2$ and $MoSe_2$ by selectively filtering their characteristic diffraction spots, respectively. This confirms the 1T and 2H phase for $PtSe_2$ and $MoSe_2$ monolayer, respectively.

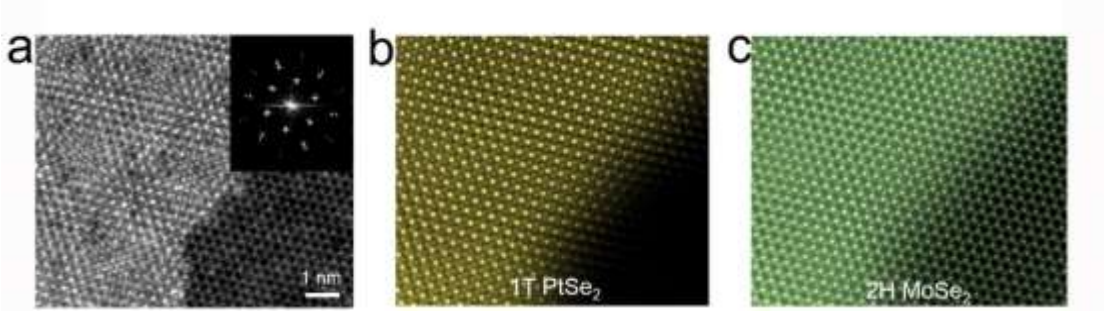

Figure 6.7 Atomic structure of the vertically stacked $PtSe_2/MoSe_2$ heterostructure and lateral boundary. (a) Experimental atomic-resolution ADF-STEM image of $PtSe_2/MoSe_2$, showing the periodic Moiré pattern where the monolayer $PtSe_2$ stacks on the top of monolayer $MoSe_2$. Inset showing the FFT pattern obtained from a, in which the lattice constants of 0.191 nm and 0.174 nm are corresponding to the lattice of $PtSe_2$ and $MoSe_2$, respectively. (b, c) Inverse FFT image of (a) by selectively filtering out the $PtSe_2$ (b) and $MoSe_2$ (c) lattice information in the FFT pattern, respectively.

Figure 6.8a shows a low magnified ADF-STEM image of $PtSe_2/MoSe_2$ heterostructure with a lateral boundary between the bilayer $PtSe_2/MoSe_2$ heterostructure and bilayer $MoSe_2$. Such a structure can be considered as a grain boundary between $PtSe_2$ and $MoSe_2$ monolayer on $MoSe_2$ substrate. Figure 6.8b and 6.8c show the zoom-in images of the areas highlighted in Figure 6.8a. It is found that the two different monolayers grow over each other instead of forming an atomically sharp lateral boundary. The former region of the boundary shows an abrupt contrast change from the $PtSe_2$ lattice to $MoSe_2$ (Figure 6.8b). However, a very narrow region with enhanced contrast along the boundary can be observed, which is attributed to the overlapping edge atoms from the two monolayers rather than direct chemical bonding, i.e., atomically sharp interconnected boundary. As shown in later regions along the lateral boundary, the overlapping regions become wider (Figure 6.8c),

confirming the overlapping feature in the lateral boundary. The preference of forming overlapping lateral boundary between these two materials may originate from their large lattice mismatch, consistent with their strong coupling vertically epitaxial growth.

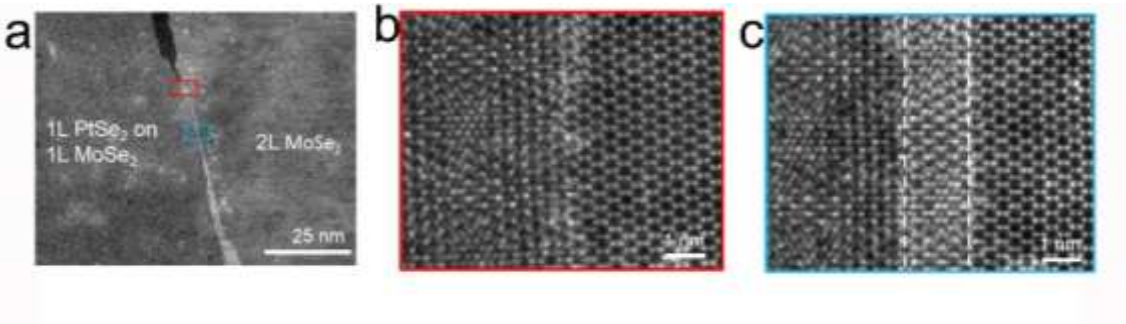

Figure 6.8 (a) Low-magnification ADF-STEM image of a lateral boundary between monolayer $PtSe_2$ and monolayer $MoSe_2$ on top of another layer of $MoSe_2$. (b, c) Zoom-in images with atomic resolution of the regions highlighted by red (b) and blue (c) in (a), illustrates the overlapping feature between the two monolayers.

6.2.5 Applications of $PtSe_2/MoSe_2$

In order to explore the electrical properties of the as-synthesized $PtSe_2/MoSe_2$, the vertical heterojunction was used to fabricate field-effect transistor devices. The Cr/Au (~ 5 nm and 50 nm, respectively) contacts as the drain and source were thermally evaporated onto the surface defined by electron beam lithography (EBL). Figure 6.9a shows optical image of the device. The output characteristic of as-fabricated devices of monolayer $PtSe_2$ is shown in Figure 6.8b, where the I_d reaches about 150 nA under the top gate 50 V. Figure 6.9c shows the transport characteristic of the monolayer $PtSe_2$. It should be noted that the monolayer $PtSe_2$ exhibits a p-ype semiconducting behavior, similar to the previous reported result.[16] As the monolayer $MoSe_2$ is a n-type semiconductor, the p-n junction forms in the heterojunction between $PtSe_2$ and $MoSe_2$ forms. The electrical properties of the p ($PtSe_2$)–n ($MoSe_2$) heterojunction were measured using electrodes 1 and 3 as shown in Figure 6.9 a. The output curve (I_d-V_d) is gate-dependent and clearly shows current rectification behavior (Figure 6.9d), indicating that a good p-n diode is formed across the heterojunction.

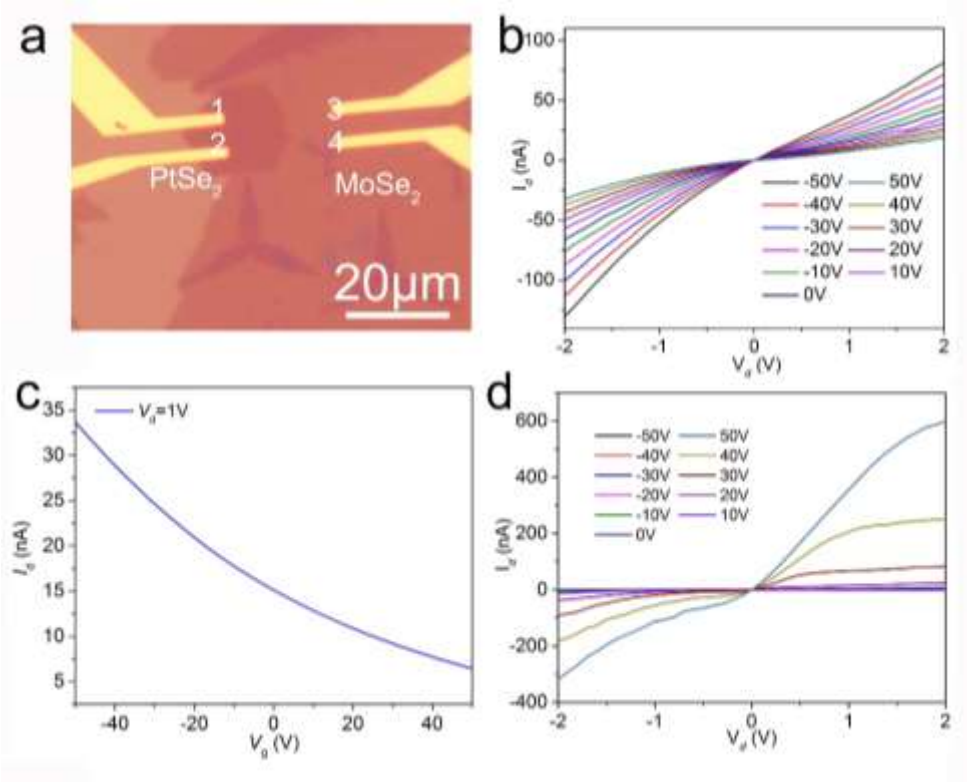

Figure 6.9 Transport of the vertical heterostructures. (a) Optical image of the FET device. (b) Output characteristics of monolayer $PtSe_2$, showing large Id under different applied voltage. (c) The transport characteristic of $PtSe_2$, indicating that monolayer $PtSe_2$ is a p type semiconductor. (d) ds-Vds curves across the p ($PtSe_2$)/n ($MoSe_2$) heterojunction (measured using electrodes 1 and 3) at different back-gate voltages, showing a typical p-n junction.

6.3 Conclusions

The $PtSe_2/MoSe_2$ vertical heterojunction was synthesized via one-step CVD method. The strong coupling epitaxial growth behavior plays the key role for the formation of $PtSe_2/MoSe_2$ heterostructure. The large-size monolayer $PtSe_2$ single crystal was obtained for the first time. Raman spectra, XPS and STEM results confirm the atomic structure of PtSe2/$MoSe_2$ heterostructure. The strong coupling between $PtSe_2$ and $MoSe_2$ offers the opportunity to study the interlayer charge transfer. More importantly, this strategy represents a facile approach to synthesize the vertical heterostructure between group 10 TMDs and MX_2.

References

[1] M. Y. Li, Y. M. Shi, C. C. Cheng, L. S. Lu, Y. C. Lin, H. L. Tang, M. L. Tsai, C. W. Chu, K. H. Wei, J. H. He, W. H. Chang, K. Suenaga, L. J. Li, Science 2015, 349, 524.

[2] K. Chen, X. Wan, J. X. Wen, W. G. Xie, Z. W. Kang, X. L. Zeng, H. J. Chen, J. B. Xu, Acs Nano 2015, 9, 9868.

[3] K. Chen, X. Wan, W. G. Xie, J. X. Wen, Z. W. Kang, X. L. Zeng, H. J. Chen, J. B. Xu, Adv Mater 2015, 27, 6431.

[4] X. F. Li, M. W. Lin, J. H. Lin, B. Huang, A. A. Puretzky, C. Ma, K. Wang, W. Zhou, S. T. Pantelides, M. F. Chi, I. Kravchenko, J. Fowlkes, C. M. Rouleau, D. B. Geohegan, K. Xiao, Sci Adv 2016, 2.

[5] Y. D. Yoo, Z. P. Degregorio, J. E. Johns, J Am Chem Soc 2015, 137, 14281.

[6] T. Zhang, B. Jiang, Z. Xu, R. G. Mendes, Y. Xiao, L. F. Chen, L. W. Fang, T. Gemming, S. L. Chen, M. H. Rummeli, L. Fu, Nat Commun 2016, 7.

[7] Y. J. Gong, J. H. Lin, X. L. Wang, G. Shi, S. D. Lei, Z. Lin, X. L. Zou, G. L. Ye, R. Vajtai, B. I. Yakobson, H. Terrones, M. Terrones, B. K. Tay, J. Lou, S. T. Pantelides, Z. Liu, W. Zhou, P. M. Ajayan, Nat Mater 2014, 13, 1135.

[8] X. D. Duan, C. Wang, J. C. Shaw, R. Cheng, Y. Chen, H. L. Li, X. P. Wu, Y. Tang, Q. L. Zhang, A. L. Pan, J. H. Jiang, R. Q. Yu, Y. Huang, X. F. Duan, Nat Nanotechnol 2014, 9, 1024.

[9] C. M. Huang, S. F. Wu, A. M. Sanchez, J. J. P. Peters, R. Beanland, J. S. Ross, P. Rivera, W. Yao, D. H. Cobden, X. D. Xu, Nat Mater 2014, 13, 1096.

[10] P. F. Li, L. Li, X. C. Zeng, J Mater Chem C 2016, 4, 3106.

[11] X. Y. Chia, A. Adriano, P. Lazar, Z. Sofer, J. Luxa, M. Pumera, Adv Funct Mater 2016, 26, 4306.

[12] Y. D. Zhao, J. S. Qiao, Z. H. Yu, P. Yu, K. Xu, S. P. Lau, W. Zhou, Z. Liu, X. R. Wang, W. Ji, Y. Chai, Adv Mater 2017, 29.

[13] X. L. Wang, Y. J. Gong, G. Shi, W. L. Chow, K. Keyshar, G. L. Ye, R. Vajtai, J. Lou, Z. Liu, E. Ringe, B. K. Tay, P. M. Ajayan, Acs Nano 2014, 8, 5125.

[14] M. O'Brien, N. McEvoy, C. Motta, J. Y. Zheng, N. C. Berner, J. Kotakoski, K. Elibol, T. J. Pennycook, J. C. Meyer, C. Yim, M. Abid, T. Hallam, J. F. Donegan, S. Sanvito, G. S. Duesberg, 2d Mater 2016, 3.

[15] W. Yao, E. Y. Wang, H. Q. Huang, K. Deng, M. Z. Yan, K. N. Zhang, K. Miyamoto, T. Okuda, L. F. Li, Y. L. Wang, H. J. Gao, C. X. Liu, W. H. Duan, S. Y. Zhou, Nat Commun 2017, 8.

[16] C. Yim, K. Lee, N. McEvoy, M. O'Brien, S. Riazimehr, N. C. Berner, C. P. Cullen, J. Kotakoski, J. C. Meyer, M. C. Lemme, G. S. Duesberg, Acs Nano 2016, 10, 9550.

Chapter 7

High Quality of α-In_2Se_3 Monolayer*

In this part, the synthesis of high-quality monolayer α-In_2Se_3 using physical vapor deposition (PVD) method will be introduced. The quality of the In_2Se_3 atomic layers has been confirmed by complementary characterization technologies such as Raman/photoluminescence (PL) spectroscopies and atomic force microscope (AFM). The atomically resolved images have been obtained by the annular dark field scanning transmission electron microscope (ADF-STEM). The field-effect transistors (FETs) have been fabricated using the atomically layered In_2Se_3 and exhibit excellent property, indicating the In_2Se_3 as a potential candidate for the optoelectronic and photosensitive device applications.

*This chapter published substantially as: Controlled Synthesis of High-quality Monolayered α-In_2Se_3 via Physical Vapor Deposition, Zhou jiadong, etc. (*Nano Letters*, 2015, 15, 6400)

7.1 Introduction

Two-dimensional (2D) materials have attracted intensive attention due to their excellent property and considered as the potential candidates for next generation electronic and optoelectronic applications.[1-3] Recently, graphene-like 2D materials have been revisited due to their unique properties when their thickness is thinned down to few layers or monolayer. For instance, 2D TMDs monolayers show high on/off ratio ($10^3 \sim 10^8$) and high mobility (1 ~ 100 cm^2/ Vs),[4,5] which can be used for the ultra-low-power electronics. Moreover, TMDs monolayers have also been used for valleytronics, nonlinear optics, optical sensors and high-effective catalyst for hydrogen evolution.[6-7] Although many efforts have been devoted to study the 2D TMDs, the non-transition metal chalcogenides such as Bi_2Se_3, Bi_2Te_3, Ga_xS_y, In_xSe_y, and Sb_2Te_3, showing the exciting physics such as topological insulating effect and potential applications in catalysis and sensors, have not been studied.[8-11] This is attributed to the difficulty in synthesizing these 2D materials. Especially, existence of different phases impedes researchers to produce them. For example, there are five known crystal forms (α, β, γ, δ and *k*) in In_2Se_3 at different temperature.[12] Furthermore, demonstrating their phase is still a big challenge.[12] However, all these phases also offer the interesting in the In_2Se_3. Among the five phases, the α phase In_2Se_3 is a layered 2D material. The thickness of one layer is of ~ 1 nm.[13-14] The phase transition from α-In_2Se_3 to β-In_2Se_3 indicates the fascinating physics in this system. Synthesis of high-quality α-In_2Se_3 atomic layers will offer the possibility to study such transition. Furthermore, In_2Se_3 flakes and nanowire arrays show excellent optoelectronic properties. α-In_2Se_3 is a direct-band gap semiconductor with the band gap of ~ 1.3eV, indicating α-In_2Se_3 can be used in optoelectronics, nonvolatile phase change memory, especially in the field of photodetector and FETs. [15-18]

In order to synthesize the In_2Se_3, the direct sputtering deposition has been used. However, only the polycrystalline In_2Se_3 films were obtained. Recently, In_2Se_3 nanosheets have been prepared by micromechanical exfoliation method. However, only small size and thick In_2Se_3 flakes were obtained. PVD method has been employed to synthesize In_2Se_3 nanowire arrays for visible-light photodetectors and produce GaSe.[15, 20, 21] Very recently,

Lin et al. reported that In_2Se_3 layers can be obtained on mica and graphene under low pressure,[18] This indicates that the synthesis of large-size In_2Se_3 monolayer can be achieved by PVD method. However, In_2Se_3 on mica needs to be transferred onto the silica substrate for device fabrication. More importantly, regular monolayer In_2Se_3 and atomic structure of monolayered In_2Se_3 have not been observed. Synthesis of monolayer In_2Se_3 remains a big challenge due to the decomposition of In_2Se_3 powders under low pressure at high temperature.[22] Based on the discussion above, in this thesis, the In_2Se_3 on silicon substrate under atmospheric pressure was synthesized directly.

7.2 Results and Discussion

7.2.1 Optical images of In_2Se_3

The monolayer and few layer In_2Se_3 crystals were produced by PVD method. Briefly, the Ar was used as the carrier gas and the growth temperature was set at 850 °C. Especially, the thickness of In_2Se_3 can be controlled by controlling the growth time. Figure 7.1 shows the reaction system used to prepare the In_2Se_3 atomic layers. Figure 7.2a shows a triangular In_2Se_3 monolayer with lateral size of ~ 4 μm when using the growth time of 5 min. Furthermore, large In_2Se_3 atomic layers with lateral size up to 10 μm is obtained upon increasing the growth time to 10 min, as shown in Figure 7.2b. However, thickness of In_2Se_3 increases with increasing growth time to 15 min, as shown in Figure 7.2c. Meanwhile, In_2Se_3 with different morphologies and thickness can be obtained by controlling the growth condition, as shown in Figure 7.3. AFM was used to check the thickness of In_2Se_3. AFM images and height are shown in Figure 7.3, indicating that the as-synthesized In_2Se_3 is monolayer.

Figure 7.1 Schematic diagram of the PVD system used for the preparation of In_2Se_3

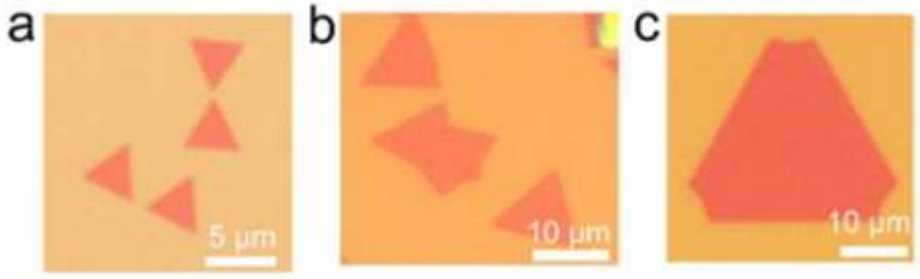

Figure 7.2 Optical images of In_2Se_3. (a-c) Optical images of In_2Se_3 with different growth time.

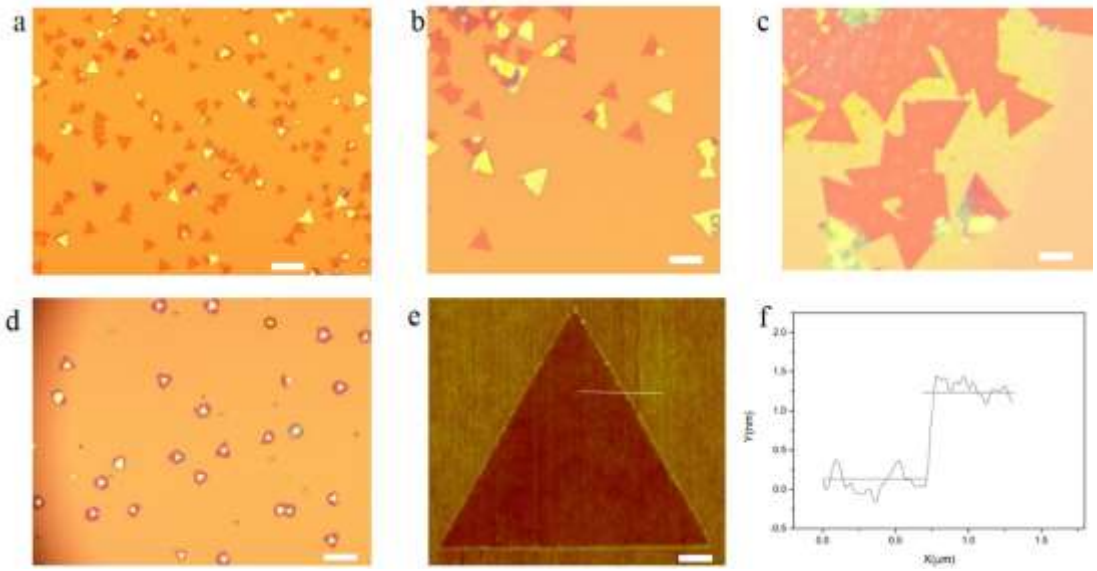

Figure 7.3 In_2Se_3 with different growth time. (a) 5 min. (b) 10 min. (c) 12 min. (d) 15 min. (a-c) Scale bar: 10μm, 10μm, 10μm, and 20 μm, respectively. (e-f) The AFM image and thickness of In_2Se_3 monolayer. Scale bar: 0.2 μm.

7.2.2 RM and PL characterizations of In_2Se_3

Raman spectroscopy and photoluminescence (PL) were used to examine the quality of the monolayer and few-layer In_2Se_3. The 532 nm laser was used as the incident light source. Figure 7.4a shows Raman spectra of In_2Se_3 with different thickness ranging from monolayer to bulk. The inserted In_2Se_3 was used to measure Raman and PL mapping. It is notable that the Raman peaks located at 237 and 252 cm^{-1} are observed, corresponding to

the vibration modes originating from the A_1 symmetry and Se_8 rings,[23] respectively. This result is in good agreement with the previous reported results on α-In_2Se_3,[24] demonstrating the as-synthesized In_2Se_3 is α phase. For bulk In_2Se_3, the Raman peaks locate at 180 and 192 cm^{-1}, showing a little down-shift compared with those of the few layer In_2Se_3. Similar shift has also been observed in other 2D materials such as MoS_2, WS_2 and so on.[23, 25] Raman mapping of monolayer In_2Se_3 is shown in Figure 7.4c, demonstrating a high homogeneousness of as-produced In_2Se_3. The PL spectra of 1L, 2L, 4L and bulk In_2Se_3, are shown in Figure 7.4b, respectively. It is notable that the position of the monolayer In_2Se_3 locates at ~ 801 nm, revealing that the optical band gap of In_2Se_3 is ~ 1.55 eV, which is for the first time observed in monolayer In_2Se_3. Similar to previous reports on 2D TMDs, there is no any PL signal for the bulk In_2Se_3 at room temperature (Figure 7.4b). Compared with the monolayer, the PL intensity of few layer In_2Se_3 significantly decreases with the thickness increases. This is probably due to quantum size confinement and defects in In_2Se_3. Furthermore, because of complicated structure of In_2Se_3, it is very difficult to determine the defect in monolayer of few layer In_2Se_3 from STEM image.[26] PL mapping of monolayer In_2Se_3 (Figure 7.4d) shows a low density of the defects in In_2Se_3.

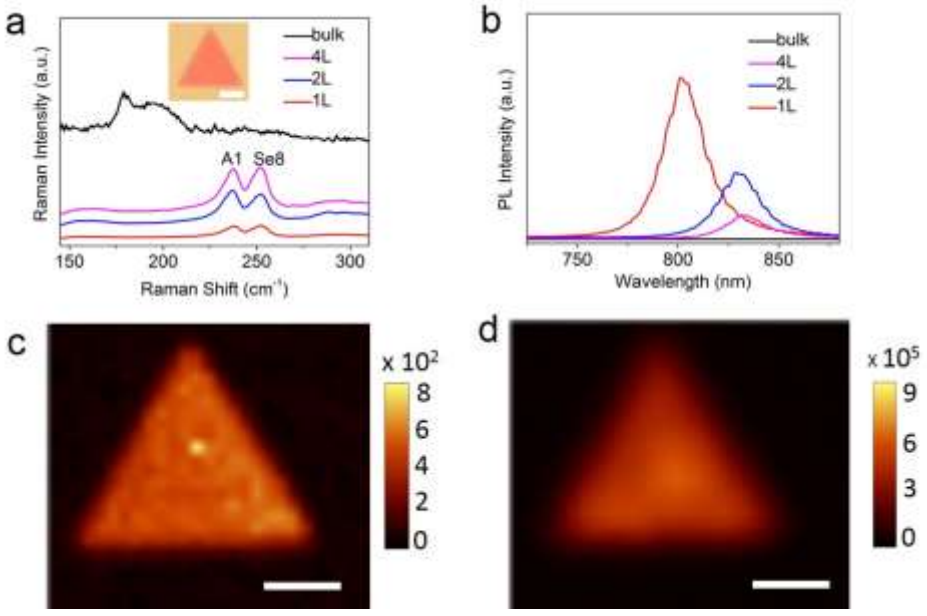

Figure 7.4 Raman and PL spectra of In_2Se_3. (a) layer-dependent Raman spectra of In_2Se_3. (b) PL of In_2Se_3 from 1 to 4 layers. (c and d) Raman and PL mapping of monolayer In_2Se_3, respectively.

7.2.3 STEM characterization of In_2Se_3

TEM/STEM techniques were further used to study atomic structure of In_2Se_3. Figure 7.5a shows the low-magnitude TEM image of In_2Se_3 flakes on the TEM grid. From the inset SAED pattern of the monolayer In_2Se_3 in Figure 7.5a, it can be seen that the six-fold rotational symmetric diffraction pattern was obtained, indicating the hexagonal structure of In_2Se_3. Figure 7.5b and Figure 7.5c show In_2Se_3 flakes with triangular and hexagonal shapes, respectively. The previous results reported that there are two different models of crystal structure of In_2Se_3, namely the wurtzite sequence and the bonding structure of Se-In-Se-In-Se five layer in the tetrahedral structure.[13, 27, 28] The atomically resolved STEM imaging of monolayer In_2Se_3 is shown in Figure 7.6a with a hexagonal honeycomb structure. The corresponding Fast Fourier Transform (FFT) pattern is inserted in Figure 7.6a. The dotted yellow line in Figure 7.6a is used to identify the possible arrangement of In and Se atoms. Figure 7.6b shows the zoomed image of the highlighted area. The top-view and side-view models of In_2Se_3 monolayer are shown in Figure 7.6b. Lines 1 and 2 correspond to the column of the Se-In-Se and Se-In, respectively. It is notable that the two sites in line 2 are darker that the 3 overlapped atoms in line 1. Figure 7.6a shows a few much brighter sites (see yellow arrows), contributable to the single In atom which is produced by the decomposition of In_2Se_3 at high temperature (Figure 7.7). Figure 7.6c shows the bilayer crystal. It shows that the atomic shape interface forms between monolayered In_2Se_3 in the left and bi-layered in the right. Inset is the FFT pattern. Similar to Figure 7.6a, the highlighted region in Figure 7.6c is given in Figure 7.6d. The typical AB stacking from the top-view mode along the [001] direction can be observed. The bright sites in lines 1 and 2 resulting from the sequence of Se-In-Se-In-Se and other sites originating from the sequence of In-Se-In and Se-In between lines 1 and 2 can be found in Figure 7.6d.[29]

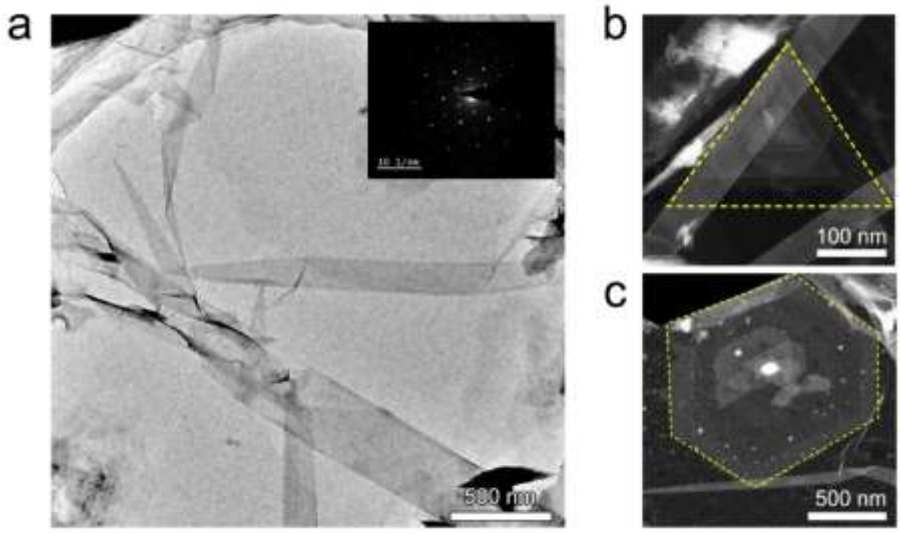

Figure 7.5 TEM imaging of In_2Se_3. (a) Monolayer In_2Se_3 film (Inset: the SAED patterns of monolayer In_2Se_3). (b-c) Low magnification TEM imaging of In_2Se_3 (triangular and hexagonal shapes). The indium particles are produced during the growth, as indicated by white dots in c.

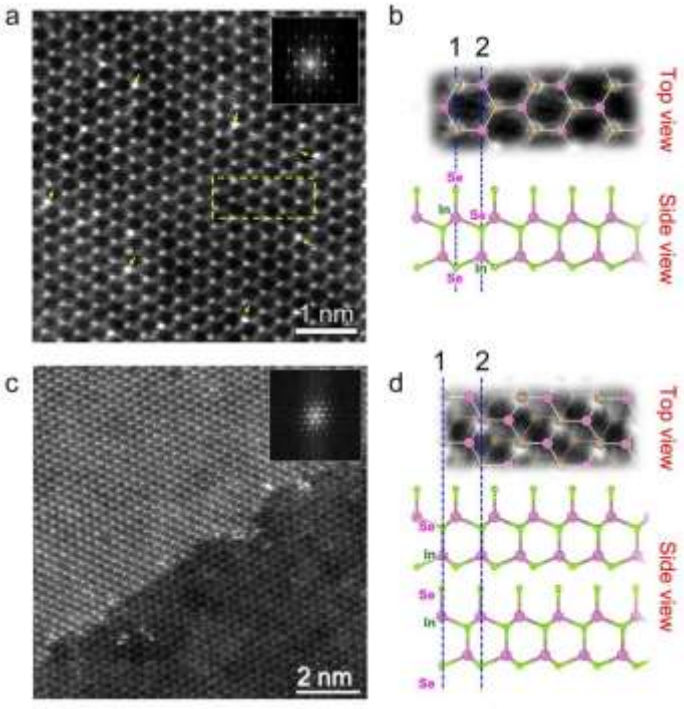

Figure 7.6 STEM imaging of monolayer and bi-layer α-phase In_2Se_3. (a) HAADF STEM image and Fast Fourier Transform (FFT) pattern. (b) The region highlighted in (a). Line 1: Se-In-Se sequence (bright sites); line 2: a Se-In sequence (dark site). (c) Monolayer In_2Se_3 and bi-layer In_2Se_3 with an AB stacking. Some indium absorbed on the surface. (d) AB stacking of bi-layer In_2Se_3.

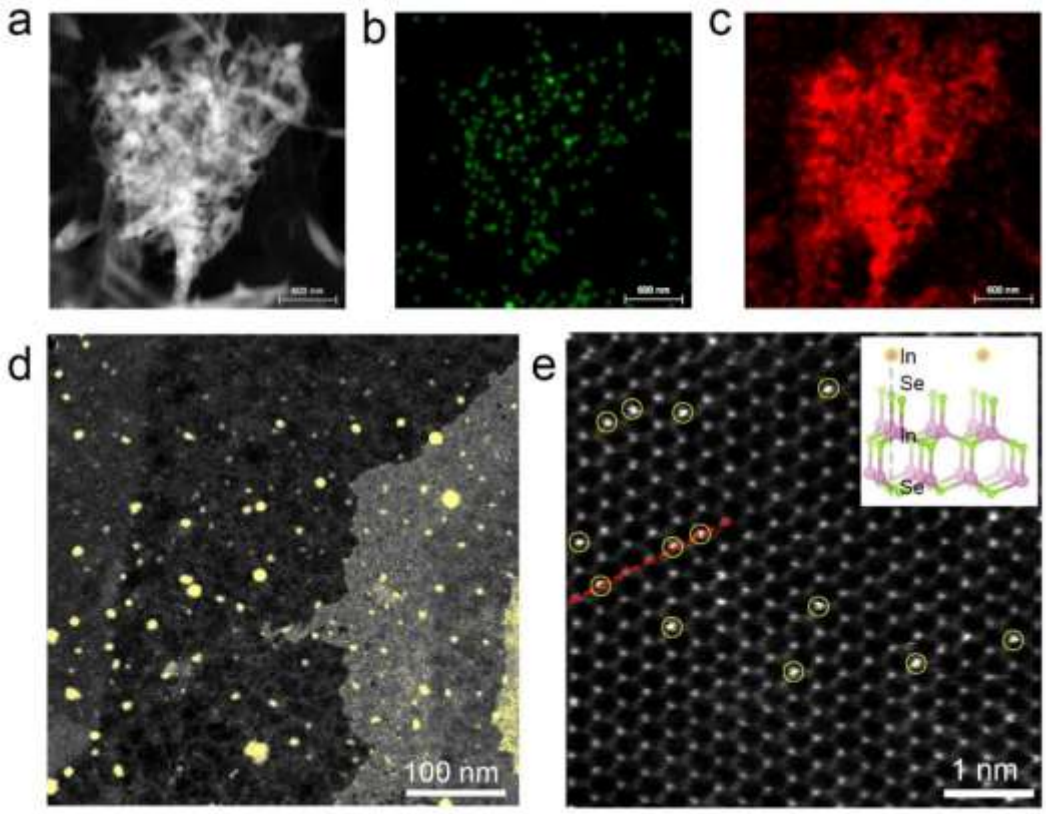

Figure 7.7 STEM characterization of indium particles. (a) TEM image of a large indium particle ~ 1μm. (b, c) Elemental mapping of Se and In, respectively. (d) Relative small indium particles (yellow) with a size ranging from a few nm to 20 nm. (e) Yellow circles indicates the dopants found in the monolayer In_2Se_3.

It is known that there are about five phases (α, β, γ, δ, κ) in In_2Se_3. Especially, the δ- and γ- In_2Se_3 are monoclinic structure and cubic (a defect wurtzite structure), respectively. The recently discovered phase-κ-In_2Se_3 is a relative new phase. However, only the three phases i.e. α, β and κ are layered structure.[30, 31] All these phases are very difficult to be identified in their monolayer or bilayer. Recently, a phase transition has been observed from α-In_2Se_3 to β-In_2Se_3 at a high temperature of 450 K by Raman spectra.[30, 31] The β phase is a high temperature phase and can be confirmed by growing condition. However, β phase cannot be obtained in this experiment, because the growth temperature cools down to room temperature naturally. Herein, temperature-dependent Raman spectroscopy was employed

to check the phase transition of as-synthesized samples. As shown in Figure 7.8, the phase transition at high temperature is confirmed, demonstrating that the In_2Se_3 is α phase In_2Se_3 in this experiment.

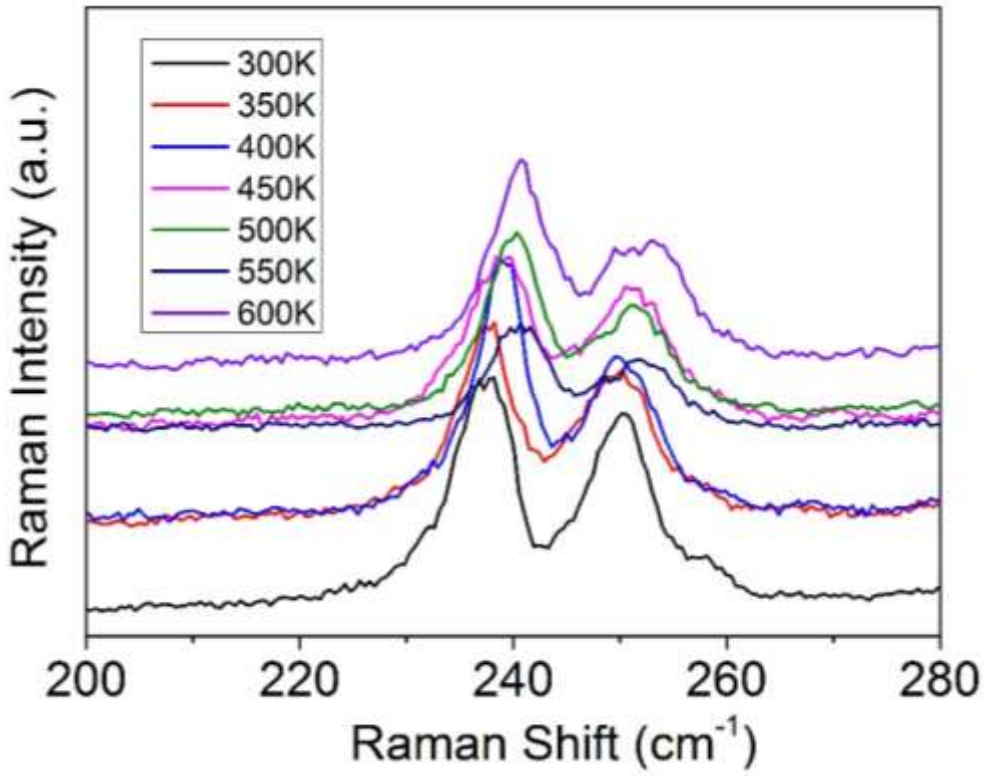

Figure 7.8 Micro-Raman spectra of monolayer In_2Se_3 at various temperatures, indicating the α phase In_2Se_3 in this experiment.

7.2.4 Applications of In_2Se_3

In order to study the application of α phase In_2Se_3 in FET and photodetector, FETs were fabricated using In_2Se_3 few layers. The drain and source of Cr/Au (~ 5 nm and 50 nm, respectively) contacts were thermally evaporated onto the samples surface by electron beam lithography (EBL). Figure 7.9a and Figure 7.9b show the output and the transfer characteristics of the FET. It should be noted that the In_2Se_3 FETs shows a p-type semiconducting behavior, which is different from the previous report on In_2Se_3 with n-type behavior.[32] The abnormal situation could be attributed to high temperature (850°C)

growth. A selenium-rich environment appears because of the decomposition of In_2Se_3, which has also been observed during the growth of InSe nanowire at a high temperature using the In_2Se_3 as the sources.[24] It can calculate the mobility of as-synthesized In_2Se_3 from Figure 7.9b, based on the following equation $\mu = dI_{ds}/dV_{bg} \times L_{ch}/(W_{ch}C_{ox}V_{ds})$, where the L is the channel length, the W is the channel width, and the Cox ($C_{ox} = 1.26 \times 10^{-4}$ F/m^2). The mobility of the In_2Se_3 device is calculated to be 2.5 $cm^2V^{-1}S^{-1}$, which is similar to that of the CVD MoS_2 and also higher other III-VI group layered materials including GaSe, GaTe, and GaS.[33-36]

Herein, the photodetector performance of monolayer In_2Se_3 was studied. Figure 7.9c shows the I-V characteristics of the In_2Se_3 photodetector, which are measured under 532 nm laser illuminated and dark conditions at $V_g = 0$ V. It can be seen that the photocurrent still remains high even at a very low illumination intensity (26μW/cm^2). Figure 7.9d shows the relationship between the incident light intensity (P) and current. It exhibits that the photocurrent increases linearly with the variation of V_d in the low V_d region. However, the saturated photocurrent is observed when the V_d further increases, which is the consequence of the Schottky barrier in In_2Se_3 devices.[29] From the result in Figure 7.9d combined with the equation photoresponsivity = $(I_{light} - I_{dark})/P_{light}$, the photoresponsivity is calculated to be ~ 340A/W, which is better than the previous reports on the In_2Se_3 nanosheets (7.2A/W), In_2Se_3 flakes (2.5A/W), the In_2Se_3 nanowires (150A/W), the 2D GaSe flakes (2.8A/W) and graphene (0.01A/W).[15, 18, 21] The comparison results are also shown in Figure 7.9e. Additionally, the rise and fall time can be calculated from Figure 7.9f, to be about 6 ms and 12 ms (using the photocurrent from 10% to 90% for the rise times, 90% to 10% for the fall times) respectively, indicating potential application of few layer α-In_2Se_3 for a resistor-mode photodetector.

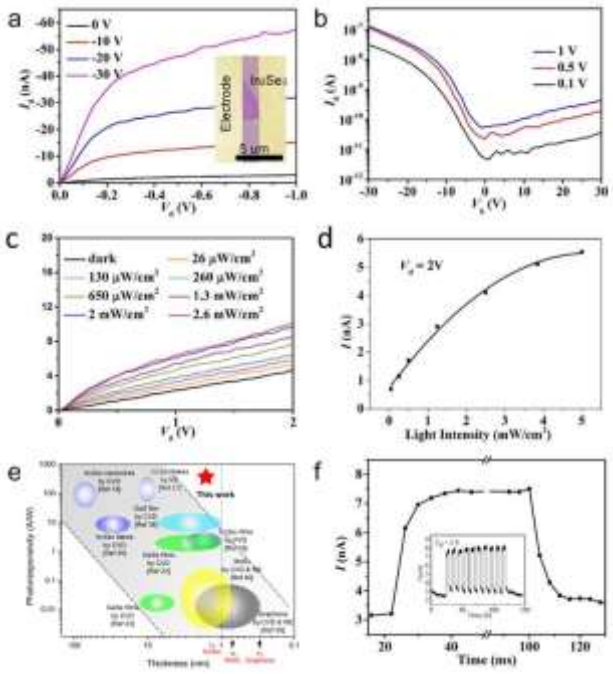

Figure 7.9 Optoelectronic performance of α-In_2Se_3. (a and b) Output and transfer characteristics of few layered In_2Se_3. Inset: false-colored of the fabricated α-In_2Se_3 transistor. (c) Photocurrent under the illumination with different light intensities. (d) Time-resolved photoresponse under on and off the light illumination. (e) Summarized the relationship between photoresponsivity and thickness in 2D layers. (f) Rise and decay behaviors of photocurrent.

7.3 Conclusions

In this chapter, the large-size α-In_2Se_3 monolayers obtained by PVD method under different growing conditions were discussed. Raman and PL spectra in monolayer In_2Se_3 were observed for the first time. The atomic structure of In_2Se_3 was examined by electron diffraction. STEM imaging showed the AB stacking in bi-layer In_2Se_3. The few-layer In_2Se_3 showed a p-type semiconducting property and a high mobility. Moreover, an excellent photoresponsivity of few-layer In_2Se_3 transistor indicates the great potential of In_2Se_3 in the field of optoelectronic applications

References

[1] J. H. Chen, C. Jang, S. D. Xiao, M. Ishigami, M. S. Fuhrer, Nat Nanotechnol 2008, 3, 206.

[2] K. S. Novoselov, D. Jiang, F. Schedin, T. J. Booth, V. V. Khotkevich, S. V. Morozov, A. K. Geim, P Natl Acad Sci USA 2005, 102, 10451.

[3] Q. H. Wang, K. Kalantar-Zadeh, A. Kis, J. N. Coleman, M. S. Strano, Nat Nanotechnol 2012, 7, 699.

[4] B. Radisavljevic, A. Kis, Nat Mater 2013, 12, 815.

[5] L. K. Li, Y. J. Yu, G. J. Ye, Q. Q. Ge, X. D. Ou, H. Wu, D. L. Feng, X. H. Chen, Y. B. Zhang, Nat Nanotechnol 2014, 9, 372.

[6] W. X. Zhang, Z. S. Huang, W. L. Zhang, Y. R. Li, Nano Res 2014, 7, 1731.

[7] S. Z. Butler, S. M. Hollen, L. Y. Cao, Y. Cui, J. A. Gupta, H. R. Gutierrez, T. F. Heinz, S. S. Hong, J. X. Huang, A. F. Ismach, E. Johnston-Halperin, M. Kuno, V. V. Plashnitsa, R. D. Robinson, R. S. Ruoff, S. Salahuddin, J. Shan, L. Shi, M. G. Spencer, M. Terrones, W. Windl, J. E. Goldberger, Acs Nano 2013, 7, 2898.

[8] S. H. Kwon, B. T. Ahn, S. K. Kim, F. Adurodija, K. H. Kang, K. H. Yoon, J. S. Song, J Korean Phys Soc 1997, 31, 796.

[9] P. A. Hu, L. F. Wang, M. Yoon, J. Zhang, W. Feng, X. N. Wang, Z. Z. Wen, J. C. Idrobo, Y. Miyamoto, D. B. Geohegan, K. Xiao, Nano Lett 2013, 13, 1649.

[10] C. Schumacher, K. G. Reinsberg, R. Rostek, L. Akinsinde, S. Baessler, S. Zastrow, G. Rampelberg, P. Woias, C. Detavernier, J. A. C. Broekaert, J. Bachmann, K. Nielsch, Adv Energy Mater 2013, 3, 95.

[11] L. Goncalves, C. Couto, P. Alpuim, D. M. Rowe, J. H. Correia, Mater Sci Forum 2006, 514-516, 156.

[12] J. Jasinski, W. Swider, J. Washburn, Z. Liliental-Weber, A. Chaiken, K. Nauka, G. A. Gibson, C. C. Yang, Appl Phys Lett 2002, 81, 4356.

[13] J. P. Ye, S. Soeda, Y. Nakamura, O. Nittono, Jpn J Appl Phys 1 1998, 37, 4264.

[14] S. T. Lakshmikumar, A. C. Rastogi, Sol Energ Mat Sol C 1994, 32, 7.

[15] T. Y. Zhai, X. S. Fang, M. Y. Liao, X. J. Xu, L. Li, B. D. Liu, Y. Koide, Y. Ma, J. N. Yao, Y. Bando, D. Golberg, Acs Nano 2010, 4, 1596.

[16] K. J. Lai, H. L. Peng, W. Kundhikanjana, D. T. Schoen, C. Xie, S. Meister, Y. Cui, M. A. Kelly, Z. X. Shen, Nano Lett 2009, 9, 1265.

[17] B. Yu, S. Y. Ju, X. H. Sun, G. Ng, T. D. Nguyen, M. Meyyappan, D. B. Janes, Appl Phys Lett 2007, 91.

[18] M. Lin, D. Wu, Y. Zhou, W. Huang, W. Jiang, W. S. Zheng, S. L. Zhao, C. H. Jin, Y. F. Guo, H. L. Peng, Z. F. Liu, J Am Chem Soc 2013, 135, 13274.

[19] R. B. Jacobs-Gedrim, M. Shanmugam, N. Jain, C. A. Durcan, M. T. Murphy, T. M. Murray, R. J. Matyi, R. L. Moore, B. Yu, Acs Nano 2014, 8, 514.

[20] X. Lu, M. I. B. Utama, J. H. Lin, X. Gong, J. Zhang, Y. Y. Zhao, S. T. Pantelides, J. X. Wang, Z. L. Dong, Z. Liu, W. Zhou, Q. H. Xiong, Nano Lett 2014, 14, 2419.

[21] S. D. Lei, L. H. Ge, Z. Liu, S. Najmaei, G. Shi, G. You, J. Lou, R. Vajtai, P. M. Ajayan, Nano Lett 2013, 13, 2777.

[22] J. J. Wang, F. F. Cao, L. Jiang, Y. G. Guo, W. P. Hu, L. J. Wan, J Am Chem Soc 2009, 131, 15602.

[23] C. H. Ho, Sci Rep-Uk 2014, 4.

[24] J. Weszka, P. Daniel, A. Burian, A. M. Burian, A. T. Nguyen, J Non-Cryst Solids 2000, 265, 98.

[25] H. Li, Q. Zhang, C. C. R. Yap, B. K. Tay, T. H. T. Edwin, A. Olivier, D. Baillargeat, Adv Funct Mater 2012, 22, 1385.

[26] N. O. Kim, H. G. Kim, H. J. Lim, C. I. Lee, M. S. Jin, C. S. Yoon, W. T. Kim, J Korean Phys Soc 2001, 38, 405.

[27] S. Popovic, A. Tonejc, B. Grzetaplenkovic, B. Celustka, R. Trojko, J Appl Crystallogr 1979, 12, 416.

[28] S. A. Semiletov, Sov Phys-Sol State 1961, 3, 544.

[29] M. J. Hytch, E. Snoeck, R. Kilaas, Ultramicroscopy 1998, 74, 131.

[30] X. Tao, Y. Gu, Nano Lett 2013, 13, 3501.

[31] C. H. de Groot, J. S. Moodera, J Appl Phys 2001, 89, 4336.

[32] Q. L. Li, C. H. Liu, Y. T. Nie, W. H. Chen, X. Gao, X. H. Sun, S. D. Wang, Nanoscale 2014, 6, 14538.

[33] D. J. Late, B. Liu, J. J. Luo, A. M. Yan, H. S. S. R. Matte, M. Grayson, C. N. R. Rao, V. P. Dravid, Adv Mater 2012, 24, 3549.

[34] P. A. Hu, Z. Z. Wen, L. F. Wang, P. H. Tan, K. Xiao, Acs Nano 2012, 6, 5988.

[35] F. C. Liu, H. Shimotani, H. Shang, T. Kanagasekaran, V. Zolyomi, N. Drummond, V. I. Fal'ko, K. Tanigaki, Acs Nano 2014, 8, 752.

[36] O. Lopez-Sanchez, D. Lembke, M. Kayci, A. Radenovic, A. Kis, Nat Nanotechnol 2013, 8, 497.

Chapter 8

Implications/Impact/Outstanding Questions

In this part, a general conclusion of the whole thesis were discussed, including the implications, impact and outstanding questions. First, the main outcomes are summarized as follows: 1) large-size monolayer $MoTe_2$ and WTe_2 are obtained via chemical vapor deposition method; 2) TiX_2, VX_2 and NbX_2 are synthesized via molten salt-assisted chemical vapor deposition method; 3) $PtSe_2/MoSe_2$ heterostructure is prepared by one-step chemical vapor deposition method and monolayer In_2Se_3 obtained by physical vapor deposition method; 4) the properties and applications of all the as-synthesized 2D materials above are mentioned. Second, the work about the growth mechanism and properties of TiX_2, VX_2 and NbX_2 that are needed to be addressed in future is also discussed. Finally, a summarization is presented to explain the outcomes reflected in the original hypothesis.

8.1 General Discussion

In this thesis, the synthesis, properties and applications of the monolayer and few-layer 2D materials and their heterostructure were discussed. Specifically, the preparation, properties, structrues and applications of the tellurides including $MoTe_2$ and WTe_2, 2D TDMs such as TiX_2, VX_2, and NbX_2 together with large-size monolayer In_2Se_3, and epitaxial growth of the $PtSe_2/MoSe_2$ heterostructure were studied in details.

First, large-size tellurides including WTe_2 and $MoTe_2$ were produced by CVD method. The mixed compounds Te, $MoCl_5$ (WCl_6), and MoO_3 (WO_3) as precursors are regarded as the key role for the tellurides growth. The atomic structure of WTe_2 monolayer was identified for the first time. Especially, the domain walls in bi-layer WTe_2 with the stacking boundary between two distinct stacking sequences were observed. The atom-thin $MoTe_2$ showed the same atomic structure as WTe_2. Electrical transport measurements based on the few-layered and monolayer $MoTe_2$ and WTe_2 showed enhanced superconductivity and semimetal-to-insulator transition, respectively. This work opens up a new approach to the synthesis of large size tellurides. More importantly, synthesis of the topological-superconducting material i.e. $MoTe_2$ boost the realization of quantum spin Hall devices.

Second, a new molten salt-assisted CVD method was designed to synthesis of TiX_2, VX_2, and NbX_2 based 2D TDMs for the first time. The large monolayer TiS_2, VS_2, VSe_2, NbS_2 and $NbSe_2$ together with few-layered $TiSe_2$, $TiTe_2$, VTe_2 and $NbTe_2$ were prepared for the first time. Raman spectra and STEM were performed to confirm the as-synthesized 2D TMDs successfully. The superconducting transition behavior was observed in the monolayer $NbSe_2$, indicating the high quality of as-produced 2D TMDs. This work will motivate the researchers to produce such kinds of 2D TMDs and study their novel properties such as ferrimagnetism, superconductivity and CDW state.

Third, the $PtSe_2/MoSe_2$ vertical heterojunction was synthesized via one-step CVD method. It was found that the strong coupling epitaxial growth behavior was crucial for the growth of $PtSe_2/MoSe_2$. The large-scale monolayer $PtSe_2$ single crystal was obtained for the first

time. Raman spectra, XPS and STEM results confirmed the heterojunction structure of $PtSe_2/MoSe_2$.The strong coupling between $PtSe_2$ and $MoSe_2$ offered the opportunity to study the charge transfer. The p type $PtSe_2$ and n type $MoSe_2$ provided the possibility to broaden their applications in p-n junction. More importantly, the strategy proposed here paves the way to synthesize the vertical heterostructure between group 10 TMDs and MX_2.

Forth, large α-In_2Se_3 monolayer single crystal was synthesized for the first time by PVD method. The α-In_2Se_3 was confirmed from the atomic structure examined by TEM and STEM imaging and temperature-dependent Raman spectra. The high mobility of the In_2Se_3 atomic layers indicated the high quality of as-synthesized In_2Se_3. Moreover, excellent photoresponsivity in the atom-thin In_2Se_3 flake shows the great potential of In_2Se_3 in the field of optoelectronic applications.

8.2 Reconnaissance Work not Included in Main Chapters

As mentioned above, although several different types of 2D TMDs, $PtSe_2/MoSe_2$ heterostructure and In_2Se_3 have been synthesized and their properties based on the FETs have been studied, more efforts need to be devoted in the future.

First, large-size $MoTe_2$ and WTe_2 have been successfully synthesized. However, the predicted quantum spin Hall devices based on monolayer $MoTe_2$ has not been realized, which is of great importance for the development of next-generation quantum computer.

Second, using the salts such as the NaCl and KI as the reaction sources, TiX_2, VX_2, and NbX_2 based 2D TDMs with different crystal styles can be prepared. Nevertheless, the growth mechanism is still not clear now, and is be elucidated. Moreover, the novel properties have not been fully exploited. It is also unsure whether this method can be directly extended to synthesis of other 2D TMDs such as ZrX_2, HfX_2, PtX_2 and PdX_2. All these concerns are discussed as follows:

For the growth mechanism: The reported synthetic process for MoS_2, WS_2, $MoSe_2$ and WSe_2 is the route 2 that has been discussed in the introduction part. In order to confirm the growth mechanism of MoS_2, the formation stages for the MoS_2 flakes have been discerned [1], during the experiment, the in-situ transmission electron microscopy was used to detect the formation of MoS_2. The result shows that the vertically aligned MoS_2 structures grow in the form of layer-by-layer mode. However, the orientation of MoS_2 structures becomes horizontal with increasing growth temperature. Specially, when the growth temperature reaches up to 850 ºC, the size of MoS_2 increases owning to merging adjacent flakes. The corresponding TEM results are shown in Figure 8.1 and 8.2.

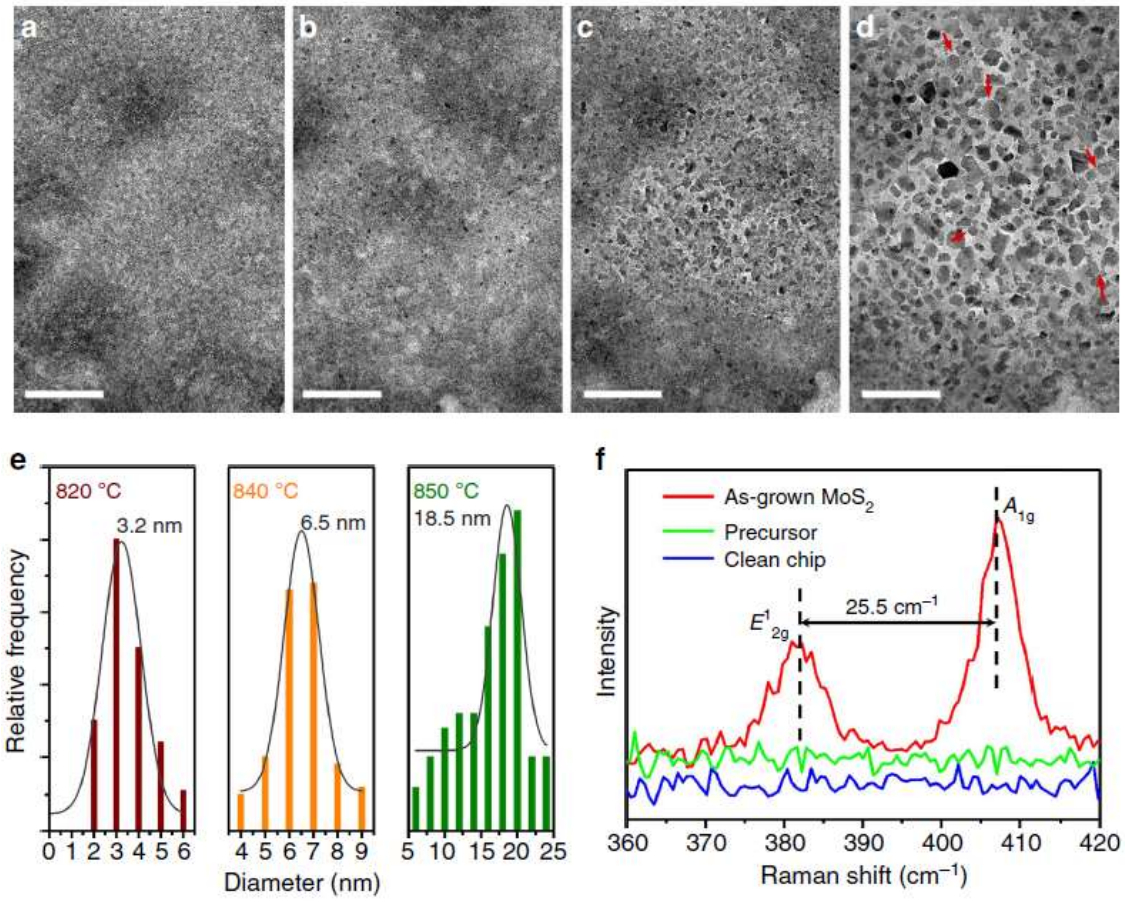

Figure 8.1 Formation of 2D MoS_2 flakes with heating temperature above 800 ºC. (a–d) TEM image showing the size of MoS_2 increases with increasing temperatures: (a) 800 ºC, (b) 820 ºC, (c) 840 ºC, and (d) 850 ºC. The red arrows in (d) denote 120º angles. Scale bars: 100 nm. (e) Distribution of MoS_2 size as a function of temperature. The areas are 340 to 516 nm^2. (f) Raman spectra of the E-chip.

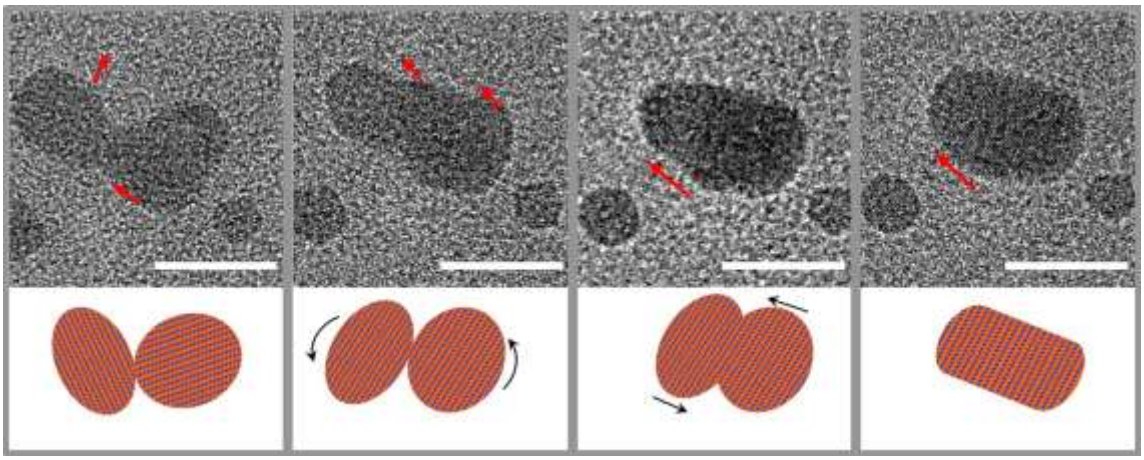

Figure 8.2 (a–d) Sequences of in situ TEM images, illustrating that the flakes (I and II) merge into flake III; (a) 0 s. (b) 22s. (c) 42 s. (d) 59 s. Scale bars, 10 nm.

The growth mechanism of MoS_2 was further studied by in-situ transmission electron microscopy (TEM) [2]. In the experiment, the MoS_2 was prepared on the graphene which was supported on Cu grid. Through observing the nucleation seed, evolution morphology, edge structure and the terminations at the atomic scale during the CVD growth process, two forms of seed centers which are Mo-oxysulfide (MoO_xS_{2-y}) nanoparticles and the Mo-S atomic clusters were formed. Mo-oxysulfide (MoO_xS_{2-y}) nanoparticles which appear in a form of multi-shelled fullerene-like structures or in compact nanocrystals are the key for the growth of fewer-layer MoS_2. However, the Mo-S atomic clusters are essential for the growth of monolayer MoS_2. The growth mechanism is shown in Figure 8.3.

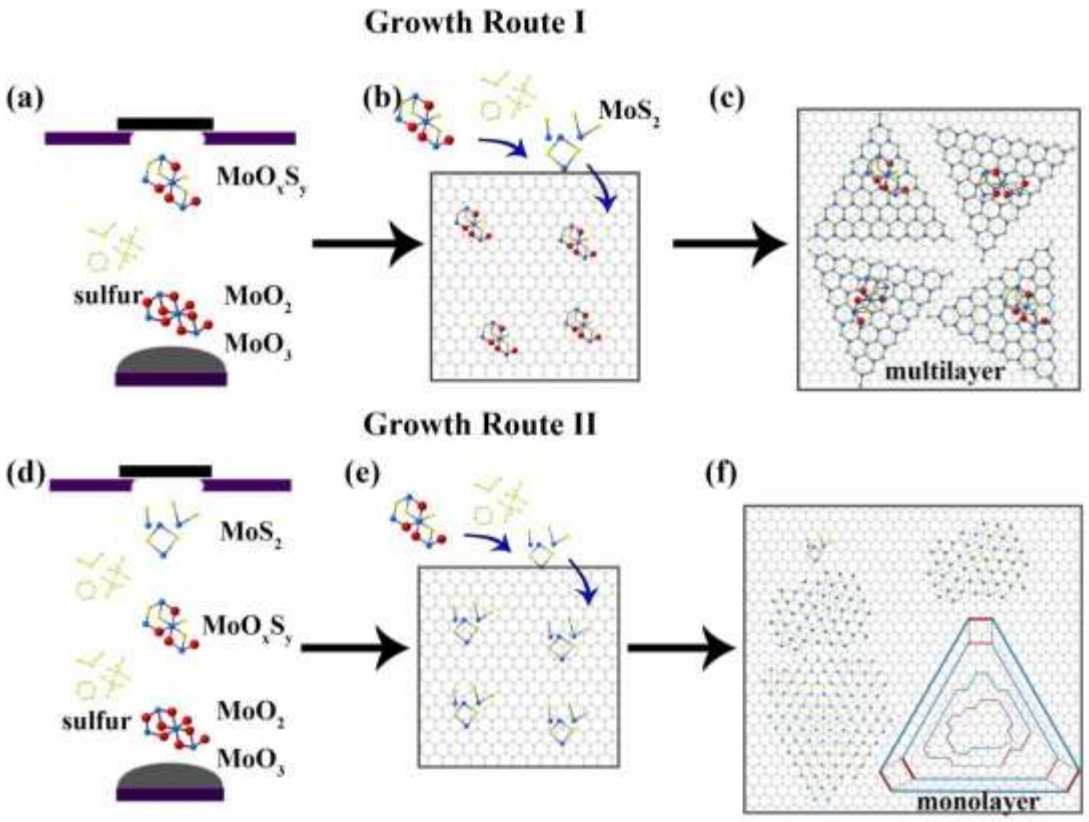

Figure 8.3 (a-c) Schematic sketches explaining the possible route for the nucleation and growth kinetics of few-lay MoS_2 bound with thick core, and (d-f) for the nucleation and growth kinetics of MoS_2 monolayers.

For the synthesis: our salt-assisted approach, which actually adds the salt NaCl or KI into the precursors, lowers the melting point of the growth system, so the growth mechanism needs to be further elucidated by in-situ TEM and STEM.

For the properties: although 2D TiX_2, VX_2, and NbX_2 have been synthesized, only the superconductivity is observed in the monolayer $NbSe_2$. The high-mobility and phase-transition in TiX_2, the ferromagnetism in VX_2 monolayers, superconductivity and charge density wave (CDW) effects in group-V TMD monolayers have not been studied, which is also the concern in my future work.

8.3 Outcomes Reflected in the Original Hypothesis

In the thesis, the large-size $MoTe_2$ and WTe_2 monolayers were synthesized by CVD method via using mixed powders of Te, $MoCl_5$ (WCl_6) and MoO_3 (WO_3) as the precursors. Their properties have been studied. The results are in good agreement with the hypothesis that $MoTe_2$ and WTe_2 cannot be obtained using the oxides as the precursors. The mixed compounds not only reduce the growth temperature of $MoTe_2$ and WTe_2 but also enhance their stability.

The typical 2D TMDs including TiX_2, VX_2 and NbX_2 (X: S, Se and Te) have been successfully prepared via molten salt-assisted CVD method. The added salt facilitates the growth of 2D TMDs via reducing the melting point of precursors. The superconductivity in the monolayer $NbSe_2$ has been demonstrated. These results open up a new route to the synthesis of new 2D TMDs. However, the magnetism in VX_2 monolayers and CDW state in TiX_2 mentioned in the hypothesis have not been studied and need to be investigated in the future.

The vertically stacked $PtSe_2/MoSe_2$ heterostructure has been synthesized via one-step CVD method, which is in good agreement with the hypothesis. The large-size In_2Se_3 monolayer was produced by PVD method for the first time and its excellent photoresponsivity has been demonstrated. This is in accordance with the hypothesis and indicates its potential applications in the field of optoelectronic.

References

[1] L. F. Fei, S. J. Lei, W. B. Zhang, W. Lu, Z. Y. Lin, C. H. Lam, Y. Chai, Y. Wang, Nat Commun 2016, 7.

[2] D. Zhu, H. Shu, F. Jiang, D. Lv, V. Asokan, O. Omar, J. Yuan, Z. Zhang, C. Jin, npj 2D Materials and Applications 2017, 1.

Publications

1. **J. d. Zhou**, F. c. Liu, J. h. Lin, X. w. Huang, J. Xia, B. w. Zhang, Q. s. Zeng, H. Wang, C. Zhu, L. Niu, X. w. Wang, W. Fu, P. Yu, T. R. Chang, C.H. Hsu, D. Wu, Horng-Tay Jeng, Y. z. Huang, H. Lin, Z. x. Shen, C. l. Yang, L. Lu, K, Suenaga, W. Zhou, T. Pantelides, G. t. Liu and Z. Liu. Large-area and high-quality 2D transition metal telluride, *Advanced Materials*, 29, 1603471, 2016.
2. **J. d. Zhou**, Q. s, Zeng, D. h. Lv, L. f. Sun, L. Liu, W. Fu, F. c. Liu, Z. x. Shen, C. h. Jin, Z. Liu. Controlled Synthesis of High-quality Monolayered α-In_2Se_3 via Physical Vapor Deposition, *Nano Letters*, 2015, 15, 6400
3. M. Chen#, J. Xia#, **J. d. Zhou**#, Q.s. Zeng, K. w. Li, K. Fujisawa, W. Fu, T. Zhang, J. Zhang†, Z. Wang, Z. x. Wang, X. t. Jia, M. Terrones, Z. X. Shen, Z. Liu, and L. Wei. Ordered and Atomically Perfect Fragmentation of Layered Transition Metal Dichalcogenides via Mechanical Instabilities, *ACS Nano*, **DOI:** 10.1021/acsnano.7b04158.
4. X. y. Yang, Y. t. Wang, **J. d. Zhou**, Z. Liu. Temperature-dependent morphology of chemical vapor grown molybdenum disulfide. Journal of Physics D, Doi:10.1088/1361-6463/aa6220.
5. J. X;, Q. s. Zeng, **J. d. Zhou**, W. Zhou, Q. Zhang, J. x. Yan, Z. Liu, Z. X. Shen, Current rectification and asymmetric photoresponse in MoS_2 stacking-induced homojunctions. *2D materials*, 2DM-101822.
6. H. Wang , X. w. Huang , J. h. Lin , J. Cui , Y. Chen, C. Zhu, F. c. Liu, Q. s. Zeng, **J. d. Zhou** , P. Yu, X. w. Wang, H. y. He, S. H. Tsang, W. b. Gao, K. Suenaga, F. c. Ma, C. l. Yang , L. Lu, T. Yu, Edwin Teo, G. t. Liu, Z. Liu. High-quality monolayer superconductor $NbSe_2$ grown by chemical vapour deposition. *Accepted by nature communications*.
7. F. c. Liu, **J. d. Zhou**, C. Zhu, Z. Liu. Electric Field Effect in Two-Dimensional Transition Metal Dichalcogenides$_2$, *Advanced Functional Materials* 2016. 10.1002/adfm.201602404
8. W. L. Chow, P. Yu, F. C. Liu, J. h. Hong, X. l. Wang, Q. s. Zeng, C.-H. Hsu, C. Zhu, **J. d. Zhou**, X. w. Wang, J. Xia, J. x. Yan, Y. Chen, D. Wu, T. Yu, Z. x. Shen, H. Lin, C. h. Jin, B. K. Tay, Z. Liu. High Mobility 2D Palladium Diselenide Field-effect Transistors with Tunable Ambipolar Characteristics, *Advanced Materials*, 2017 10.1002/adma.201602969.

9. W. Fu, Y. Chen, J. h. Lin, X. w. Wang, Q. s. Zeng, **J. d. Zhou**, L. Zheng, H. Wang, Y. m. He, H. y. He, Q. d. Fu, K. Suenaga, T. Yu, Z. Liu Controlled Synthesis of Atomically Thin 1T-TaS_2 for Tunable Charge Density Wave Phase Transitions, *Chemistry of Materials*, 28, 7613, 2016
10. W. Fu, H. y. He, Z. h. Zhang, C. y. Wu, X. w. Wang, H. Wang, Q. s. Zeng, P. Yu, L. f. Sun, X. l. Wang, **J. d. Zhou**, Z. x. Shen, C. h. Jin, B. I. Yakobson, Z. Liu. Strong interfacial coupling of MoS_2/g-C_3N_4 van de Waals solids for highly active water reduction, *Nano Energy*, 27, 44, 2016
11. F. c. Liu, L. You, K. L. Seyler, X. b. Li, P. Yu, J. h. Lin, X. w. Wang, **J. d. Zhou**, H. Wang, H. y. He, S. T. Pantelides, W. Zhou, P. Sharma, X. d. Xu, P. M. Ajayan, J. l. Wang, Z. Liu. Room-temperature ferroelectricity in $CuInP_2S_6$ ultrathin flakes, *Nature Communications*, 7, 12357, 2016
12. F. c. Liu, C. Zhu, L. You, S. j. Liang, S. j. Zheng, **J. d. Zhou**, Q. d. Fu, Y. m. He, Q. s. Zeng, H. J. Fan, L. K. Ang, J. l. Wang, Z. Liu. 2D Black Phosphorus/SrTiO3 based Programmable Photoconductive Switch, *Advanced Materials*, 2016. 10.1002/adma.201602280
13. L. Niu, Q. s. Zeng, J. Shi, C. x. Cong, C. y. Wu, F. c. Liu, **J. d. Zhou**, W. Fu, Q. d. Fu, C. h. Jin, T. Yu, X. f. Liu, Z. Liu. Controlled Growth and Reliable Thickness-dependent Properties of Organic-inorganic Perovskite Platelet Crystal , *Advanced Functional Materials* , 2016 10.1002/adfm.201601392
14. F. c. Liu, S. j. Zheng, A. Chaturvedi, V. Zólyomi**, J. d. Zhou**, Q. d. Fu, C. Zhu, P. Yu, Q. s. Zeng, N. Drummond, H. J. Fan, C. Kloc, V. I. Fal'ko, X. x. He, Z. Liu Optoelectronic properties of atomically thin ReSSe with weak interlayer coupling, *Nanoscale*, 2016,8, 5826-5834
15. F. c. Liu, S. j. Zheng, X. x. He, A. Chaturvedi, J. f. He, W. L. Chow, T. R. Mion, X. l. Wang, **J. d. Zhou**, Q. d. Fu, H. J. Fan, B. K. Tay, L. Song, R. H. He, C. Kloc, P. M. Ajayan, Z. Liu Highly Sensitive Detection of Polarized Light Using Anistropic 2D ReS_2, *Advanced Functional Materials*, 2015, 10.1002/adfm.201504546
16. L. Niu, X. f. Liu, C. x. Cong, C. y. Wu, D. Wu, T. R. Chang, H. Wang, Q. s. Zeng, **J. d. Zhou**, X. l. Wang, W. Fu, P. Yu, Q. d. Fu, S. Najmaei, Z. h. Zhang, B. I. Yakobson, B. K. Tay, W. Zhou, H. T. Jeng, H. Lin, T. C. Sum, C. h. Jin, H. y. He, T. Yu, Z. Liu Controlled Synthesis of Organic/Inorganic van der Waals Solid for Tunable Light-matter Interactions, *Advanced Materials*, 27, 7800, 2015

17. J. Shi, P. Yu, F. c. Liu, P. He, R. Wang, L. Qin, J. b. Zhou, X. Li, **J. d. Zhou**, X. y. Sui, S. Zhang, Y. f. Zhang, Q. Zhang, T. C. Sum, X. h. Qiu, Z. Liu and X. f. Liu. 3R MoS_2 with Broken Inversion Symmetry: A Promising Ultrathin Nonlinear Optical Device, *Advanced Materials* DOI: 10.1002/adma.201701486.